ALMA MATER STUDIORUM – UNIVERSITY OF BOLOGNA
SCHOOL OF ENGINEERING AND ARCHITECHTURE

Master Thesis

Tunnelling-induced deformation and damage on framed structures with masonry infills

Supervisor:

Prof. Daniela Boldini

Co-supervisor:

Dr. Andrea Franza

Candidate:

Seyedmohsen Miraei

October 2020

Table of Contents

Acknowledgments

Throughout the writing of this dissertation I have received a great deal of support and assistance.

I would first like to thank my supervisor, Professor Daniela Boldini, for her dedicated support and guidance. She continuously provided encouragement, and her insightful feedback pushed me to sharpen my thinking and brought my work to a higher level.

I would also like to thank my co-supervisor, Dr. Andrea Franza, for his valuable guidance throughout my studies. He provided me with the tools that I needed to choose the right direction and successfully complete my dissertation.

In addition, I would like to thank Dr. Nunzio Losacco for providing advice regarding analysis and for his valuable contribution through this research.

In addition, I would like to thank my parents for their wise counsel and sympathetic ear. You are always there for me.

List of Publications

Conference papers

Boldini, D., Losacco, N., Franza, A., Miraei, M., **Numerical modelling of framed structures with masonry infills affected by tunnelling-induced deformations and damage,** *IS-Cambridge 2020, 10th International Symposium on Geotechnical Aspects of Underground Construction in Soft Ground, Accepted, Cambridge, England, Accepted, 2020.*

Boldini, D., Losacco, N., Franza, A., Miraei, M., **Tunnelling-induced displacements and damage on framed structures: comparison between centrifuge and numerical results,** *IACMAG, 16th International conference of the International Association for Computer Methods and Advances in Geomechanics, Submitted, Turin, Italy, Accepted, 2020.*

ABSTRACT

The expansion of cities often involves tunnel construction, which may result in detrimental effects on structures.This research describes a numerical approach aimed at investigating the interaction between tunnelling-induced ground deformations and framed buildings with masonry infills. This study includes experimental data obtained from geotechnical centrifuge tests and predictions of building response based on numerical analyses. The numerical model, analysed with the Finite Element method, includes the soil, the tunnel, and the framed structure with infills. It proved its capability in reproducing the soil response at different values of the volume loss and the principal soil-structure interaction mechanisms, including sliding and development of a gap at the soil-foundation interface. In addition, a large number of framed building models were simulated to investigate the effects of volume loss of the tunnel, presence of masonry infills, opening of infills, eccentricity, and dimensions of the building. The results are summarised in terms of angular distortion values for each bay as well as local tensile strains in the masonry infills. Moreover, the efficiency of angular distortion models in predicting the maximum tensile strain of the infills is also evaluated. Finally, the maximum tensile strains of infills are used to evaluate the building deformation based on the damage classifications.

Keywords:

tunnel subsidence, soil/structure interaction, centrifuge modelling, finite-element modelling, framed structure, masonry infills.

Chapter. 1. Introduction

1.1 Background and motivations

The development of cities and urban areas is resulting in an increased demand for sustainable transport and services infrastructure. Underground construction and infrastructure that often require the excavation of tunnels represent an ideal solution to satisfy these needs. Nowadays, tunnels are the most used techniques of transport in metropolitan cities of the world. Also, tunnel construction is increasingly taking place close to buried and surface structures. If protective measures are not adopted, tunnel construction inevitably affects existing structures due to the induced ground movements and stress relief which in some cases could represent damage for buildings located on the ground level. To optimize the design of tunnel excavations and minimize the surface movements generated by the excavation of a tunnel (which involves assessing tunnelling-induced greenfield soil movements, the deformations induced on structures resulting from soil-structure interactions, and the risk of failure), engineers need to be able to efficiently predict building distortions considering soil-structure interaction.

Current design approaches for the evaluation of tunnelling induced damage on buildings are based on semi-empirical evaluations of the deflection ratios and horizontal tensile strains at foundation level, assuming that the structure will conform to the greenfield displacements (Peck, 1969; Burland and Wroth, 1975; Burland, 1977; O'Rrielly and New, 1982; Boscardin and Cording, 1989; Burland, 1997). The response of buildings to tunnelling-induced ground movements has been investigated extensively (Pickhaver et al., 2010; Amorosi et al., 2014; Farrell et al., 2014; Bilotta et al., 2017). While the effect of tunnel excavation on masonry structures has been thoroughly studied (e.g. Potts and Addenbrooke (1997); Burd et al. (2000); Pickhaver et al. (2010); Amorosi et al. (2014); Losacco et al. (2014); Losacco et al. (2016)), the response of framed buildings have been received only limited attention in the past (e.g., Goh and Mair (2014); Fargnoli et al. (2015); Boldini et al. (2018); Xu et al. (2019); Xu et al. (2020); Xu et al. (2020)). Although the characteristics of the framed buildings must be considered during the evaluation of risk (Cook, 1994; Boone, 1996; Son and Cording, 2005), equivalent beam or plate models characterized by minimal shear flexibility are often adopted (Franzius, 2003; Pickhaver et al., 2010; Maleki et al., 2011; Farrell et al., 2014; Bilotta et al., 2017; Franza and Marshall, 2019).

According to recent studies, the effect of structural details (e.g., building position, presence of masonry infills, openings, and building dimensions) on the soil-structure interaction problem requires further research.

1.2 Problem description

Due to the lack of an experimental investigation on the effect of structural details on the soil-structure interaction problem, the research has focused on the development of numerical models capable of predicting the deformations and damages. The main goal of this research is providing experimental and numerical evidence regarding tunnel-soil-frame building interaction problems for which there is not enough availability of reliable data.

In this study, the numerical simulations were inspired by a set of centrifuge tests performed at the Nottingham University focusing on the response of framed buildings on raft foundations to tunnelling (Xu et al., 2019). A fine dry silica sand, known as Leighton Buzzard Fraction E, was adopted in all the experiments.

This research addresses the response of framed structures to tunnel excavation with 2D and 3D numerical approaches based on the Finite Element method of varying complexity and explores the role played by masonry infills. More specifically, the soil-structure interaction problem is simulated using advanced numerical models (considering the masonry infills, foundations, and the structural members of the building in fair detail and using an advanced elasto-plastic constitutive model for the soil). The soil behaviour is simulated by adopting the SANISAND bounding surface plasticity model originally proposed by Dafalias and Manzari (2004). SANISAND constitutive model is employed to capture the evolution of the displacement field with increasing volume loss. In contrast, a linear elastic constitutive law is adopted for the structural elements (i.e. the frame and the infills).

The thesis aims to investigate how a framed building with masonry infills responds to tunnelling-induced ground movements in terms of foundation and superstructure displacements. In this research, the finite element model was initially validated against available centrifuge data and proved to fairly reproduce the main mechanisms of the soil-structure phenomenon, including the formation of a gap and the relative sliding between the foundation and the soil. As mentioned, SANISAND constitutive model is used for the soil to simulate the tunnel excavation which plays an important role in the compatibility between the

experimental and numerical results. Accordingly, model parameters were preliminary calibrated against available laboratory and centrifuge tests performed on the Leighton Buzzard sand in the framework of other experimental campaigns (Visone and Santucci De Magistris, 2009; Farrell, 2011). Subsequently, an analysis of simulating greenfield conditions was also carried out, to serve as a reference. Afterward, both the cases of a bare frame and of a frame with masonry infills were studied, the latter being the building components most prone to tunnelling-induced damage. In these cases, the effects of structural stiffness and details (such as the presence of masonry infills, openings, building positions, and building dimensions) and variation of volume loss of the tunnel are the main factors in this study on the prediction of deformations and damages induced by tunnelling. Finally, results are summarized in terms of foundation displacements, shear strains for each bay, and maximum tensile strains of the masonry infill walls. Eventually, the maximum tensile strains of infills are used to evaluate the building deformation based on the damage classifications.

1.3 Organization and objectives of the thesis

This dissertation is structured as follows.

- A review of the relevant literature to this research is provided in Chapter 2.
- The centrifuge model, experimental method, and centrifuge tests carried out by researchers at the University of Nottingham are summarised in Chapter 3.
- The Finite Element modelling and the implementation of SANISAND constitutive model are explained in Chapter 4.
- Chapter 5 reports the numerical modelling of tunnel-bare frame interaction performed in PLAXIS 2D and 3D and its comparison with the experimental centrifuge tests .
- In Chapter 6, the effects of volume loss of the tunnel, presence of masonry infills, eccentricity, and dimensions of the building on vertical and horizontal ground movements due to tunnelling in sands are studied. Also, shear strains for each bay and maximum tensile strains of the masonry infill walls are predicted for all cases.
- In chapter 7, the presence of openings in masonry infills is investigated on both structural stiffness and damage.
- Conclusions and recommendations for further research are given in Chapter 8.

Chapter. 2. Soil-structure interaction due to tunnelling

The prediction of building distortion induced by tunnelling construction is nowadays a key issue in the planning process of any new underground projects. The main purpose of the latest studies is related to obtain a better understanding of the mechanism which can predict and control this interaction problem. Firstly, greenfield tunnelling is discussed with reference to tunnelling-induced subsidence and the prediction methods. The subsequent sections discuss the damage estimation for masonry and framed buildings. Finally, the classification of building damage is described for risk assessment.

2.1 Soil and tunnel volume losses

Ground movements are induced by the soil moving towards the drilling machine due to the stress-relief, which results in a ground loss. Generally, ground loss depends on the tunnel construction method (either open-faced or closed-face excavation using tunnel boring machines (TBMs)). There are two key parameters to describe the ground loss in tunnelling: the tunnel volume loss, $V_{l,t}$, and the soil volume loss, $V_{l,s}$, whose concept is shown in Figure **2**.1.

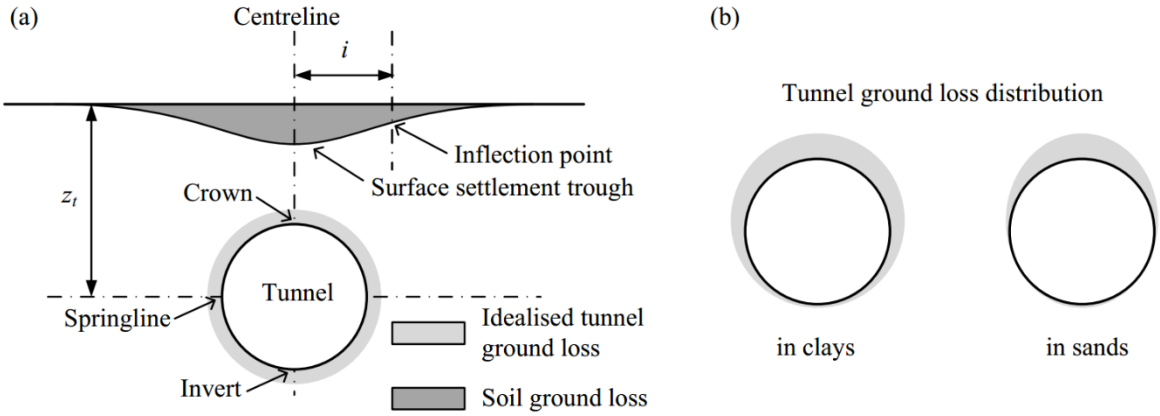

Figure 2**.1.** (a) Illustration of the concept of soil and tunnel volume losses; (b) typical tunnel volume loss distribution for shallow tunnels according to Loganathan and Poulos (1998) and Zhou (2015).

$V_{l,s}$ is the ratio between the volume of the settlement trough per unit length of tunnel, V_s, and the theoretical final area of the tunnel cross section, V_0.

Eq. 2.1 $$V_{l,s} = \frac{V_s}{V_0} \times 100 \qquad [\%]$$

$V_{l,t}$ is the ratio between the ground loss at the tunnel boundary, ΔV, and the theoretical final area of the tunnel cross section, V_0.

Eq. 2.2 $$V_{l,t} = \frac{\Delta V}{V_0} \times 100 \qquad [\%]$$

Both of these key parameters are expressed as a percentage. In a brief description, $V_{l,t}$ is used to describe the magnitude of the tunnel overexcavation and contraction while $V_{l,s}$ is determined based on the field-measured settlements, obtained using instrumentation and monitoring methods.

The distribution of ground loss at the tunnel boundary plays an important role when modelling tunnel excavation. Some analytical approaches assume a uniform convergence around the tunnel; however, this assumption does not describe actual conditions adequately. According to the recent studies, the tunnel volume loss distributions are different in clays and sands. Figure 2.1(b) shows that the actual tunnel ground loss is distributed similar to an elliptical shape in clays, whereas the ground loss is concentrated at the tunnel crown in sands (Rowe and Kack, 1983; Loganathan and Poulos, 1998; Marshall, 2009; Zhou, 2015).

Different volume losses are expected on the basis of the adopted construction method (Mair, 1978; Mair and Taylor, 1997):

- for open face tunnelling, volume losses in stiff clays, such as London Clay, are generally between 1% to 2%.
- construction with sprayed concrete linings (NATM) is effective in controlling ground movements. It is reported in London Clay that the volume losses varying from 0.5%-1.5%.
- for closed tunnelling with pressurised face, a high degree of settlement control can be achieved, using earth pressure balance (EPB) or slurry shields, particularly in sands where volume losses are often as low as 0.5%. The volume losses of only 1%-2% have been reported in soft clays (excluding consolidation settlements). Volume losses may be higher in mixed face conditions for EPB or slurry shields, particularly where sands or gravels overlie stiff clays.

As an example, Figure 2.2 illustrates the variation of volume losses during tunnelling works for the tunnels of the channel rail link (CTRL) in London using earth pressure balance (EPB)

machine. These results refer to approximately 34km of 8.15m outer diameter tunnel bored through a variety of soils.

In London Clay, the short-term subsurface ground displacements are measured from the construction of the twin-bore Crossrail tunnels by EPB machines. Subsurface ground displacements were measured with surface monitoring by precise levelling and micro-meter stick measurements to provide absolute displacements. Clear insights were gained into subsurface displacement mechanisms: an 'inward' displacement field was observed around the cross-rail tunnel construction, in contrast to the 'outward' displacement field that developed around the shallower Channel tunnel rail link (Wan et al., 2017).

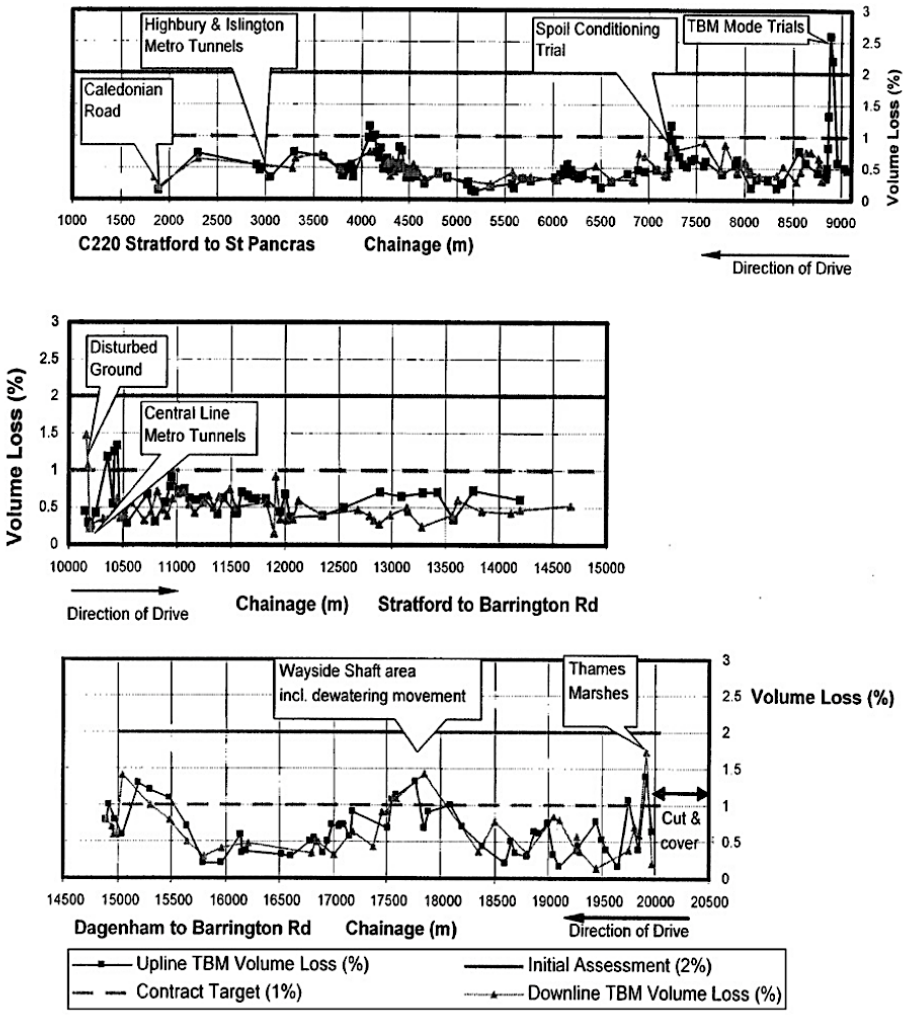

Figure 2.2. Volume losses observed on London tunnels of the channel rail link (CTRL) (Leca and New, 2007).

In another example, relative to the excavation by an EPB machine of the metro line 5 in Milan in sands and gravels, an average volume loss of 0.5% was achieved (Boldini et al., 2016).

2.2 Greenfield tunnelling-induced subsidence

The construction of a tunnel causes both settlements (S_v) and horizontal (S_h) displacements in the ground. “Greenfield” conditions indicate a tunnelling scenario without nearby surface or buried structures. The resulting three-dimensional ‘settlement trough’ induced at the surface by tunnelling is shown in Figure 2.3. To simplify the three-dimensional distribution of ground movements in Figure 2.3, x, y and z directions are used to show the transversal, longitudinal and vertical settlements, respectively. Engineers tend to study the distribution of ground movements considering the two-dimensional cross sections corresponding to the transverse and longitudinal planes defined with respect to the tunnel axes.

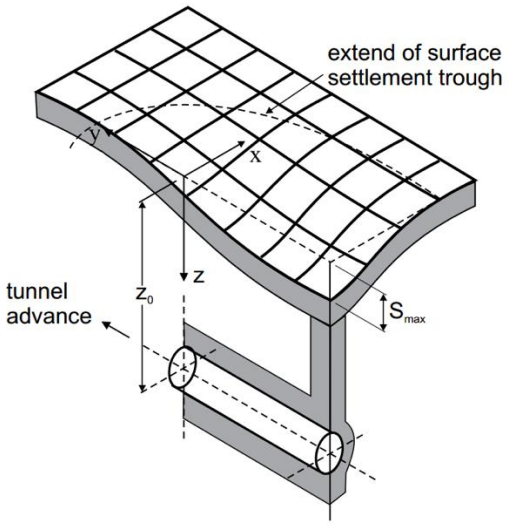

Figure 2.3 Tunnel induced settlement trough after Attewell et al. (1986).

The assessment of greenfield settlements is often carried out by adopting empirical and semi-empirical expressions calibrated on the basis of on-site measurements. For simplicity, the final steady-state settlement distribution transverse to the tunnel axis is often approximated to a Gaussian distribution curve. Figure 2.4 illustrates an idealized transverse settlement trough approximated by a Gaussian curve (Peck, 1969), as a function of the horizontal offset *x*:

Eq. 2.3
$$S_v = S_{v,max} \,.\exp\left(-\frac{x^2}{2{i_x}^2}\right)$$

where $S_{v,,max}$ is the maximum settlement on the tunnel centre-line and i_x is the horizontal distance from the tunnel centre-line to the point of inflection of the settlement trough. O'Rrielly and New (1982) proposed a linear relationship between distance of deflection (i_x) and tunnel depth (H):

Eq. 2.4 $$i_x = K \, . \, H$$

where *K* depends on the soil type; *K*=0.4-0.5 for stiff clays, *K*=0.6-0.7 for soft silty clays, and *K*=0.2-0.3 for coarse-grained soils above water table level.

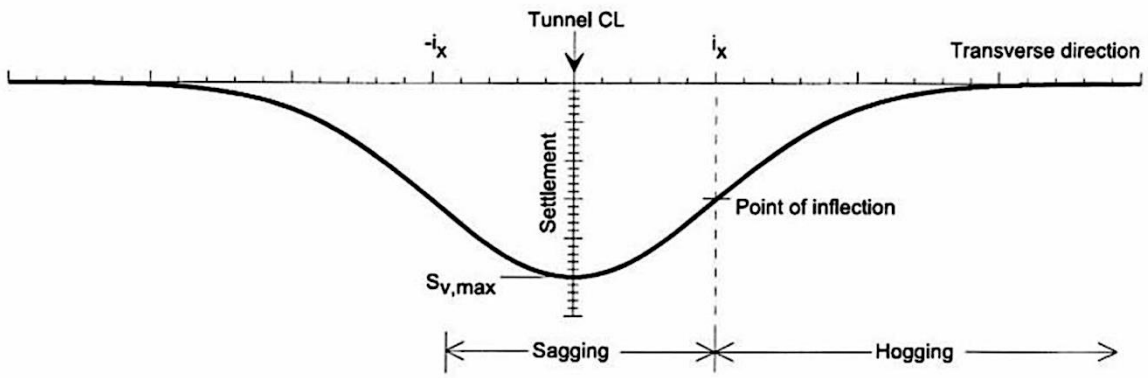

Figure 2.4. Gaussian curve used to describe the transverse settlement trough (Franzius et al., 2006).

The volume of the settlement trough per unit length of tunnel, V_s , is obtained by integrating the Gaussian curve as follows

Eq. 2.5 $$V_s = \int_{-\infty}^{\infty} S_V \, dx = \sqrt{2\pi} \, i_x \, S_{v,max}$$

$S_{v,max}$ can be easily derived from Eq. 2.5:

Eq. 2.6 $$S_{v,max} = \frac{V_s}{\sqrt{2\pi} \, i_x}$$

Eq. 2.7 $$V_{l,s} = \frac{V_s}{A} \times 100$$

Eq. 2.5 can be inserted in the Eq. 2.3 to express the settlement profile as a function of the volume loss:

Eq. 2.8 $$S_v(x) = \frac{V_{l,s}}{\sqrt{2\pi} \, i_x} \exp\left(-\frac{x^2}{2{i_x}^2}\right)$$

As far as the *y*-axis is concerned, the maximum settlement recorded along the longitudinal section (*y* and *z* axes, with *x* = 0) can be expressed by the integral form of the Gauss function, indicated by the term $F(y)$ (Figure 2.5). Attewell (1982) proposed the distribution in y direction with a function $F(y)$, where the parameter i_y is having the same meaning of i_x. The value of $F(y = 0)$, in correspondence to the tunnel face, is 50% of the maximum settlement (Figure 2.5).

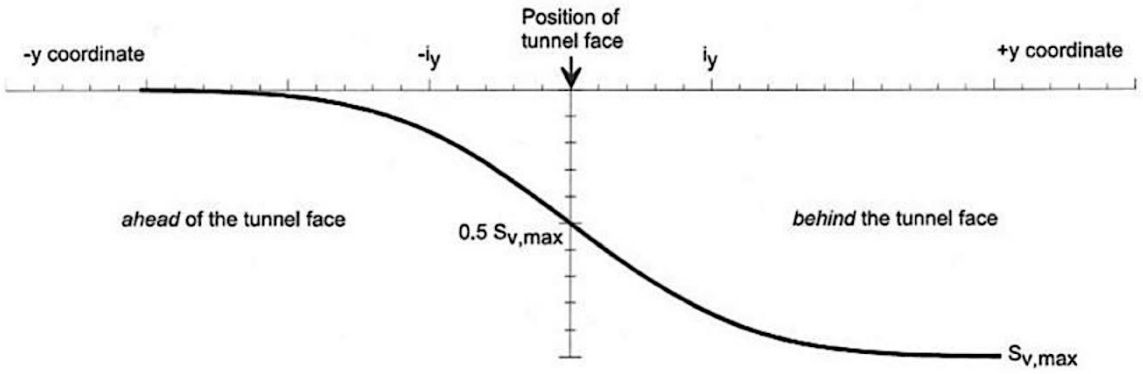

Figure 2.5. Longitudinal settlement trough (Franzius et al., 2006).

Finally, the subsidence curve can be expressed by the general expression:

Eq. 2.9 $$S_v(x,y) = S_{v,max}\, F\left(\frac{y}{i_y}\right) \exp\left(-\frac{x^2}{2{i_x}^2}\right)$$

Besides the vertical displacements, building damages can also be caused by horizontal tensile strains which result from horizontal movements of ground surface. However, there are uncertainties in the estimation of greenfield horizontal movements because of the lack in monitoring data. In this way, the horizontal displacement, S_h, is related to S_v by:

Eq. 2.10 $$S_h = \frac{S_v.x}{H}$$

from which it follows that

Eq. 2.11 $$S_h(x) = \frac{S_v.x}{H} = \frac{x}{H}\frac{V_s}{\sqrt{2\pi}\, i_x} \exp\left(-\frac{x^2}{2{i_x}^2}\right)$$

Horizontal strains are obtained by deriving the previous expression:

Eq. 2.12 $$\varepsilon_h(x) = \frac{\partial S_h}{\partial x} = \frac{S_v.}{H}\left(\frac{x^2}{{i_x}^2} - 1\right)$$

The distribution of horizontal and vertical displacements as well as of horizontal strains is plotted in Figure 2.6. In this figure, it can be observed that the maximum horizontal displacement occurs at the inflection point of the settlement curve. The curvature of the settlement curve defines two distinct areas at the ground surface, respectively named hogging and sagging zones (Figure 2.7).

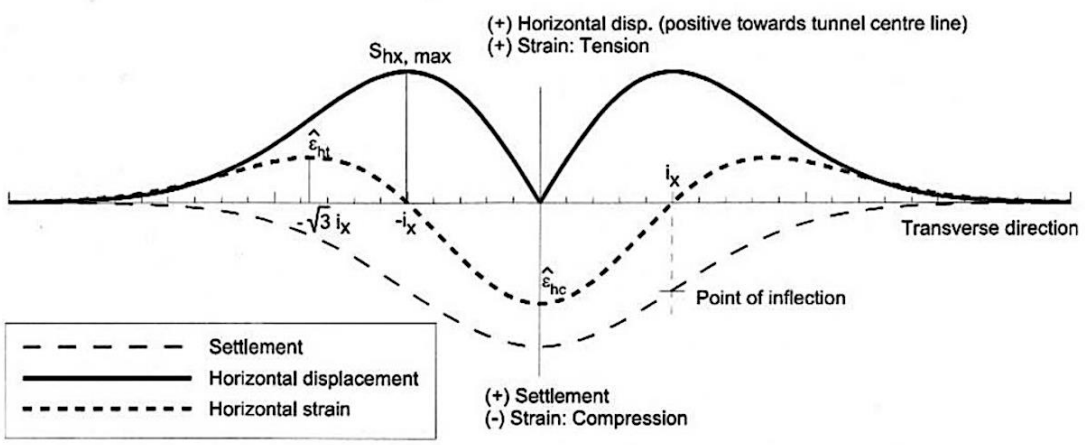

Figure 2.6. Distribution of settlements, horizontal displacements, and strains after Franzius et al. (2006).

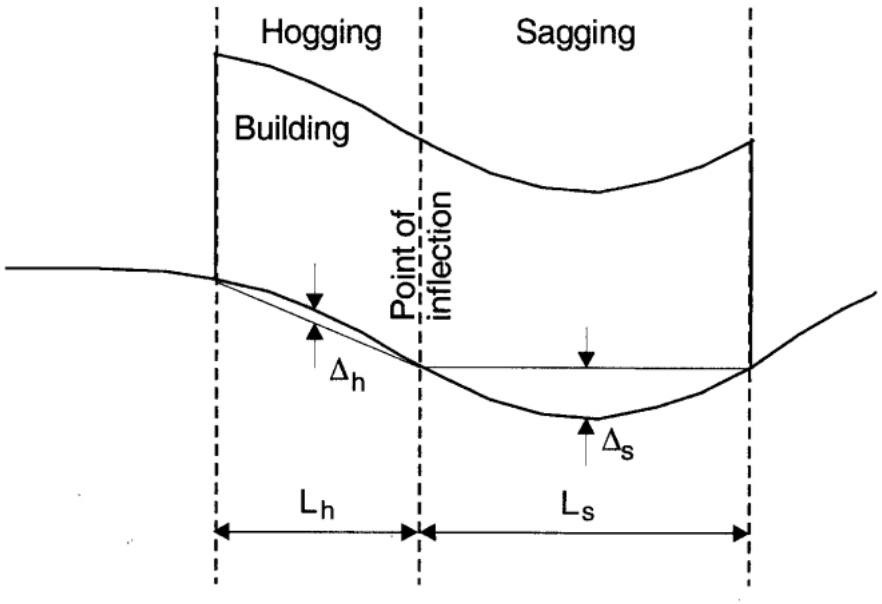

Figure 2.7. Definition of hogging and sagging zones (Franzius et al., 2006).

2.3 Estimated damage for buildings

The excavation of a new tunnel will generate ground movements that can detrimentally affect existing structures, including buildings. It should be recognized that the building and the ground interact with each other in a complex soil-structure interaction problem; typically, the stiffness of the existing structure reduces its resulting deformations.

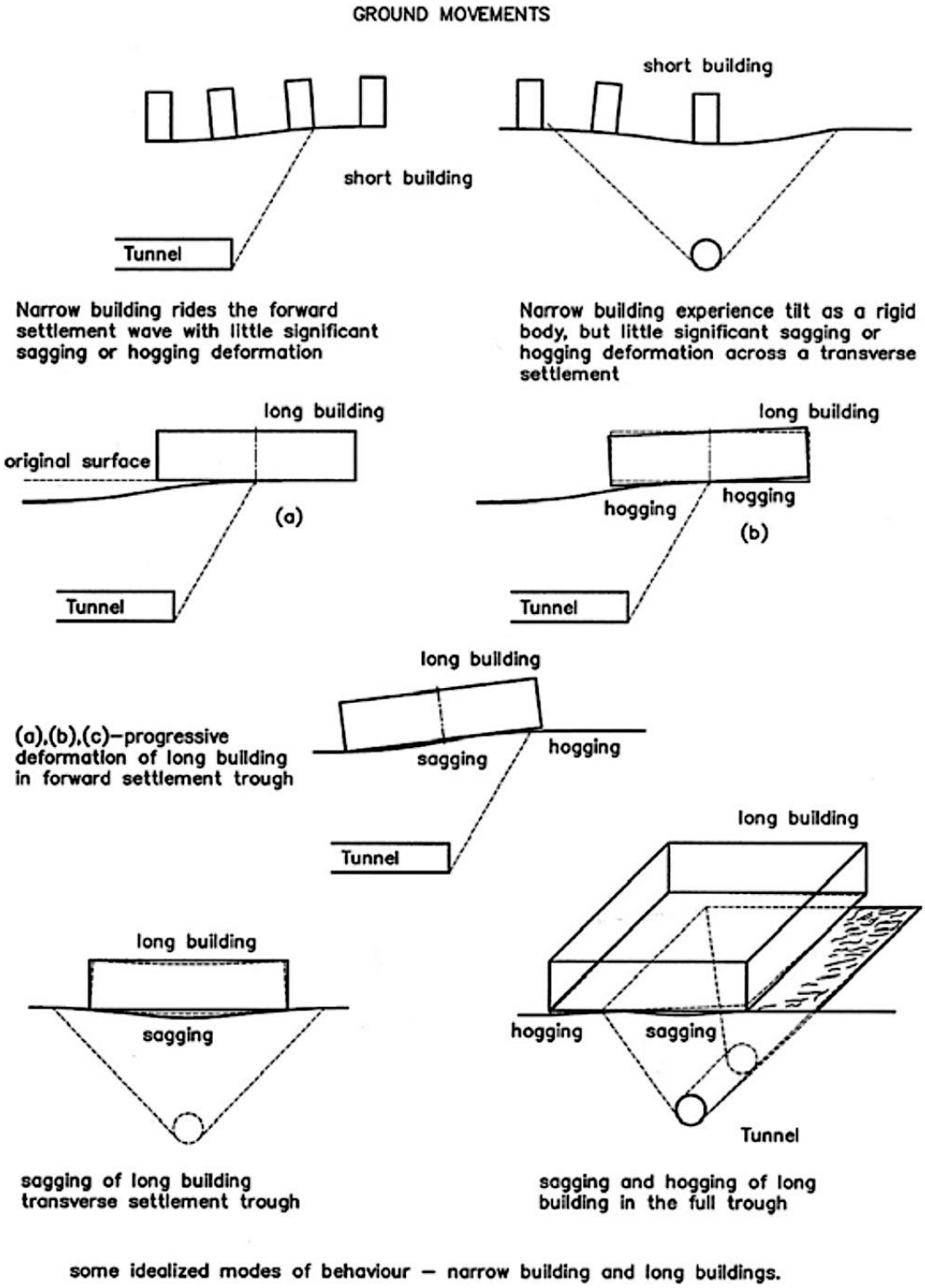

Figure 2.8. Typical idealized building response (Attewell et al., 1986; Leca and New, 2007).

Existing structures can be masonry structures and framed structures (e.g., steel and reinforced concrete structures). For frames, structures will have a high level of bending stiffness and tend

to be subjected to shear rather than bending. The building height (number of floors), the building length (short and long buildings), the number of openings, the type of structure (concrete walls, beams and pillars, etc.) and eccentricity play the most important role on the response pattern. Figure 2.8 illustrates some idealized response patterns have been sketched for typical building configurations, either narrow or long, and in relation to their location with respect to the settlement trough.

The following types of movements can occur in a structure located in the vicinity of a tunnel:

- uniform settlements (or heave)
- differential settlements (or heave) between supports
- overall or differential rotation
- overall horizontal displacements
- differential horizontal displacement in compression or extension

The current design approaches to assess the potential damage to buildings consider that the structure conform to the greenfield displacements (Burland, 1977; O'Rrielly and New, 1982; Boscardin and Cording, 1989; Burland, 1997). More refined analyses can be made by taking into account the buildings in a simplified fashion with equivalent beams or solids (Potts and Addenbrooke, 1997; Franzius et al., 2006; Pickhaver et al., 2010; Maleki et al., 2011; Farrell et al., 2014; Losacco et al., 2014) or in details in the context of advanced numerical analyses (Amorosi et al., 2014; Fargnoli et al., 2015; Bilotta et al., 2017; Boldini et al., 2018).

This section reviews previous studies on soil-structure interactions due to the tunnelling and its effects on structures with shallow foundations.

2.3.1 Building deformation parameters

Tunnel excavation causes vertical and horizontal movements at the foundation level that results in load redistributions, structural damage and strain variation within the structure. Eventually, structures can experience local cracks and loose the bearing capacity of the structural elements. The main deformation parameters to be considered are listed as bellow and illustrated in Figure 2.9:

- settlement, S_v
- maximum relative settlement, $\delta S_{v,max}$
- rotation, $\theta_{i,j}$: the angle between two points and the horizontal line.

- angular strain, α_i : the difference between two slopes at edges of one point.
- angular distortion (or relative rotation), $\beta_{i,j}$: the rotation of the straight line connecting two points relative to their tilt.
- relative deflection, Δ_{max} : defined with respect to a line connecting two points is the maximum distance between the settlement curve and the straight line.
- deflection ratio, $DR = \Delta_{max}/L$: the ratio between the relative deflection between two points and their horizontal distance.
- tilt, ω : the rigid body rotation of the entire structure or part of it.

Figure 2.10 shows the definition of these deformation parameters in hogging and sagging zones.

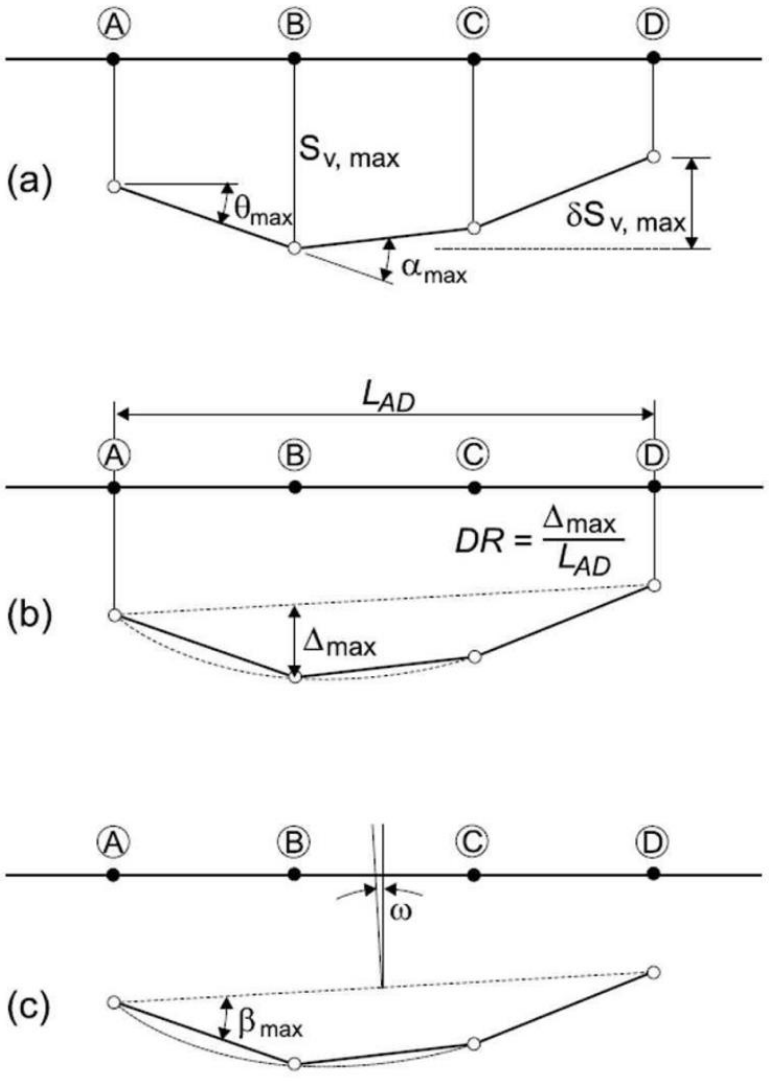

Figure 2.9. Definition of building deformation parameters [After (Burland, 1977)].

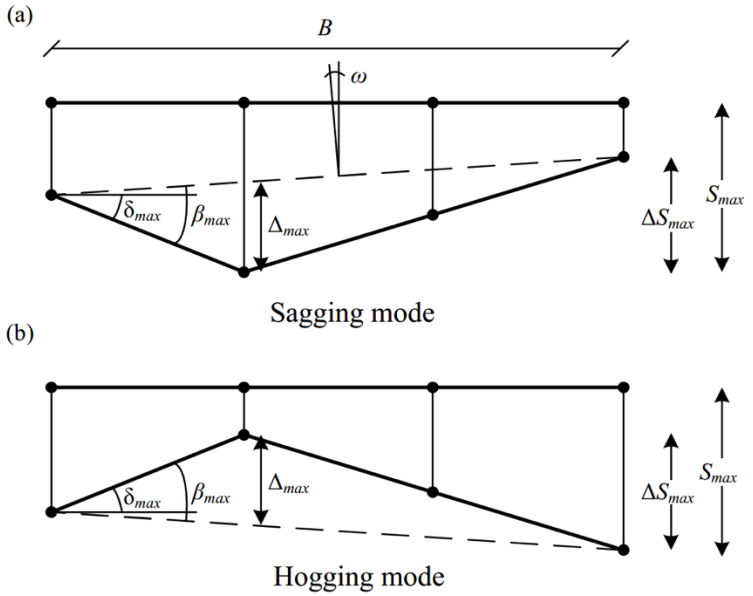

Figure 2.10. Definition of building deformation parameters in (a) sagging (b) hogging (Franza, 2017).

2.3.2 Deformation parameters in masonry structures

The deformation mechanism of the structure should be completely evaluated to determine the response of structures due to tunnelling. For this reason, tunnelling engineers usually assess the tensile strain in structural elements and evaluate the risk of damage in the building. Mair et al. (1996), Burland (1977) and Boscardin and Cording (1989) provided the standard procedure for preliminary risk assessment of surface structures to tunnelling-induced movements.

By idealizing the structure as an equivalent weightless, linear-elastic, and isotropic beam, Burland (1977) calculated the maximum extreme bending strain, ε_{bmax}, and the shear (or diagonal) strain, ε_{dmax}, from the deflection ratio, $DR = \Delta/L$ for a hogging or sagging deflected shape. In this method, the equivalent beam is supposed to have a length, *L*, height, *H*, and unit thickness. Figure 2.11 illustrates the shape of equivalent beam model with its possible modes of deflection including bending and shear.

In most structures, the equivalent beam deflects in a combined mode of bending and shearing. Timoshenko (1957) introduced a formula to compute the total midspan deflection, Δ, for the case of a simply supported beam with a central load:

Eq. 2.13 $$\Delta = \frac{PL^3}{48EI}\left[1 + \frac{18EI}{L^2HG}\right]$$

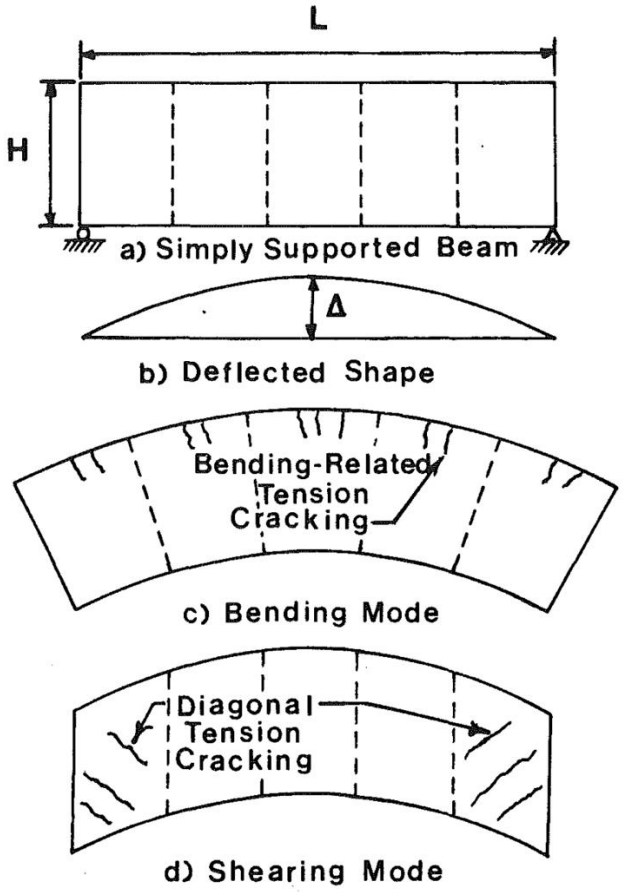

Figure 2.11. An equivalent beam idealization with the possible modes of deflection on cracking (Boscardin and Cording, 1989).

In the hogging zone, the neutral axis can be set at the lower edge of the beam model because the foundations are likely to offer considerable restraint causing the neutral axis to move downwards. Burland and Wroth (1975) suggest to assume the neutral axis should be located at the middle and bottom of the beam in the hogging and sagging zone, respectively, to empirically account for the higher potential for damage associated with the hogging deformations. This equation is adopted by Burland and Wroth (1975) to relate the deflection ratio to the maximum bending strain as follow:

Eq. 2.14 $$\frac{\Delta}{L} = \left[0.083\frac{L}{H} + 1.3\frac{H}{L}\right]\varepsilon_{bmax}$$

In a similar way, the deflection ratio can be related to the maximum shear strain:

Eq. 2.15 $$\frac{\Delta}{L} = \left[0.064\frac{L^2}{H^2} + 1\right]\varepsilon_{dmax}$$

These relations are plotted in Figure 2.12 based on Eq. 2.14 and Eq. 2.15 for structures with different L/H ratios. Plots of Eq. 2.14 and Eq. 2.16 are shown in Figure 2.12, where the maximum tensile strains, either bending or diagonal tension, are related to the critical tensile

strains These graphs show that when L/H ratios are less than one, the first damage will be in the form of diagonal tension cracking.

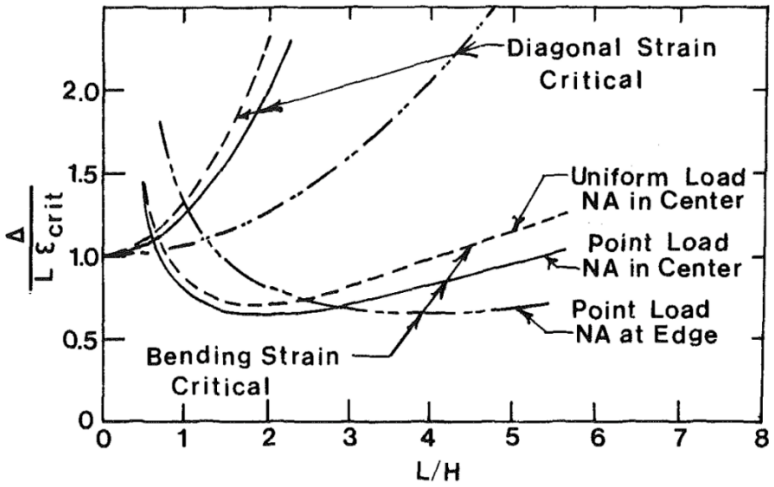

Figure 2.12. Variation of the inflection ratio with the dimensions of the equivalent beam (Boscardin and Cording, 1989).

Boscardin and Cording (1989) proposed that the critical tensile strain, ε_{crit}, can be computed to account also for the horizontal strain:

Eq. 2.16 $$\varepsilon_{crit} = \varepsilon_{bmax} + \varepsilon_h$$

For the case of diagonal tension with horizontal extension, the maximum tensile strain, $\varepsilon_{\theta max}$, can be written as:

Eq. 2.17 $$\varepsilon_{crit} = \varepsilon_{\theta max} = \varepsilon_h cos^2\theta_{max} + 2\varepsilon_{dmax} \cos\theta_{max} \sin\theta_{max}$$

To identify the start of serviceability loss, Burland (1977) firstly used the concept of "limiting tensile strain", ε_{lim}.

Alternatively to the deflection ratio, the angular distortion, β, is the other parameter to evaluate the response of the system. For a simply supported beam with a central point load the maximum change in the slope along the beam (the slope at the support) can be estimated from:

Eq. 2.18 $$\beta = \frac{3\Delta}{L}\left[\frac{1+4\left(\frac{E}{G}\right)\left(\frac{H^2}{L^2}\right)}{1+6\left(\frac{E}{G}\right)\left(\frac{H^2}{L^2}\right)}\right]$$

Son and Cording (2005) investigated several cases of physical model tests, numerical and field observations to investigate the ratios between the angular distortions, β, and the deflection ratio, $\frac{\Delta}{L}$. In summary, they found that the ratio is in the rage 2-4. For elastic conditions (including framed structures), the ratio is approximately equal to 2 and for severe cracking in the structure,

the ratio is around 4. The low ratio of 2 indicates that the distortion in a structure is less than the change in differential ground slope (ΔGS) that would occur in the absence of structure, and the high ratio of 4 has the distortion in a structure being close to differential ground slope (ΔGS) in ground slope (Son and Cording, 2005).

Mair et al. (1996) introduced a two-stage approach to estimate the structural deformations. In the first, conservative, stage, greenfield movements are imposed to the building. In the second phase, if the results of previous phase indicate a not acceptable risk level, soil-structure interaction analyses are performed.

2.3.3 Deformation parameters in framed structures

The equivalent beam method has proven itself over the years to be very reliable for estimating the damage induced on masonry buildings. However, the concepts previously exposed must be revised if the superstructure has a frame configuration.

For a more effective evaluation of building deformations and damages in framed structures, the building is divided into several spans (or units) with equal size, which are composed of beams (or pillars) and wall panels. Cook (1994) mentions that each structure can have one or more floors and be composed of several spans. For better understanding the type of movements in each part of the building, Figure 2.14 shows the deformation parameters used to describe the response of the frame to the movements induced by the tunnelling. The deformation parameters for framed buildings are developed and studied in more detail (Xu et al., 2020):

- The sagging and hogging deflection ratios $DR_{sag/hog}$ could be computed from the maximum deflections $\Delta_{sag/hog}$ and lengths of the sagging/hogging zones $B_{sag/hog}$. In this case, the sagging profile is divided into sagging (compression deformations) and hogging (extension deformations) zones (Burland, 1977; Mair et al., 1996).
- The angular distortion β of each bay is the rotation of the straight line concerning two points relative to their local tilt (Boscardin and Cording, 1989).
- The longitudinal strain, ε_{xx}, is related to axial and bending stresses. This parameter is negligible in frames with continuous foundations because of the axial slabs and foundation stiffness.
- The diagonal deformation, ε_{xz}, generated by shear stresses and normally related to the shear deformations γ of each span (Figure 2.13).

The diagonal deformations, ε_{xz}, are instead determined starting from the shear deformation recorded on each single span:

Eq. 2.19 $$\varepsilon_{xz} = \frac{\gamma}{2}$$

where precisely γ is the shear deformation angle (Figure 2.13), approximately equal to the angular distortion β (Ritter et al., 2020).

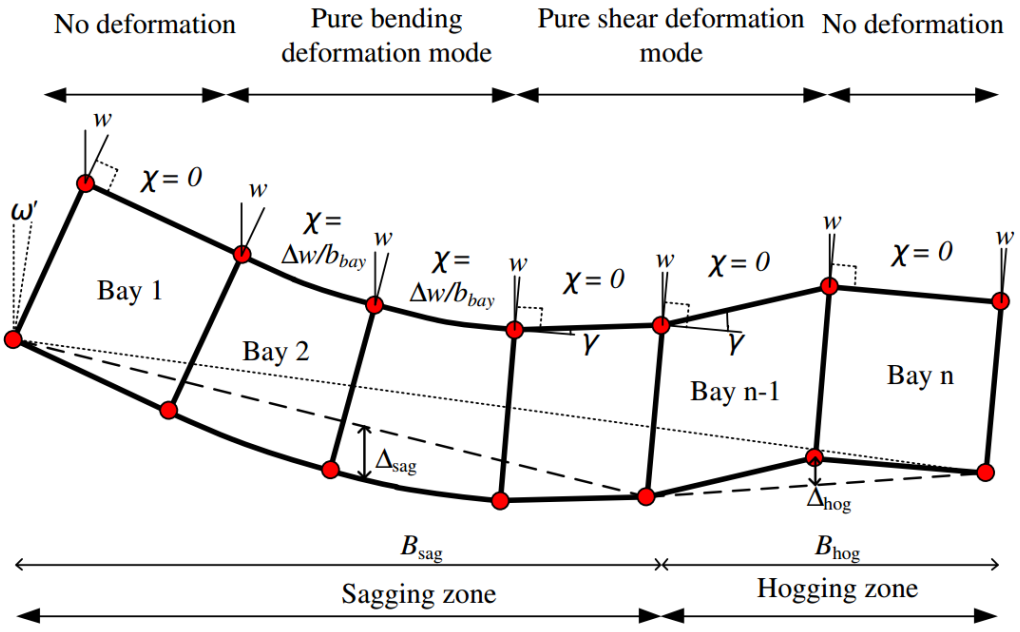

Figure 2.13. Distortions of a building due to settlements and illustration of deformation parameters (Xu et al., 2020).

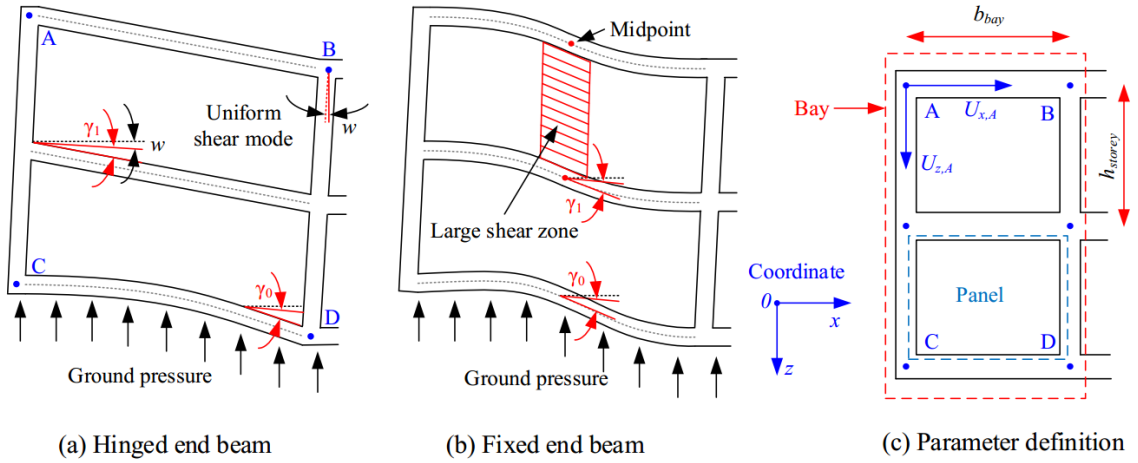

(a) Hinged end beam (b) Fixed end beam (c) Parameter definition

Figure 2.14. (a) and (b) bay distortion modes; (c) parameter definition (Xu et al., 2020).

The maximum tensile strains can be determined using Eq. 2.20 and Eq. 2.21(Mair et al., 1996), based on a Mohr's circle of strain for a plane-stress or plane-strain condition, respectively, where ε_{xx} is longitudinal strain due to axial and bending deformations associated with curvature χ, ε_{xz} is diagonal strain due to shear deformations associated with shear strain γ, and ν is Poisson's ratio.

Eq. 2.20 $$\varepsilon_{max} = \frac{\varepsilon_{xx}(1-\nu)}{2} + \sqrt{\frac{1}{4}\varepsilon_{xx}^2(1+\nu)^2 + \varepsilon_{xz}^2}$$

Eq. 2.21 $$\varepsilon_{max} = \frac{\varepsilon_{xx}}{2} + \sqrt{\frac{1}{4}\varepsilon_{xx}^2 + \varepsilon_{xz}^2}$$

Boone (1996) evaluated damage in terms of cumulative crack width determined from strains. Son and Cording (2005) assimilate the building to a set of units or portions (Figure 2.14(c)), avoiding the dependence of the parameters β and ε_h on the geometric characteristics of the structure. A direct and effective approach is therefore defined to determine the response of each substructure by simply measuring the displacements at the four vertices of each span (*A*, *B*, *C* and *D* in Figure 2.14(c)), namely the bay analysis adopted in this thesis.

Son and Cording (2005) summarized the generalized damage criterion referring to a vertex of a single unit (Figure 2.15). The criterion is based on the concept that a structure is deformed by the combination of angular distortion, lateral strain, and the maximum strain on the structure. Son and Cording (2005) subdivided a building adjacent to a deep excavation into bays based on the location of intermediate walls, building columns, different structural properties (e.g., geometry or stiffness) or gradient of ground displacements.

The angular distortion and lateral strain for building damage estimate can be determined by measuring vertical and horizontal displacements at the corners, *A*, *B*, *C*, and *D* of a building unit (Figure 2.14(c)). This criterion has the following steps:

1- a structure is deformed by the combined action of β and ε_h.
2- β and ε_h are determined by considering the vertical and horizontal displacements of the edges of a building unit.
3- the maximum principal deformation ε_{max} of the structure is obtained by a combination of β and ε_h.
4- the maximum main deformation is compared with the categories of damage.

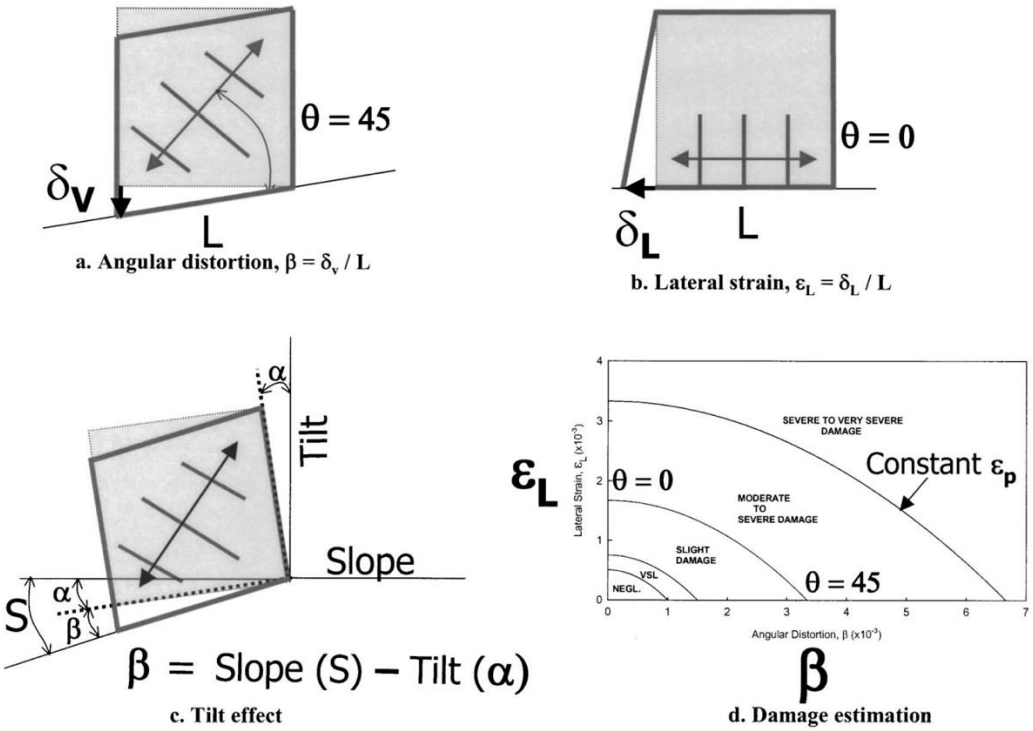

Figure 2.15. State of strain at point or average state of strain in distorting portion of structure (Son and Cording, 2005).

The combination of angular distortion and lateral strain at a point or in a building unit results in a maximum principal tensile strain is:

Eq. 2.22 $$\varepsilon_{max} = \varepsilon_p = \varepsilon_L cos^2\theta_{max} + \beta \cos\theta_{max} \sin\theta_{max}$$

in which:

Eq. 2.23 $$\tan(2\theta_{max}) = \frac{\beta}{\varepsilon_L}$$

where θ_{max} is the direction of crack formation and the angle of the plane on which ε_p acts, measured from vertical plane.

It should be noted that when $\beta = 0$, $\varepsilon_{max} = \varepsilon_h$ acts on the vertical plane and therefore $\theta_{max} = 0°$. From the other point of view, if $\varepsilon_h = 0$, $\varepsilon_{max} = \frac{1}{2}\beta$ acts on the plane at $\theta_{max} = 45°$ and a crack forms at $\theta_{max} = -45°$. These possible values indicate $0° < \theta_{max} < 45°$.

Typically, the angular distortion and lateral strains are determined for the section of bay in the first third to one half of the base length where the damage was concentrated. The angular distortion (β) is the shearing distortion of the bay and defined as (Son and Cording, 2005):

Eq. 2.24 $$\beta = Slope - Tilt$$

This formula considers the scheme in Figure 2.14(c) and it is equal to:

Eq. 2.25 $$\beta = S - \alpha = \frac{U_{z,D} - U_{z,C}}{b_{bay}} - \frac{U_{x,A} - U_{x,C}}{2h_{storey}}$$

where $U_{i,j}$ represents the horizontal and vertical displacements of the corners in which $i = x; z$ is the displacement direction, and $j = A; B: C; D$ is the location of the bay corner. Indeed, *C* and *D* are the two lower corners of the base where as *A* and *B* are the upper corners. The other parameters are the lateral strain at the top and base of each bay proposed by Son and Cording (2005). The lateral strain at top, $\varepsilon_{Lat}(T)$, is the change of lateral displacement at the top over the length *L* of the bay. Similarly, the lateral strain at base, $\varepsilon_{Lat}(F)$, is possible to be found. These formulas are:

Eq. 2.26 $$\varepsilon_{Lat}(T) = \frac{U_{x,A} - U_{x,B}}{L}$$

Eq. 2.27 $$\varepsilon_{Lat}(F) = \frac{U_{x,C} - U_{x,D}}{L}$$

Cook (1994) suggests to use top and bottom corner displacement of each bay to isolate tilt, bending displacements, and shear displacements and to estimate the average bay curvature and shear strain from bay corner displacements. Ritter et al. (2020) proposes an analytical procedure to estimate the shear strain or average shear distortion, γ, of a building unit or bay:

Eq. 2.28 $$\gamma = \frac{U_{z,D} - U_{z,C}}{b_{bay}} - \frac{3U_{x,A} - 3U_{x,C} - (U_{x,B} - U_{x,D})}{4h_{storey}}$$

To distinguish between bending and shear displacements (and strains), the framework outlined by Cook (1994) is used (the sign convention and tilt and bending deformations are shown in Figure 2.16). The settlement due to tilt is computed as:

Eq. 2.29 $$S_{v,tilt} = \omega_2 L_u$$

Also, the bending-related settlement is derived as:

Eq. 2.30 $$S_{v,bend} = \chi \frac{L_u^2}{2} = \Delta\omega \frac{L_u}{2}$$

where χ is the average curvature and $\Delta\omega$ is subtraction of ω_1 and ω_2 .

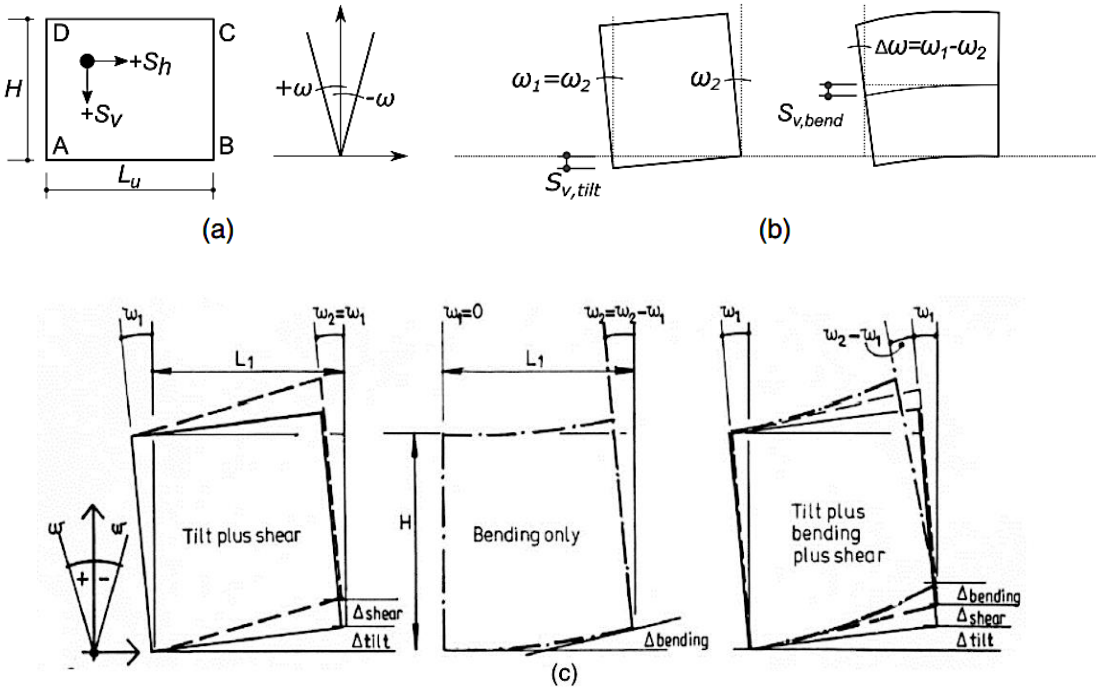

Figure 2.16. Framework to investigate building response after Cook (1994): (a) sign convention and reference condition for bay; (b) tilt and bending deformations; and (c) different contributions of shear, tilt and bending deformations.

2.3.4 Damage prediction with equivalent beam approach

To characterize the effects of building stiffness on the soil-structure interaction, Potts and Addenbrooke (1997) conducted a parametric finite element analysis to investigate the response of buildings to tunnelling. Two parameters were defined to account for the modification to the settlement and the axial response of buildings; they are the relative bending stiffness; ρ^*; and the relative axial stiffness; α^*. ρ^* and α^* were later modified by Franzius et al. (2006), the former to be dimensionless. The relative bending stiffness and the relative axial stiffness formula, defined by Franzius et al. (2006), are:

Eq. 2.31 $$\rho^*_{mod} = \frac{EI}{E_s B^2 z_0 L}$$

Eq. 2.32 $$\alpha^*_{mod} = \frac{EA}{E_s B L}$$

where EI and EA are the bending stiffness and the axial stiffness of the structure, respectively. E_s is the secant stiffness of the soil at an axial strain of 0.01% and at a depth of $z = z_0/2$. B is the building width and L is the length of the building in the longitudinal direction of the tunnel. The dimensions are illustrated in Figure 2.17.

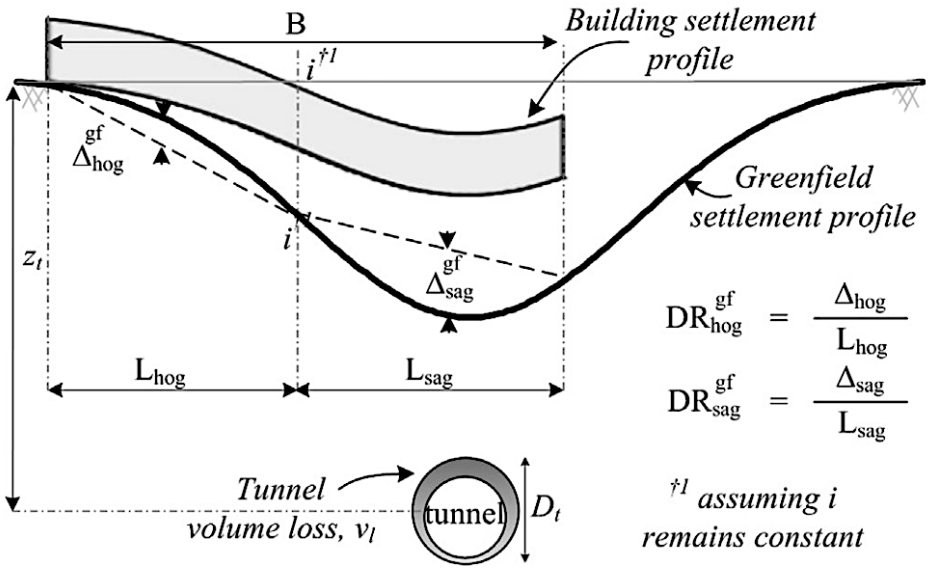

Figure 2.17. Influence of soil-structure interaction on settlement distortions (Farrell et al., 2014).

In the next years, Mair (2013) proposed the relative bending stiffness factors $\rho_{sag/hog}$ as:

Eq. 2.33
$$\rho_{sag/hog} = \frac{EI}{E_s B^3_{sag/hog,gf} L} = \frac{EI^*}{E_s B^3_{sag/hog,gf}}$$

where EI^* is EI per running meter of the building. $B_{sag/hog,gf}$ is the length of building in the sagging/hogging zones defined by the greenfield settlement inflection point. In this equation, EI^* is used to indicate the total building stiffness (e.g. Goh and Mair (2014)) without distinguishing between bending and shear contributions.

Settlement distortions to building are typically measured in both hogging and sagging modes of determination using the deflection ratio (Δ/L or DR, defined in Figure 2.17). The hogging and sagging regions are partitioned by the point of inflexion (i) of the settlement trough, assuming that each building responds fully flexibly. Potts and Addenbrooke (1997) introduced the deflection ratio modification factors $M^{DR,sag}$ and $M^{DR,hog}$, defined as:

Eq. 2.34
$$M^{DR,sag/hog} = \frac{DR_{sag/hog,bld}}{DR_{sag/hog,gf}}$$

where $DR_{sag/hog,bld}$ and $DR_{sag/hog,gf}$ are, respectively, the deflection ratios of the building settlement profile and the greenfield settlement trough.

Modification factors to the greenfield settlement distortions are highly dependent on ρ^*_{mod}. Similarly, the modification to tensile and compressive horizontal strains, in the hogging and sagging regions, respectively, are highly dependent on α^*_{mod} (Franzius et al., 2006).

2.3.5 Response of infills

Masonry buildings and frames with masonry infills suffer different damages due to the horizontal and vertical movements of ground surface. Cracking on infill walls occur due to the deformation of surrounding beams and columns that leads to create tensile strain inside the infills. The deformation in framed buildings is expected to primarily result from differential vertical movement of columns due to the higher tensile strength of framed buildings. Since columns may be in sagging and hogging zones, tilt of the building must also be considered separately and subtracted from the deformation due to differential column settlement. Boone (1996) assumed the tilt equal to the slope of the chord between endpoints of symmetric ground movement profile segments. Figure 2.18 shows the deflected shape of a fixed end beam frame and a simple beam frame. The deflected shape of fixed end beams will resemble an elongated S with an inflection point at the midspan. In this case, the shear strain is $\Delta S/L$; however, the maximum curvature will be on half of beam length. Therefore, in completing analyses of fixed end beams using the above methods, calculation of the L/H ration, radius of curvature, and central deflection must be based on $0.5L$.

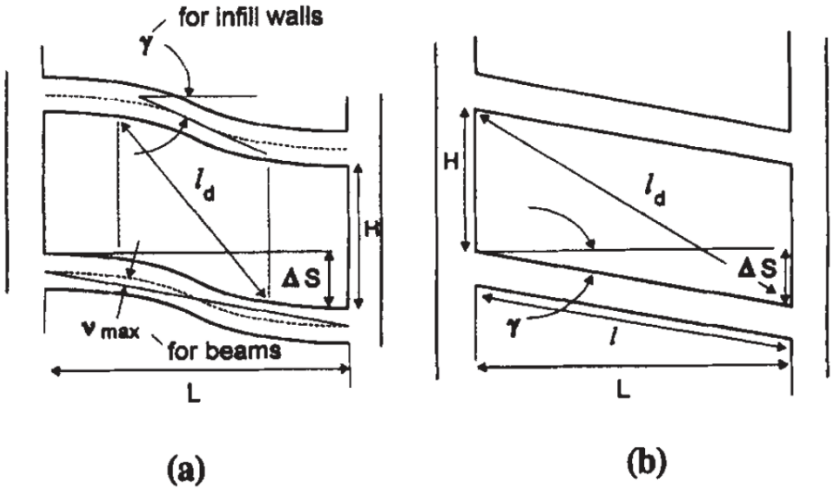

Figure 2.18. Geometry of beams and infill/panel walls: (a) Fixed end beam frame; (b) Simple beam frame (Boone, 1996).

Figure 2.18(a) shows the infill walls bound by fixed-end beams and columns that in this type of deformation it is reasonable to expect that the deformed shape could be approximated as shown in Figure 2.18(a). Since end rotation is restricted and the wall is forced to conform to the beam's deformed shape, the wall itself have greater deformation between the wall quarter points with a maximum shear at the wall midspan equal to $2\Delta S/L$ (excluding tilt). The expected

deformed shape for infill walls supported by simple beams and columns is shown in Figure 2.18(b). In both cases shear is likely be the predominant mode of strain deformation.

Cracks in buildings usually have diagonal patterns for different cases subjected to ground movements and these types of cracks refer to shear cracking.

Cracking of structures deforming principally in shear will likely follow irregular patterns through masonry, mortar joints, and/or other discontinuities along the principle stress trajectories. Although $\varepsilon_p$could be used to approximate the potential crack width and severity, the length over which the strain will occur is difficult to define in simple terms and depends on many factors including height, length, openings, and load-bearing walls and infill walls supported by fixed-end beams may be applied to an equivalent diagonal length based on the building element height and length approximated by:

Eq. 2.35 $$l_d = \sqrt{(l/2)^2 + H^2}$$

and for infill walls supported by simple beams

Eq. 2.36 $$l_d = \sqrt{l^2 + H^2}$$

Recent studies in the last few decades investigated the response of infilled frames both in terms of their global and local behaviour. In the first elastic phase, by increasing the loads due to the ground movements, the first cracks in the infills lead to separation from the frame, and a compression strut mechanism occurs. Figure 2.19 shows four mechanisms were identified in the masonry infilled frames, depending on the mechanical properties of masonry and on the relative panel-to-frame stiffness. The main failure modes, which were introduced by Blasi et al. (2018), consist of: (1) mid-height cracking, (2) diagonal cracking, (3) horizontal slip and (4) corner crushing.

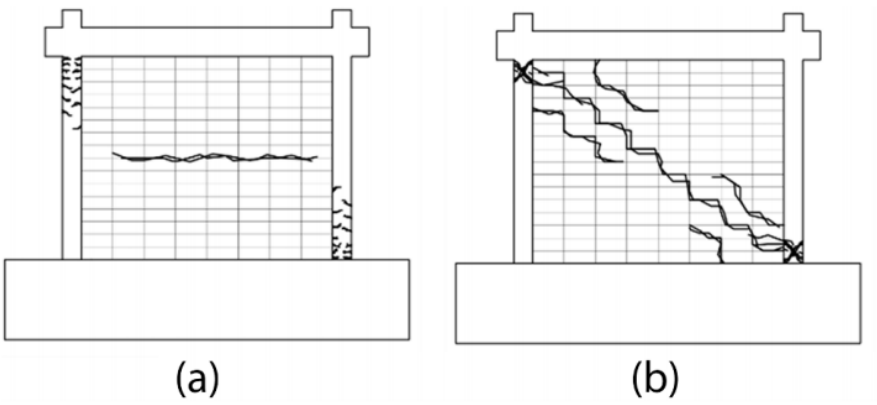

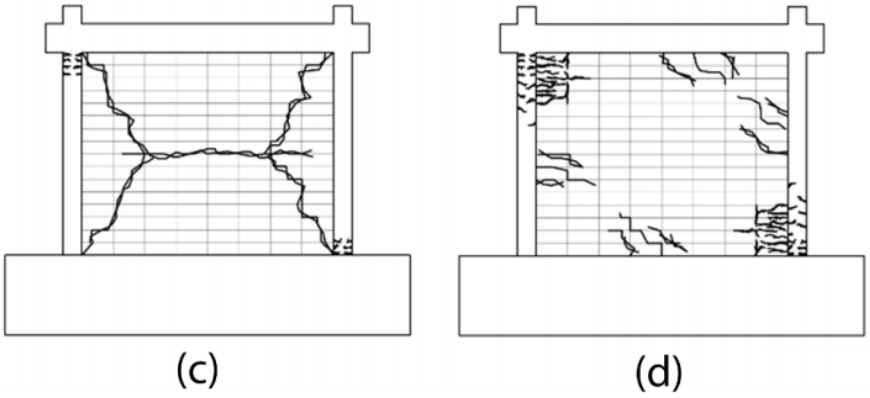

Figure 2.19. Failure mechanisms of infills (a) mid-height sliding, (b) diagonal cracking, (c) bed joint cracking, and (d) corner crushing (Blasi et al., 2018)

2.4 Risk assessment

Protection of adjacent or overlying structures occupies a major part of the cost, schedule, and third-party impacts of an urban underground construction. Risk assessment is the most important work of engineers to do during the analysis and evaluation of damages for the design of structures which are exposed to the shallow tunnelling. Methods used to limit damage or mitigate their effects include limiting movements at the excavation source with controlled construction measures, improve ground characteristics or using compensation methods to replace ground loss, underpinning reinforcing, repairing, or replacing structures. Predicting and then monitoring building performance is a key aspect in planning, design, and implementation of such measures.

Son and Cording (2005) developed a procedure to estimate the building damage induced by ground movements (Figure 2.20). The procedure starts from a conservative screening that eliminates from further study buildings that do not fall within a significant damage category using even the conservative estimate. This procedure allows a number of buildings in urban areas to be investigated in a limited time.

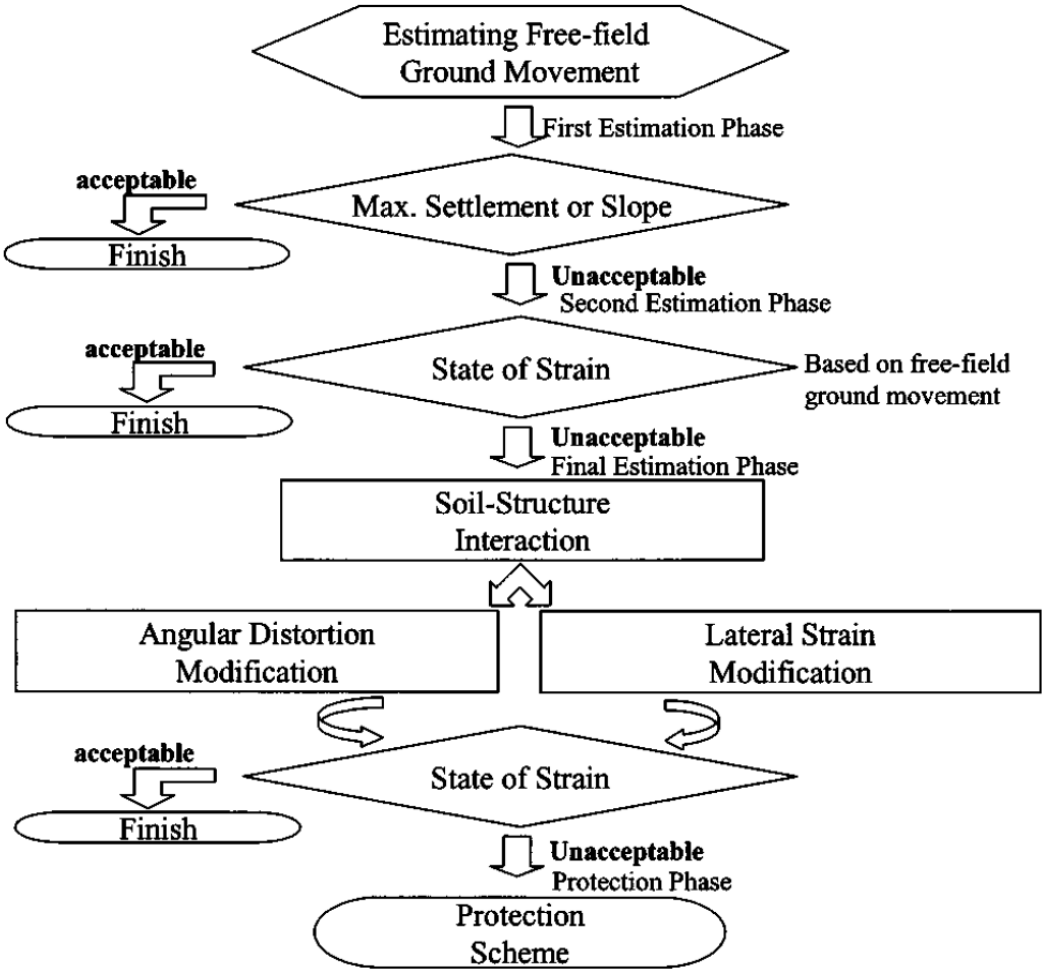

Figure 2.20. Procedure for building damage estimate to excavation-induced ground movement (Son and Cording, 2005).

2.4.1 Damage classification

Classification of building damage has been traditionally divided into three categories such as architectural damage, functional damage, and structural damage. Architectural damage affects the appearance of structures and is related to cracks or separations in panel walls and doors. Functional damage affects the use of the structure, and is exemplified by jammed doors and windows, extensively cracked and falling plaster, tilting of walls and floors, and other damage that would require non-structural repair to return the building to its full-service capacity. Structural damage affects the stability of the structure, usually related to cracks or distortions in primary support elements such as beams, columns and load bearing walls (Boscardin and Cording, 1989).

There are several levels in evaluating the effect of ground movements on building performance (Boscardin and Cording, 1989). An initial screening determines the potential affected structures along the project alignment by considering the width, maximum settlement, and ground slope of the free-field trough. Table 2-1 summarises different categories of risk based on the maximum slope and settlement of building (Rankin, 1988; Boscardin and Cording, 1989).

Table 2-1. Typical values of maximum building slope and settlement for damage risk assessment [after Rankin (1988) and Son and Cording (2005)].

Risk category	Maximum slopes of building	Maximum settlement of building (mm)	Description of risk
1	Less than 1/500	Less than 10	Negligible: superficial damage unlikely
2	1/500-1/200	10-50	Slight: possible superficial damage which is unlikely to have structural significance
3	1/200-1/50	50-75	Moderate: expected superficial damage and possible structural damage to buildings, possible damage to relatively rigid pipelines
4	Greater than 1/50	Greater than 75	High: expected structural damage to buildings. Expected damage to rigid pipelines, possible damage to other pipelines

Burland (1997) presented a table of damage category according to crack width (see Table 2-2). The adopted classification provides five categories, ranging from negligible (category 0) to severe damage (category 5). These categories were correlated to a range of limiting tensile strains by Boscardin and Cording (1989). Mair et al. (1996) stressed the importance of the transition from category 2 to category 3, with the latter category often associated with relevant tunnelling-induced damage.

If the predicted degree of damage falls into the first three categories from 0 to 2, the risk is considered low. At these degrees of damage, the structural integrity is assured, and the damage can be easily and economically fixed. A major objective of designers is to maintain the level of risk below the category 3, as this is considered safe threshold for all buildings.

Table 2-2. Damage classification system proposed by Burland (1997) and Boscardin and Cording (1989).

Category of damage	Damage class	Description of typical damage and ease of repair	Approx. crack width (mm)	Limit. tensile strain levels
Aesthetic damage	Negligible	Hairline cracks of less than about 0.1 mm width.	up to 0.1 mm	0 -0.05
	Very slight	Fine cracks which can easily be treated during normal decoration. Perhaps isolated slight fracturing in building. Cracks in external brickwork visible on close inspection.	up to 1 mm	0.05 –0.075
	Slight	Cracks easily filled. Redecoration probably required. Several slight fractures showing inside of building. Cracks are visible externally and some repainting may be required externally to ensure water tightness. Doors and windows may stick slightly.	up to 5 mm	0.075– 0.15
Functional damage, affecting serviceability	Moderate	The cracks require some opening up and can be patched by a mason. Recurrent cracks can be masked by suitable linings. Repainting of external brickwork and possibly a small amount of brickwork to be replaced. Doors and windows sticking. Service pipes may fracture. Weather-tightness often impaired.	5 to 15 mm or a number of cracks > 3 mm	0.15 –0.3
	Severe	Extensive repair work involving breaking out and replacing sections of walls, especially over doors and windows. Windows and door frames	15 to 25 mm, but also depends on	> 0.3

		distorted, floors sloping noticeably. Walls leaning or bulging noticeably, some loss of bearing in beams. Service pipes disrupted.	number of cracks	
Structural damage, affecting stability	Very severe	This requires a major repair involving partial or complete rebuilding. Beams loose bearing, walls lean badly and require shoring. Windows broken with distortion. Danger of instability.	usually > 25 mm, but depends on number of cracks	> 0.3

Chapter. 3. Geotechnical modelling in centrifuge tests

Nowadays, physical modelling is an increasingly used approach in the engineering field, which includes a set of methodologies to study the real behaviour of soil and structures by using prototypes and small models. In tackling some complex geotechnical problems, centrifuge modelling is often considered as a preferred experimental method.

Geotechnical centrifuge modelling is a technique for testing physical scale models of geotechnical engineering systems. A geotechnical centrifuge is used to conduct model tests to study geotechnical problems such as the bearing capacity of foundations for bridges and buildings, settlement of embankments, stability of slopes, earth retaining structures, the effect of tunnelling/excavation on adjacent existing underground structures (mechanized or traditional excavation) and the dynamic problems (earthquakes).

This section briefly introduces the use of centrifuge modelling for geotechnical, and more specifically soil-structure interaction, problems. A brief introduction on the theoretical and practical aspects of geotechnical centrifuge modelling is given followed by a description of the experimental set-ups and investigative techniques implemented today at the University of Nottingham, where experimental results for tunnel-frame interaction were obtained.

3.1 Geotechnical centrifuge

The mechanical principle at the base of centrifuge modelling is simple; if a body of mass m is rotating at constant radius r about an axis with steady speed v (Figure 3.1), in order to keep it in that circular orbit, a constant radial centripetal acceleration v^2/r or $r\omega^2$ (where ω is the swept angular velocity) develops. To produce this acceleration, the body should experience a radial force $mr\omega^2$ directed towards the axis. The centripetal acceleration can be normalized with earth's gravity g and the body is being subjected to an acceleration of ng where $n = r\omega^2/g$.

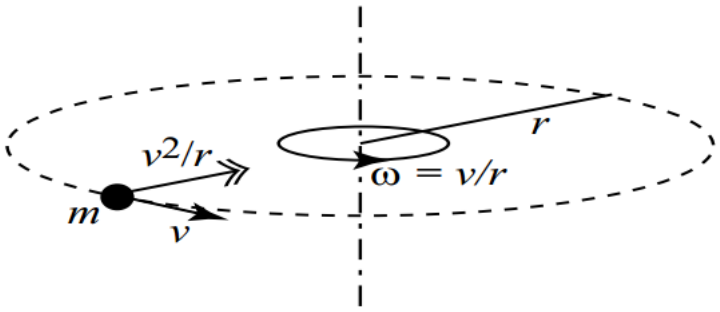

Figure 3.1. Object moving in steady circular orbit (Wood, 2003).

If the equilibrium of an element of unit cross-sectional area and of thickness δ_z taken from a column of soil at the surface of the earth were considered (Figure 3.2(a)), the increase in stress through the element should balance the weight of the element (which itself comes from the gravitational acceleration) in order to prevent any acceleration of the element:

Eq. 3.1 $$\delta\sigma_v = \rho g \delta_z$$

and, considering a constant density, at a depth z below the free surface

Eq. 3.2 $$\sigma_v = \int_0^z \rho g dz = \rho g z$$

In the centrifuge, if the equilibrium of an element of unit cross-sectional area and of thickness δ_z were considered (Figure 3.2(b)), the stress increase should provide the force necessary to generate the centripetal acceleration. The equation of motion becomes:

Eq. 3.3 $$\delta\sigma_v = \rho n g \delta_z$$

and at depth z/n below the free surface (again, assuming a constant density)

Eq. 3.4 $$\sigma_v = \int_0^{z/n} n\rho g dz = \rho g z$$

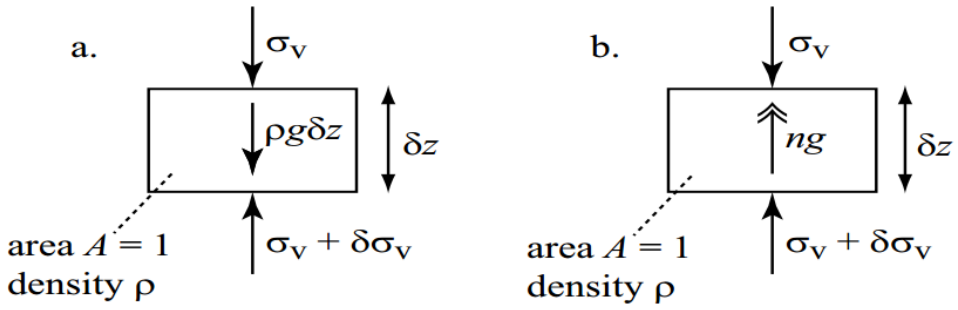

Figure 3.2. Element of soil (a) at surface of the earth and (b) on centrifuge (Wood, 2003).

In the centrifuge tests, a model with geometry of N times smaller than the prototype is constructed and is tested under centrifugal acceleration field with a magnitude of N times the Earth's gravity (Schofield, 1980). A $1/N$-scale model located at a distance, r, from the axis of a centrifuge (Figure 3.3) is rotated at a rotational speed, $\Omega = \sqrt{N/r}$, which is sufficient to raise the acceleration field at the location of the model to N times the acceleration of gravity. In principle, the stress conditions at any point in the model should then be identical to those at the corresponding point in the full-scale prototype. The overall behaviour (e.g., displacements, failure mechanisms, etc.) should also be identical. The gravitational acceleration at the top of the model is lower than that at the bottom of the model due to the fact that the gravitational field increases with radial distance.

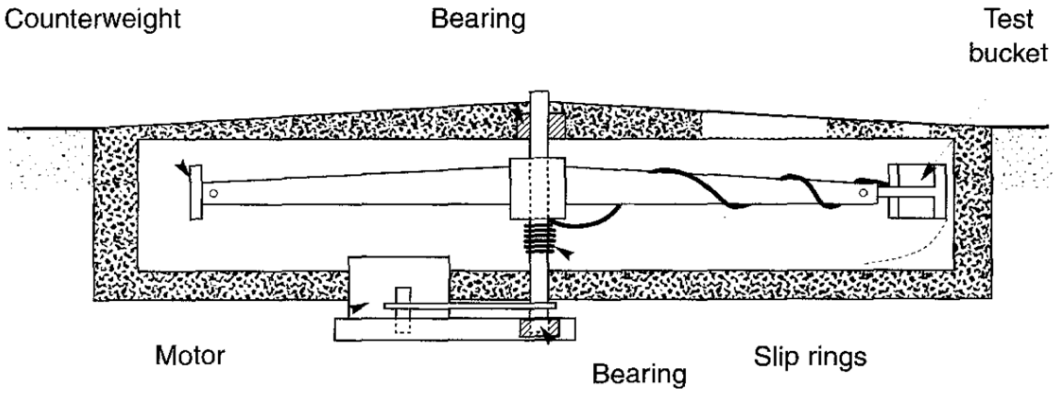

Figure 3.3**.** Cross section through a geotechnical centrifuge (Kramer, 1996).

Similitude considerations play an important role in the planning and interpretation of centrifuge tests. Table 3-1 shows the scaling factors for a number of parameters. The scaling factors show how dynamic events are speed up in the centrifuge. For example, the stresses and strains in a 30-m -high prototype earth dam could be modelled with a 30-cm -high centrifuge model accelerated to 100g.

Obviously, high-speed transducers and data acquisition systems are required to obtain useful results in dynamic centrifuge tests. Since the scaling laws apply to all parts of the model, miniaturized transducers and cables are required to minimize their influence on the response of the model.

Table 3-1. Scaling factors for centrifuge modelling (Kramer, 1996).

Type of event	Quantity	Model Dimension

		Prototype Dimension
All events	Stress	1
	Strain	1
	Length	1/N
	Mass	$1/N^3$
	Density	1
	Force	$1/N^2$
	Gravity	N
Diffusion events	Time	$1/N^2$
	Strain rate	N^2

3.2 Modelling of tunnelling

In geotechnical engineering, the understanding of the behaviour of soils and their interactions with structures induced by tunnelling is often achieved with the use of experimental testing and measurements obtained by monitoring and field data.

In tunnelling, the diameter D of the tunnel is typically small in comparison with its depth C from the ground surface; as such gravitational variation of stress in the soil from crown to invert of the tunnel is not great. Figure 3.4 shows a scheme of the classic centrifuge test performed by Mair (1978). Tunnel excavation was modelled by progressively reducing the pressure in a fluid-filled bag as shown in Figure 3.4. The three-dimensional problem of collapse of a partially unsupported tunnel heading was modelled using a half-cylindrical tunnel with fluid pressure supporting the tunnel face and a length P of unlined cross surfaces. Tunnel heading collapse can be analysed for the two extremes of fully lined and fully unlined tunnels.

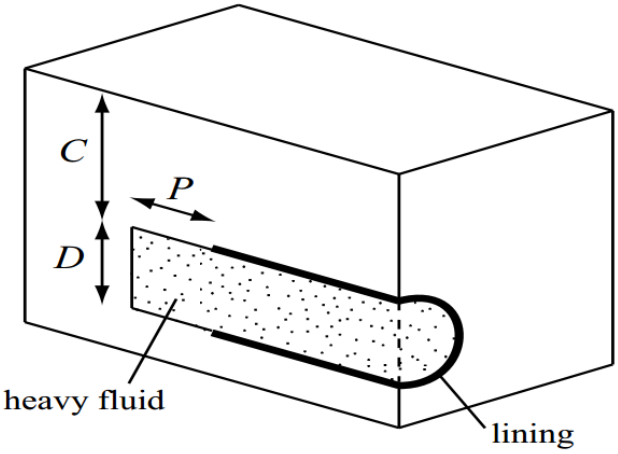

Figure 3.4. Three-dimensional model of partially lined tunnel heading (Mair, 1978).

The fluid pressure is a very approximate replacement of the actual anisotropic in-situ stress state. To have a more realistic modelling of the soil removal and lining installation in centrifuge tests, robotic techniques are now available (Wood, 2003).

3.2.1 Instrumentation

In full-scale geotechnical systems, there are some important quantities, such as pore pressures, contact stresses, displacements, and structural responses, that should be measured during the analyses.

Pore pressures are usually measured by Druck transducers composed of a silicon diaphragm as a differential pressure-sensitive element. Contact stresses, measured by contact stress transducers, are difficult to be estimated reliably at any scale. The differentiation of experimental observations always introduces errors. The use of tactile pressure sensitive mats is described by Springman et al. (2002). These can measure local stresses over a grid of 1936 contact points over an area $56 \times 56\text{mm}$. The sensitivity of this measuring device is not particularly good, and the calibration is not straightforward, but this is a promising emerging technology. Displacements can be measured by LVDTs (linear variable differential transformers) at discrete points of the model. Additionally, non-contact lasers can be used to monitor displacements across surface profiles. These devices are appropriate and practical for recording displacement patterns rather steady state conditions. Figure 3.5 shows the use of several overhead-fixed cameras mounted above the surface of the model to capture and record the actual movement of the ground surface.

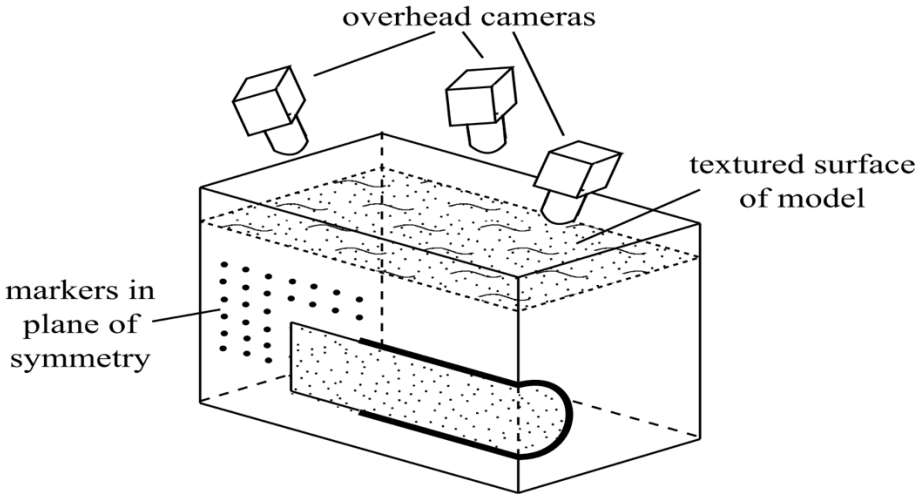

Figure 3.5. Close-range photogrammetry for recording three-dimensional surface displacements (Taylor et al., 1998).

3.3 Experimental case study: centrifuge tests at the University of Nottingham

This section briefly introduces the instruments and techniques for modelling of soil-structure interaction problems in centrifuge tests at University of Nottingham.

3.3.1 Geotechnical centrifuge

The beam centrifuge at University of Nottingham, manufactured by Thomas Broadbent & Sons Ltd, is shown in Figure 3.6. This centrifuge has 2m radius with one swinging cradle and 50g-tonne capability. The centrifuge can operate at 100-g with a payload of 500kg and up to 150-g at a reduced payload of 330kg. The centrifuge package components for the study of tunnelling include the centrifuge strong box, the soil, the model tunnel, and the tunnel volume control system. These components are described in the following sections.

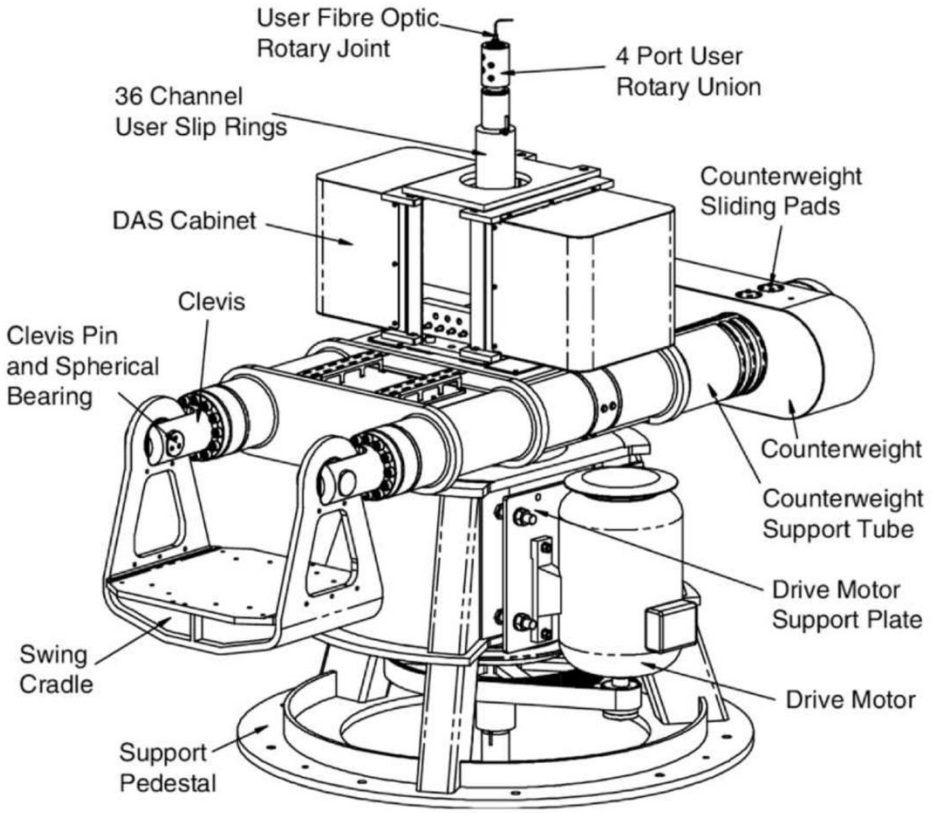

Figure 3.6. Main components of the University of Nottingham geotechnical centrifuge (Ellis et al., 2006).

3.3.1.1 Centrifuge strong box

The centrifuge strong box was designed such that measurements of soil and structure deformations are made using image-based analysis techniques at the plane of symmetry provided by the Perspex wall. The main components of the strong box are a stainless U-channel, a Perspex front wall and a Back-aluminium wall which was shown in Figure 3.7(a) and schematically for the cross-section in Figure 3.7(b). To avoid leakage, the stainless-steel U-channel was bolted to the Perspex window and the aluminium back wall. The plain dimensions at the strong box are $640 \times 260\text{mm}$ and the maximum height of soil within the box is 500mm. The thickness of the front wall was made of 100mm thick Perspex to estimate the ground movements from a series of pictures taken during the test. The internal face of Perspex sheet is curved with a circular hole of 20mm depth. It is important to report that the friction at the soil-Perspex interface reduces ground movement magnitude by 10%-15% without significant impact on the displacement distribution (i.e. the shape of the deformation pattern) (Marshall, 2009).

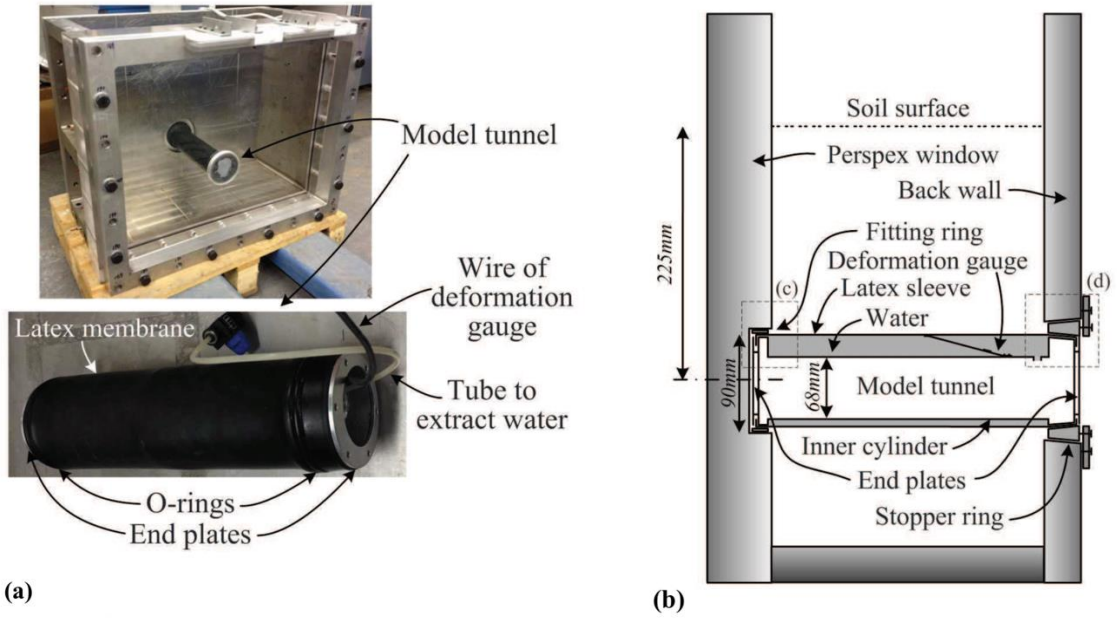

Figure 3.7. The strong box (a) model tunnel; (b) cross-section through model (Franza, 2017).

3.3.1.2 Soil

In the investigated experiments, the box was filled with dry Leighton Buzzard Fraction E silica sand supplied by David Ball Group plc. This sand has a typical average diameter $d_{50} = 0.122\text{mm}$, a specific gravity $G_s = 2.65$ and has the minimum and maximum void ratio, $e_{min} = 0.613$ and $e_{max} = 1.014$, respectively (Corresponding to relative densities vary between 0.3 and 0.9, see Table 3-2).

Table 3-2. The relative density and the density of soil (Franza, 2017).

I_d (%)	ρ_s (kg/m^3)
30	1399
50	1461
70	1529
90	1603

3.3.1.3 Tunnel model

The tunnel model consists of an outside diameter of 90mm (Figure 3.8). The entire tunnel model is sealed within a latex membrane of 1mm thickness. This part is filled with water to achieve the tunnel volume loss by extracting fluid from the annulus using the volume control system, described in section 3.3.1.4.

Figure 3.8. The model tunnel **90mm** diameter and its fitting rings (Franza, 2017).

Despite the different inner shape, the tunnel model uses the water extraction technique for simulation of the tunnel volume loss. In this type of simulation, the movement of the soil depends on the balance that is established between the water and sand, because the tunnel membranes are fully-flexible and the structural lining is not modelled. Extraction of fluid from the tunnel is achieved via a small hole through one of the ends of the tunnel model using a remotely-controlled actuator. The deformation is constant along all the longitudinal direction and, as such, the face advancement cannot be simulated.

The tunnel model consists in a hollow inner cylinder with enlarged ends covered by a latex sleeve sealed with O-rings, grease and end plates. The inner cylinder was designed with a downward eccentric shape to reproduce the typical oval-shaped distribution of ground loss (Figure 3.9(f)).

The diameter of 68mm for inner cylinder provides more than 20% potential volume loss. During the test phases, the water, which is initially at high pressures, is gradually extracted from the system for controlling the volume loss. The maximum hydraulic pressure induced in-flight in the model tunnel was about 350kPa. All components of the tunnel model and the strong box (excluding the latex sleeve) are shown in Figure 3.9. These components are made of

aluminium. The latex membrane at the edges of the enlarged ends may provide a stiffening effect, which could affect the plane-strain condition at the Perspex. To minimize this disturbance, the enlarged ends of the tunnel cylinder were set slightly inside the recess of the Perspex and the back wall (Figure 3.9(a) and (b)).

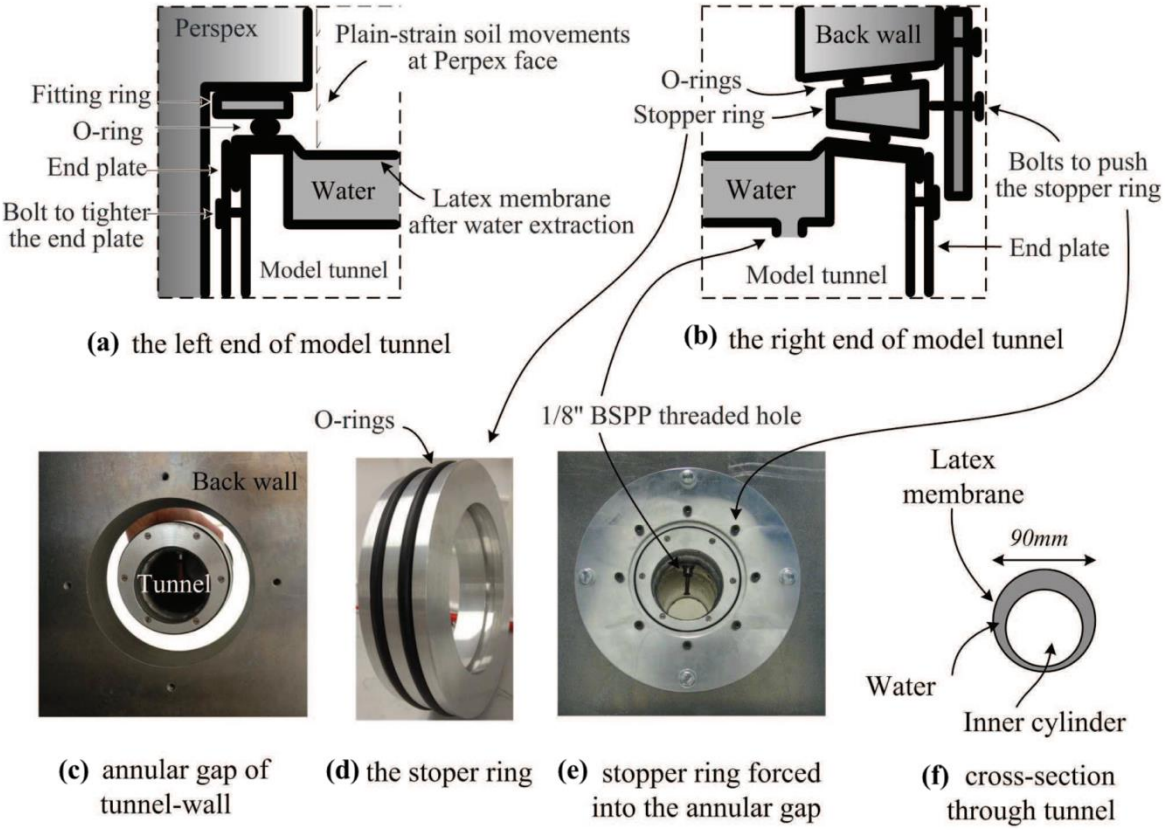

Figure 3.9. The model tunnel components and fitting rings (Franza, 2017).

3.3.1.4 Tunnel volume control system

Figure 3.10 shows the volume loss control system. This system has the possibility to simulate the excavation of the tunnel based on the volume losses by gradually extracting the pressurized water from the latex membrane. This mechanism is composed of the following main parts:

- constant-head standpipe
- pore pressure transducer (PPT)
- solenoid valve
- hydraulic cylinder with attached Linear Variable Differential Transducer (LVDT)
- actuator and pipework connecting the system to the tunnel

The solenoid valve helps to close the connection between the tunnel and stand-pipe during the spin-up to 5g to prevent a drop of the tunnel pressure. Indeed, this component balances the volume loss at the tunnel, during the centrifuge spin-up from 5g to Ng, due to the compressibility of air trapped within the system. Then, the water extraction from the tunnel was achieved by raising the actuator head connected to the hydraulic cylinder system. Finally, the LVDT and PPT are used to measure respectively the relative displacement of the hydraulic piston and the water pressure in the system.

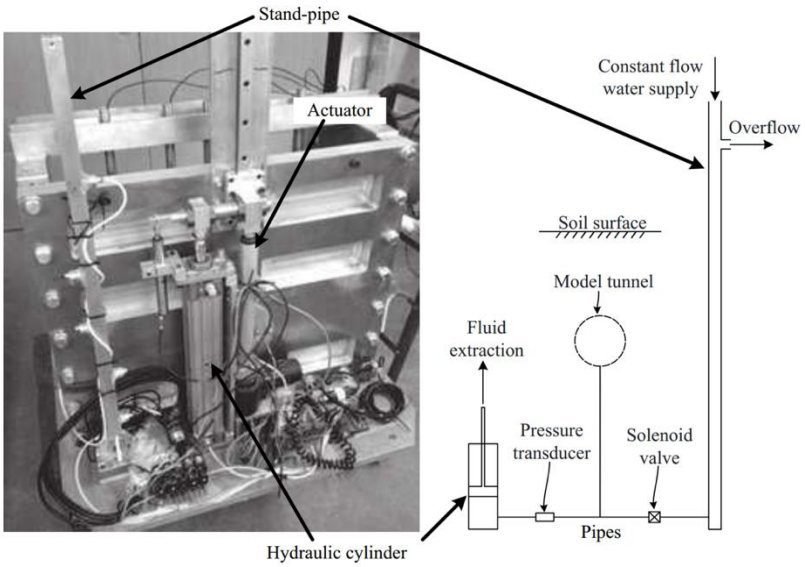

Figure 3.10. Tunnel volume control system: (a) back view of the experimental package, (b) sketch of the volume control system (Franza, 2017).

3.3.2 Digital image analysis

Digital image analysis is utilized to measure a) the surface and subsurface soil displacements and b) tunnelling-induced displacements of soil-structure interaction tests at the Perspex window. The GeoPIV image-based measurement technique is a reliable tool to compare measurements obtained through image analysis with those normally obtained through the LVDTs. In all centrifuge tests, two or three digital cameras located at the front of the centrifuge container to measure both soil and structure displacements during tests. Structure displacements were obtained by tracking white dots painted on the front face of the building models (Figure 3.11). Additionally, during some of the greenfield tests, the system was upgraded with a third camera, positioned on an aluminium support, and used to track soil movements beneath the tunnel invert.

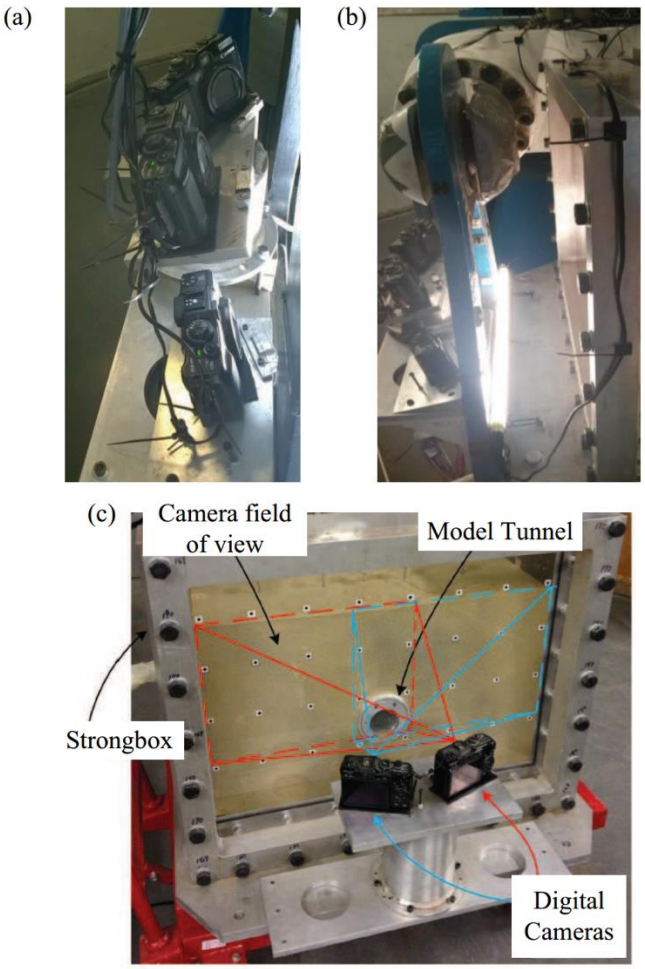

Figure 3.11. (a) Digital camera set-up, (b) cameras, lights and strong box, (c) example of the camera fields of view (Franza, 2017).

3.3.3 Centrifuge experiments on tunnel frame interaction

A large number of framed building models were manufactured for the Nottingham centrifuge tests by machining and welding aluminium plates and angles. An almost rigid connection was achieved between walls and slabs by welding 60% of the length along the longitudinal direction. To model the tunnelling process, the plane-strain experimental package was used. In these tests, the frames extended over almost the full width of the centrifuge box in the direction of the tunnel axis to achieve the plane-strain condition; in fact, the modelled buildings were 258mm long in the tunnel longitudinal direction, producing a 1mm gap at the front and back walls of the 260mm wide centrifuge strongbox. The thickness (t) of the structural elements were the same for foundation, elevated slabs and walls (Xu et al., 2019) with a thickness of 3.2mm. Considering that aluminum and concrete had a similar Young's modulus (which is not

affected by the centrifuge scaling laws), the prototype cross-sectional stiffness of slabs and walls realistically replicated typical reinforced concrete structures.

The considered prototype geometry was: a tunnel with a diameter of 6.1m, and a cover depth of 8.0m, a building transverse width of 30m (Xu et al., 2019). The tunnel diameter used in Nottingham centrifuge was different from that used by Farrell (2011). In order to compare results against Farrell's dataset (2010), the same prototype scenario was considered. For this reason, the acceleration applied to this experiment was chosen at 68g, instead of 75g used by Farrell (2011) to match the prototype scenario.

In centrifuge tests of Nottingham, the building self-weight were varied as standard self-weight (SW) and double self-weight (2SW). The standard self-weight SW was due to the weight of the aluminum used for the frame models (calculated for in-flight conditions considering the variation of gravity level across the height of the models). The double self-weight 2SW was achieved by adding simply supported (at wall locations) weights to the top of the frames; this system ensured that the additional weight did not increase the frame stiffness (see Figure 3.12). Figure 3.12 illustrates a 2-storey building frame with dead weights added on the framed structure.

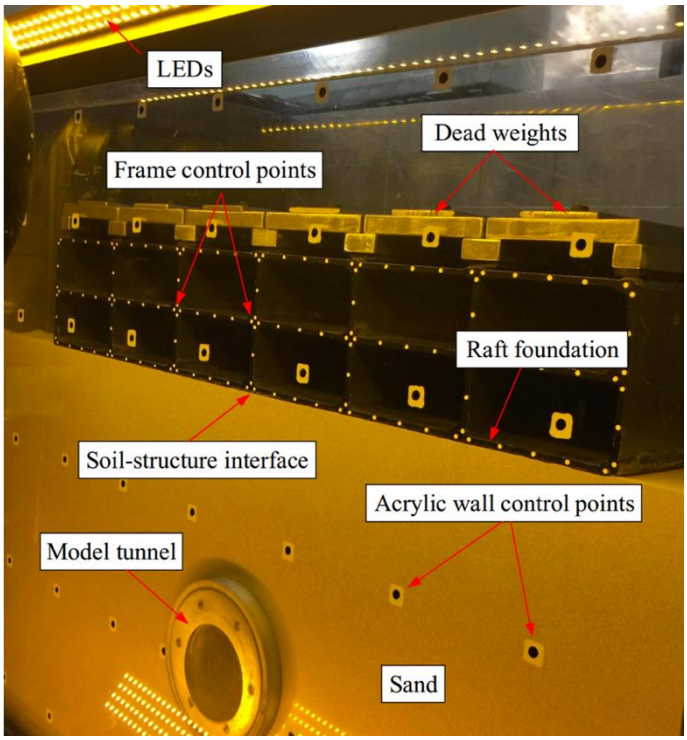

(a)

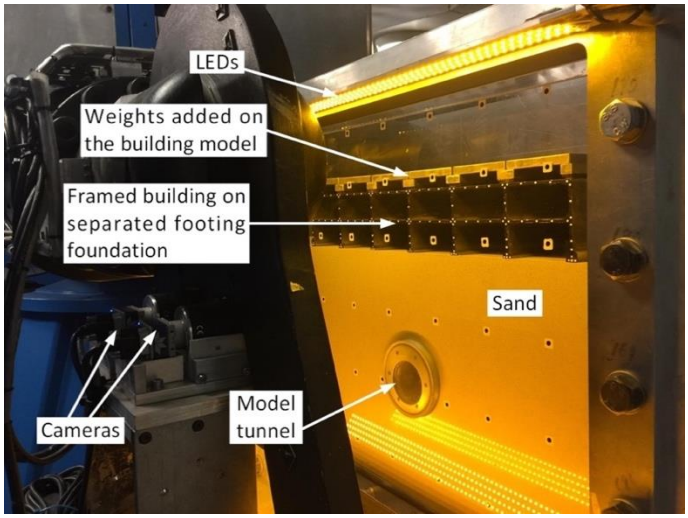

(b)

Figure 3.12. (a) Set up of the centrifuge model (b) position of cameras (Xu et al., 2019).

Chapter. 4. Finite element modelling

The Finite Element Method (FEM) has been used increasingly for the analysis of geotechnical engineering applications. The use of advanced numerical methods, such as the finite element method, allows the users to carry out complex analyses that help to describe soil behaviour and structure, as well as their interaction. When using the finite element method, soil is modelled by means of a constitutive model (stress-strain relationship) which is formulated in a continuum framework. The choice of the constitutive model and the corresponding set of model parameters are the most important issues to consider when creating a finite element model for a geotechnical project.

The finite element method involves the following steps:

- *Element discretisation:*
  This is the process of modelling the geometry of the problem under investigation by an assemblage of small regions, termed *finite elements*. These elements have *nodes* defined on the element boundaries, or within the element.
- *Primary variable approximation:*
  A primary variable must be selected (e.g. displacements, stresses, etc.) and rules as to how it should vary over a finite element established. This variation is expressed in terms of nodal values. In geotechnical engineering it is usual to adopt displacements as the primary variable.
- *Element equations:*
  Use of an appropriate variational principle (e.g. Minimum potential energy) to derive element equations.
- *Global equations:*
  Combine element equations to form global equations.
- *Boundary conditions:*
  Formulate boundary conditions and modify global equations.
- *Solve global equations:*
  The global equations are in the form of a large number of simultaneous equations. These are solved to obtain the displacements at all the nodes. From these nodal displacements, secondary quantities, such as stresses and strains, are evaluated.

Finite element softwares are available for 2D and 3D calculations; however due to its simplicity and reduced computational time, 2D versions are the most popular. In fact, 3D analysis involves considerably more elements, and therefore nodes and integration points, than comparable 2D analysis. In this study, a series of finite element analyses are conducted using PLAXIS 2D and 3D to validate the numerical approach against experimental results in centrifuge tests. In addition, a large number of numerical analyses are carried out to investigate the response of framed structures with masonry infills.

4.1 PLAXIS

PLAXIS program grew out of research conducted at Delft University of technology in the late 1970's on the use of finite element methods for geotechnical designs. In the beginning, there was an initial research project which led to the development of a finite element program that was capable of solving relatively simple deformation problems in plane strain condition. This program was later extended to include a large range of additional features (Burd, 1999).

PLAXIS started with 6-node triangles for finite element discretisation. These elements, when used by De Borst and Vermeer (1984) for the cone pressuremeter problem, gave very poor results because they exhibit 'locking' when used to model incompressible materials. After several researches and studies by Sloan and Randolph (1982), the effects of these incompressibility constraints was reduced by increasing the number of nodes in the element, adopting the 15-node triangle. De Borst and Vermeer (1984) implemented these elements in PLAXIS and were able to obtain much improved solutions to the cone penetrometer problem. In the current version of PLAXIS, the user can select either 6-node or 15-node triangular elements to model the soil layers and other volume elements. Figure 4.1 illustrates the position of nodes and stress points in soil elements for both 6-node and 15-node triangle elements. The main difference between these two types of soil elements is related to this fact that the 15-node triangle provides a fourth order interpolation for displacements and the numerical integration involves twelve Gauss points (stress points), while the 6-node triangle provides a second order interpolation for displacements and the numerical integration involves three Gauss points. The use of 15-node triangle leads to more memory consumption and slower calculation in comparison with 6-node triangle.

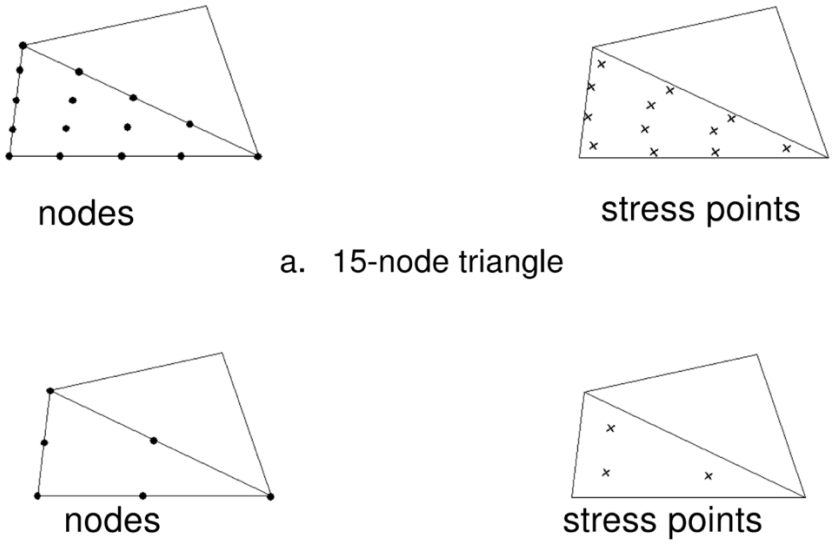

Figure 4.1. Position of nodes and stress points in soil elements for (a) 15-node triangle (b) 6-node triangle (Brinkgreve et al., 2017).

In geotechnical problems, soil and rock tend to have a highly non-linear behaviour under static and dynamic loads. The non-linear stress-strain behaviour can be modelled at several levels of sophistications. In recent years, there are a large number of constitutive models which are developed, with a number of model parameters increasing with the level of sophistication. The application of constitutive models of the elasto-plastic type allows to estimate the collapse conditions of the most common geotechnical problems in a very accurate way. The mesh dependency and establishment of cyclic/dynamic actions resulting from seismic events considerably complicates the analysis of the mechanical behaviour of the model. In such conditions of stress, the detailed knowledge of the mechanical response of the material is of fundamental importance for the creation of accurate predictive constitutive models. Some of the constitutive models are available in PLAXIS are:

- Linear Elastic model
- Mohr-Coulomb model
- Hardening Soil model
- Soft Soil model
- Modified Cam-Clay model
- Hoek-Brown model
- UBC3D-PLM model
- Concrete model

The user-defined soil model (UDSM) is an option that allows the users to implement a new material model.

Comprehensive constitutive models can reliably simulate the complex stress-strain behaviour of sands and these are conceptually simple and computationally efficient in an iterative process. The SANISAND model is a user-defined model developed for simulating the mechanical behaviour of sandy soils. SANISAND is the name used for a family of models (simple ANIsotropic Sand) developed within the frameworks of critical state soil mechanics and bounding surface plasticity (Manzari and Dafalias, 1997; Dafalias and Manzari, 2004). The SANISAND constitutive model can realistically simulate the sand behaviour under conventional monotonic and cyclic loading paths.

4.2 SANIAND constitutive model for sands

The use of representative models helps reducing the epistemic uncertainty in the analyses. The uncertainty reduction depends on the calibration of the model parameters. SANISAND model parameters are studied in detail to have a better understanding for an accurate calibration of experimental tests.

The critical state soil mechanics (CSSM) is a general theoretical framework for explaining the stress-strain behaviour of soils. The original studies for applying the elasto-plasticity theory within the framework of CSSM are due to Roscoe et al. (1963) and Roscoe and Burland (1968). These theories were not sufficiently complete for the description of the cyclic behaviour of soils, including the pore-water pressure development under cyclic undrained loading conditions. The framework was further developed by introducing the kinetic hardening, multi-surface plasticity and bounding surface plasticity models to simulate the cyclic loading conditions in addition to monotonic loadings. Finally, Manzari and Dafalias (1997) developed a comprehensive constitutive model for sands to solve the disadvantages of the previous models. There are two new concepts which are used: (1) the concept of a yield/bounding or two-surface plasticity formulation, and (2) the concept of the state parameter, an essential variable in a CSSM framework. The modifications on these two independent concepts were applied for the peak stress ratio and state parameter proposed by Wood and Belkheir (1994).

4.2.1 Basic concepts

A brief overview of the basic formulation of SANISAND will be presented in triaxial space for the sake of simplicity, even if the model is fully compatible with a multiaxial stress-space generalization. Triaxial stress and strain components are defined as deviatoric stress $q = (\sigma_1 - \sigma_3)$, mean pressure $p = (\sigma_1 + 2\sigma_3)\,(1/3)$, deviatoric strain $\varepsilon_q = (\varepsilon_1 - \varepsilon_3)\,(2/3)$, and volumetric strain $\varepsilon_V = (\varepsilon_1 + 2\varepsilon_3)$. The stress ratio is represented by $\eta = q/p$.

The drained and undrained triaxial tests are used to highlight the main features of the model by considering dense or loose specimens of sand. The critical state, at which deformation continues for fixed stresses and zero volumetric strain rate, is attained when the stress ratio $\eta = q/p$ equals M_c (the critical value in triaxial compression), and simultaneously the void ratio e equals e_c (the critical void ratio), which is assumed to be a unique function of p. The critical state line (CSL) is defined as the relation between e and $\ln p$ with slope λ , as shown in Figure 4.2.

A typical material response is illustrated in Figure 4.2 and Figure 4.3. In drained constant-p triaxial compression, the soil behaviour shows first consolidation by moving to point a'_d, and then dilation until it reaches point a'_c on the CSL, where $e = e_c$ and critical state is attained. Simultaneously, Figure 4.2 shows that the point a moves upward, crosses point a'_d, where consolidation changes to dilation at a stress ratio $\eta = M_c^d$, and then falls back at the critical stress ratio with $\eta = M_c$. In undrained loading, point a will first move to point a''_d, as positive pore water pressure development due to the initial contractive tendency reduces the effective stress p, and then upon dilative tendency will move to the critical point a''_c at the same e as the initial value, where failure occurs (Manzari and Dafalias, 1997).

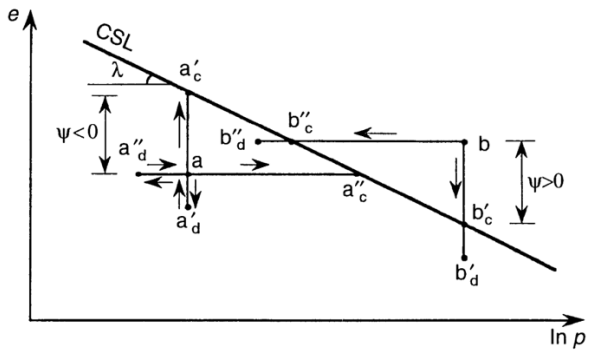

Figure 4.2. Schematic illustration of drained and undrained paths in critical state line (Manzari and Dafalias, 1997).

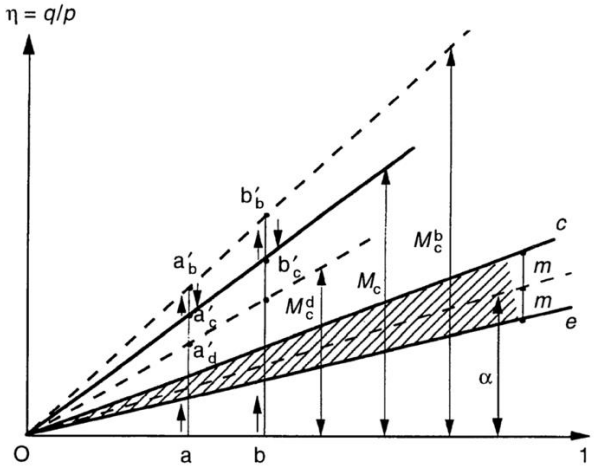

Figure 4.3. Schematic illustration in the $\boldsymbol{\eta}$, **1** space of the bounding (peak) stress ratio, critical stress ratio and dilatancy stress ratio (Manzari and Dafalias, 1997).

A constitutive model is required to simulate the response under cyclic loading if it is to be used in problems involving such loading (e.g. earthquake induced loading). In addition, a unique set of model constants for all densities and confining pressures is needed as well as a formulation for a general stress space.

4.2.2 Elastic and plastic strains

The nonlinear elastic response of the SANISAND model is assumed to be hypoelastic. The strain increment is decomposed to elastic and plastic parts, denoted by the superscript e and p, each one having deviatoric and volumetric parts, denoted by subscripts q and v:

Eq. 4.1 $$d\varepsilon_q^e = \frac{dq}{3G}, \qquad d\varepsilon_v^e = \frac{dq}{K}$$

Eq. 4.2 $$d\varepsilon_q^p = \frac{d\eta}{H}, \qquad d\varepsilon_v^p = d\left|d\varepsilon_q^p\right|$$

where K and G are the hypoelastic bulk and shear moduli, H is the plastic hardening modulus associated with the increment of stress ratio $d\eta$, and d is the dilatancy coefficient. Variables H and d will be defined later. The shear modulus is defined according to Richard et al. (1970) and Li and Dafalias (2000):

Eq. 4.3 $$G = G_0 p_{atm} \frac{(2.97-e)^2}{1+e} \left(\frac{p}{p_{atm}}\right)^{1/2}$$

where G_0 is a dimensionless material constant, ν is the Poisson's ratio, e is the void ratio, and p_{atm} is the atmospheric pressure used for normalization.

4.2.3 Critical state

SANISAND is formulated within the critical state soil mechanics framework. The location of the critical state line that defines the critical void ratio e_c is given by the power relation after Li and Wang (1998):

Eq. 4.4 $$e_c = e_{c0} - \lambda_c(\frac{p_c}{p_{atm}})^{\xi}$$

where e_{c0} is the void ratio at $p_c = 0$, λ_c and ξ are dimensionless material constants. The model uses the concept of the state parameter ψ proposed by Been and Jefferies (1985) to define the distance between the current void ratio and the critical void ratio:

Eq. 4.5 $$\psi = e - e_c$$

4.2.4 Yield surface

The yield surface can be imagined as a tiny wedge in the $p - q$ space and a cone in the multiaxial space. It is expressed by:

Eq. 4.6 $$f = |\eta - \alpha| - m$$

where the m is a material constant representing the opening of the yield surface and α is the deviatoric back stress ratio representing the orientation of the yield surface.

4.2.5 Dilatancy, bounding and critical surfaces

The model uses three concentric and homologous surfaces: the dilatancy, bounding and critical surfaces. These are considered in the π-plane. The dilatancy surface enables the model to reproduce contractive volumetric soil response if $\eta < M^d$, and dilative volumetric soil response for $\eta > M^d$. The evolution of the dilatant surface is defined by the state parameter ψ as:

Eq. 4.7 $$M^d = M \exp(n^d \psi)$$

where M and n^d are positive material constants. The bounding surface is defined by the slope of M^d. This surface enables the model to reproduce softening if $\eta > M^b$, this will result in a peak shear stress in the stress-strain curve. The evolution of the bounding surface is again defined by the state parameter ψ as:

Eq. 4.8 $$M^b = M \exp(-n^b \psi)$$

where n^b is positive material constant. As the sample reaches the critical state, and the distance between the critical void ratio and the current void ratio is close to 0, the lines representing $M^d$and M^b converge and collapse with the critical surface line M.

4.2.6 Plastic flow

The used SANISAND model includes a non-associative flow rule allowing realistic evaluations of plastic strain increments with Eq. 4.2. In this equation H controls the increment of the plastic deviatoric strain as a function of distance between $M^b$and η:

Eq. 4.9 $$H = h\,(M^b - \eta)$$

where h is a function of current state variables p and e. The dilatancy coefficient d in Eq. 4.2 is expressed through:

Eq. 4.10 $$d = A_d\,(M^d - \eta)$$

where A_d is a function of the fabric dilatancy.

4.3 Implementation of SANISAND model in PLAXIS

SANISAND model can reproduce the main features of real sand behaviour, such as: 1) the peak of deviatoric stress for dense sands in drained conditions or for loose sands in undrained tests, 2) the continuous evolution of dilatancy until eventually reaching constant volume conditions, and 3) the evidence of a small elastic region entailing initially large stiffness when load reversal occurs.

SANISAND constitutive model was programmed by Dr. Hong Yi of Zheijang University. This user-defined model was then implemented in PLAXIS and ABAQUS finite element softwares. The programming was based on a freely distributed version of $umat$ developed by Martinelli et al. (2015) available at the soilmodels.info website. This SANISAND model includes 19 parameters which are specified in the following order (Martinelli et al., 2015).

- **parameter 1 - p_a:** atmospheric pressure
- **parameter 2 - e_0:** void ratio on critical state line at $p = 0$
- **parameter 3 – λ:** CSL parameter ($e - q$ plane)
- **parameter 4 - ξ:** CSL parameter ($e - q$ plane)

- **parameter 5 - M_c or φ_c:** slope of CSL in $p-q$ plane, TX compression (in Dafalias and Manzari (2004), parameters is denoted as M). It is also possible to set critical state friction angle $\varphi_c$in triaxial compression.
- **parameter 6 - M_e or φ_e or 0:** slope of CSL in $p-q$ plane, TX extension (in Dafalias and Manzari (2004), parameter c is used insted with $c = M_e/M_c$). It is also possible to set critical friction angle φ_e in triaxial extension. It is also possible to set this parameter to 0, then $\varphi_e = \varphi_c$ is implied.
- **parameter 7 - m:** opening of yield surface cone
- **parameter 8 - G_0:** shear modulus constant
- **parameter 9 – ν:** Poisson's ratio
- **parameter 10 - h_0:** plastic modulus constant
- **parameter 11 - c_h:** plastic modulus constant
- **parameter 12 - n^b:** plastic modulus constant
- **parameter 13 - A_0:** dilatancy constant
- **parameter 14 - n_d:** dilatancy constant
- **parameter 15 - z_{max}:** fabric index constant
- **parameter 16 - c_z:** fabric index constant
- **parameter 17 - K_w:** pore water bulk modulus (undrained conditions). For drained or consolidation analysis, $K_w=0$.
- **parameter 18 - p_{tmult}:** shift of mean stress calculated as $p_t=p_{tmult} * p_a$. Can be used to stabilise the simulation where free surface or zero stresses occur.
- **parameter 19 - e:** initial value of void ratio (a state parameter that can change during the simulation).

The critical state parameters 2, 3, 4 and 5, the constants parameters 12 and 14 (which respectively relate the position of the bounding and dilatancy surfaces to the critical surface as a function of ψ), and the parameter 6 (which is the ratio c between the slopes of the CSL in extension and in compression) can all be obtained through conventional triaxial compression and extension tests. The elastic parameters can be obtained from measurements of $G_0$and ν at small strains. The hardening parameters 10 and 11 and the parameters 13, 15, and 16, governing the evolution of dilatancy, need to be found through a trial and error procedure. In addition, parameters 15 and 16, which were introduced in the model to improve predictions under cyclic

loads, are in the present work set to zero, at the load path is essentially monotonic for the problem at hand (Giardina et al., 2010).

4.4 Mechanical behaviour of Leighton Buzzard Sand

The Leighton Buzzard Sand (denoted as LBS in the following) Fraction E, used in the centrifuge tests of Nottingham, is a commercial sand. The information on the adopted material is investigated based on the results of a series of triaxial and torsional shear tests on dry and saturated sand specimens at the Soil Dynamic lab. of the University of Naples Federico II (Visone and Santucci De Magistris, 2009).

4.4.1 Physical properties of the sand

According to the British Standard, the 100/170 sand passes through the No. 100 British Standard Sieve (0.15mm) and is retained on the No. 170 sieve (0.09mm), being in the category of fine sands. The nominal grain size, which is the average of the maximum and minimum grain size, is equal to 0.12mm. The particle size distribution was determined using the dry sieve method (Figure 4.4).

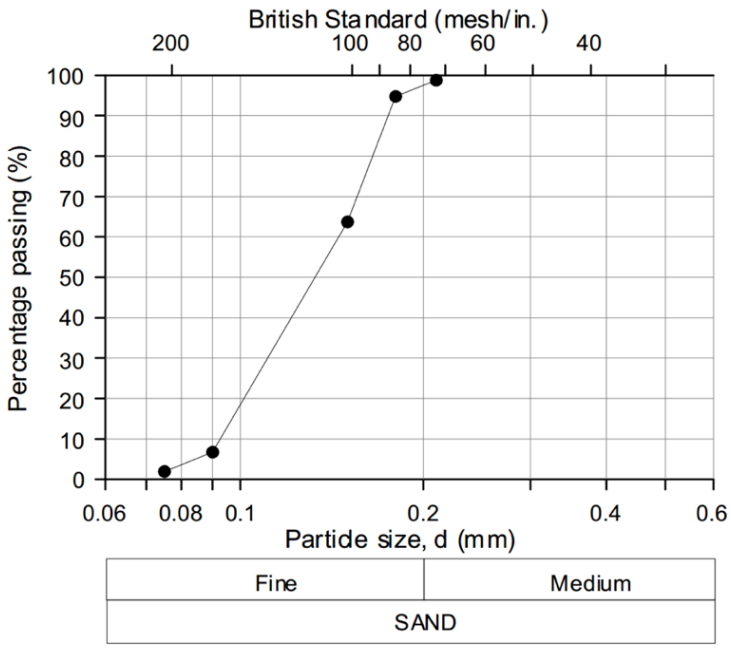

Figure 4.4. Particle size distribution for Leighton Buzzard sand 100/170 (Visone and Santucci De Magistris, 2009).

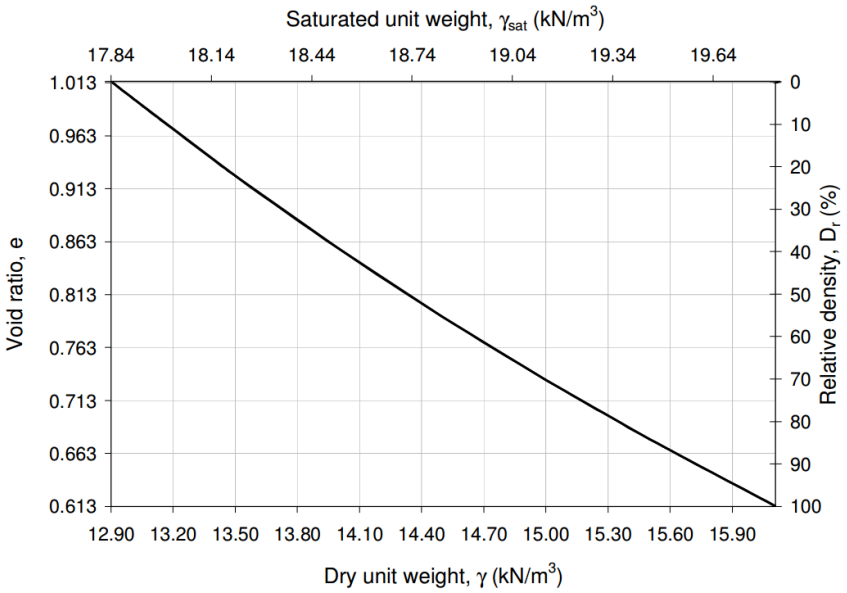

Figure 4.5. Unit weight of LBS for different densities of dry and saturated conditions (Visone and Santucci De Magistris, 2009).

The soil is classified as a uniform sand. Specific gravity G_s for the material is 2.65. The minimum void ratio $e_{min} = 0.613$ and the maximum void ratio $e_{max} = 1.014$ (Visone and Santucci De Magistris, 2009). Figure 4.5 shows the gravimetric properties of the sand for different densities of dry condition.

4.4.2 Experimental program

The mechanical properties of sand, as stiffness and strength, were examined under a series of triaxial and torsional shear tests. Four undrained triaxial compressions (UTC) and extensions (UTE) tests were conducted. Moreover, to evaluate the strength characteristics at peak conditions, drained triaxial tests (DTC and DTE) were performed. DTC100 and DTC200 were drained triaxial tests that the lateral stresses applied to specimens were equal to 100kPa and 200kPa, respectively. Additionally, resonant column and cyclic torsional shear tests were carried out to measure the stiffness and the damping parameters for low and medium strain levels.

In this study, some PLAXIS analyses are modelled to understand the accuracy of the SANISAND constitutive model in reproducing the experimental evidence. Material constants related to Leighton Buzzard sand fraction E calibrated by Giardina et al. (2010) were adopted. They were calibrated based on conventional drained triaxial tests or constant lateral stress tests.

It must be noted that calibration of the parameters related to the CSL was subjected to a certain degree of arbitrariness, as no evidence of critical state behaviour at large strains was observed in any of the laboratory tests (Giardina et al., 2010). As shown in Figure 4.6 (a and b), there is a good agreement between the numerical results of PLAXIS and the experimental results.

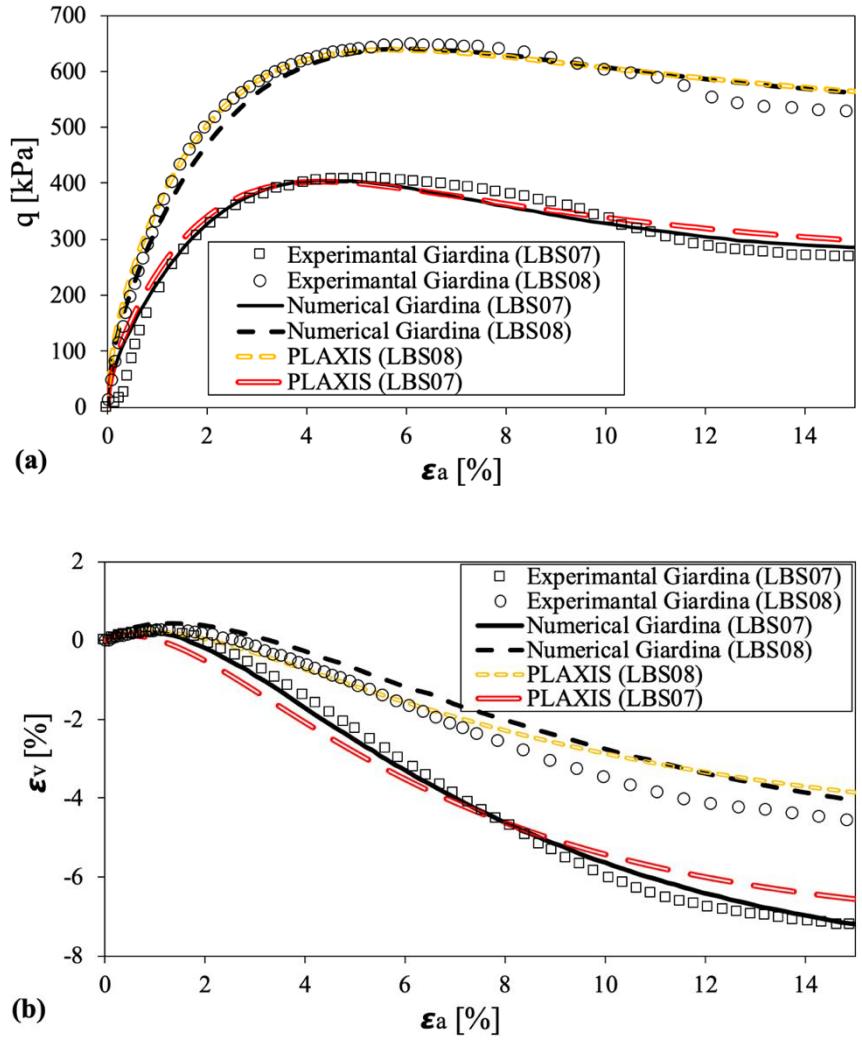

Figure 4.6. Accuracy of PLAXIS analysis for SANISAND model on numerical and experimental results of Giardina et al. (2010).

Table 4-1. Material constants: SANISAND constitutive model (Giardina et al., 2010).

Parameter	Symbol	Value
Critical state line	e_0, λ, ε	0.8191, 0.00178, 2.4352
Elastic law	G_0, ν	600, 0.3

Yield surface	m	0.001
Hardening rule	M, c, n^b, h_0, c_h	1.287, 0.78, 2.8, 0.64, 1.1
Flow rule	n_d, A_0, c_z, z_{max}	2.564, 1.1, 0, 0

4.5 Calibration of parameters for SANISAND constitutive law

Xu et al. (2019) suggested a slight modification in some values of SANISAND parameters summarised in Table 4.1. to better predict the centrifuge test results in greenfield conditions (Table 4-2). As a first approximation for SANISAND parameters, it was possible to observe from the results of the experimental tests (DTC100 and DTC200) but the use of the parameters in table Table 4-1 is not representative of the static response of the soil. For this reason, for the calibration of the model, it was decided to rely on the centrifuge tests conducted by Farrell (2010) at the University of Cambridge. The composition and test methods are similar to the centrifuge tests of the University of Nottingham, the main topic of this paper. The numerical simulations were performed under greenfield conditions, using the Abaqus finite element calculation code to find the final SANISAND parameters in Table 4-2. The comparison with the measurements was obtained in terms of surface settlements generated by the tunnel excavation (Xu et al., 2019).

Table 4-2. Material constants: SANISAND model for the LBS Fraction E (Xu et al., 2019).

Parameter	Value
Elasticity	G_0=400, ν =0.05
Critical state	M =1.287, c =0.78 e_0=0.8191, λ =0.00178, ε =2.4352
Yield surface	m =0.01
Plastic modulus	n^b=2.8, h_0=4.05, c_h=1.1
Dilatancy	n_d=2.564, A_0=0.55
Fabric-dilatancy tensor	z_{max}=0, c_z=0

To investigate the peak strength of the sand, Visone and Santucci De Magistris (2009) performed some drained triaxial compression tests (DTC), as we discussed in the experimental section of LBS, by using Bishop & Wesley-type stress path triaxial cell or B&W apparatus (Bishop and Wesley, 1975). DTC100 and DTC200 were carried out in laboratory for initial relative densities of 80.7% and 70.2%, respectively. The dense specimens were prepared with the freezing technique. In these two tests, the drained shear phases were conducted by increasing the axial stress after the isotropic compressions. The two drained triaxial tests DTC100 and DTC200 were simulated in PLAXIS by considering SANISAND model parameters listed in Table 4-2. For both models, the initial void ratio $e_{in} = 0.68$ is considered. Figure 4.7 and Figure 4.8 show the comparison between the experimental and numerical results for DTC100 and DTC200 tests in $q - \varepsilon_a$ and $\varepsilon_v - \varepsilon_a$ planes. The results of $q - \varepsilon_a$ plane show that the numerical analyses in PLAXIS reached an overestimation at the peak resistance in small strains and then they behave a permanent response to coincide with the experimental results.

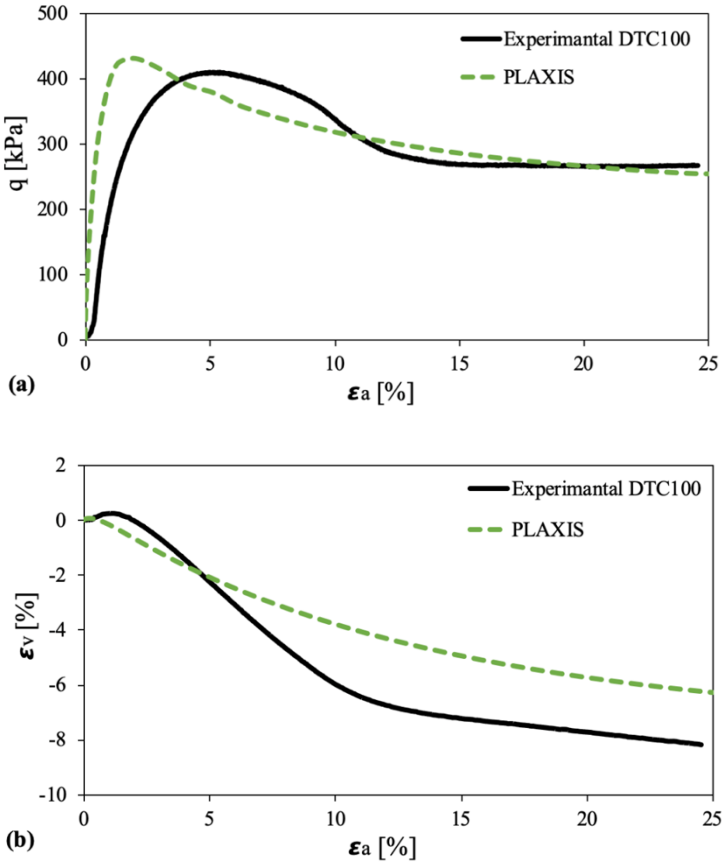

Figure 4.7. Calibration of SANISAND model: Drained Triaxial Compressive test with constant lateral stress $p = 100$kPa.

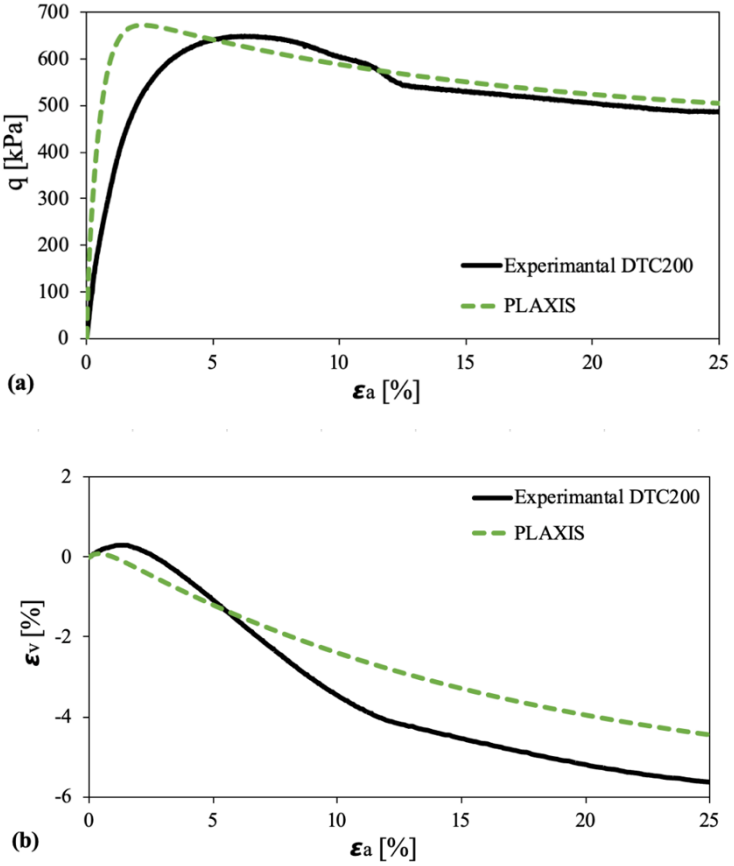

Figure 4.8. Calibration of SANISAND model: Drained Triaxial Compressive test with constant lateral stress $p = 200$kPa.

Chapter. 5. Numerical modelling of tunnel-bare frame interaction

In recent years, several numerical methods have been used to investigate the tunnel-soil-structure interaction. A large number of analyses were performed using an equivalent solid model for the buildings (Pickhaver et al., 2010; Farrell et al., 2014; Losacco et al., 2016); however, refined simulation of the problem were also carried out using detailed structural elements (Giardina et al., 2010; Amorosi et al., 2012; Fargnoli et al., 2015; Boldini et al., 2016; Franza, 2017; Boldini et al., 2018). Although the effect of tunnel excavation on masonry buildings has been studied extensively (Burd et al., 2000; Pickhaver et al., 2010; Yiu et al., 2017), the response of framed buildings has received limited attention so far (Fargnoli et al., 2015; Boldini et al., 2018). In particular, the effect of structural details (e.g., building position, presence of masonry infills, openings, building dimensions) on this soil-structure interaction problem requires further research.

This study investigates the response of framed structures to tunnel excavation with the Finite Element model and explores the influence of both stiff and flexible infill walls, which can play an important role on evaluation of risk assessment. PLAXIS software is used to simulate both 2D and 3D building conditions. In this chapter, firstly 2D Finite Element models of bare frames founded on raft foundation are initially validated against available centrifuge tests performed at the Nottingham University (Xu et al., 2019). Then, 3D numerical analyses of the tests are also presented and discussed to provide further insights into the problem.

5.1 Geometry and problem dimensions

The numerical simulations were inspired by a set of centrifuge tests performed at the Nottingham University (Xu et al., 2019; Xu et al., 2020) and were set up using a commercial software PLAXIS. In particular, the test named F2t3b6L was studied numerically. In 2D modelling, a full size of the domain was modelled while in 3D modellingtaking advantage of the plane-strain conditions of the problem for the cases used to validate. Also, only one half of the domain was simulatedsince the frame was centred in test F2t3b6L. As mentioned before, at the prototype scale, a tunnel of 6.12m diameter and 11m axis depth (thus reperesenting a rather shallow tunnel) was constructed in a fine dry silica sand, known as Leighton Buzzard Fraction E. The excavation was simulated in centrifuge testing by incrementally decreasing the pressure inside the membrane in order to obtain certain volume losses in the tunnel.

Considering the acceleration applied in the centrifuge test equal to 68g, the case F2t3b6L (Figure 5.1) is characterised by the following dimensions at the prototype scale: frame width B = 31.3m and height H = 5.4m, bay length b_{bay} = 5.2m and height h_{bay} = 2.6m, thickness of the structural elements (raft foundation, plates and walls) t = 0.22m. The soil volume is 630mm wide, 322m deep and 260mm thick in the longitudinal direction (corresponding respectively to 43.5m, 21.9m and 17.7m at the prototype scale). For practical reasons, a very small gap exists between the front/back walls of the centrifuge box and the frame; however, plain strain conditions can be practically assumed to be valid for the structure as well.

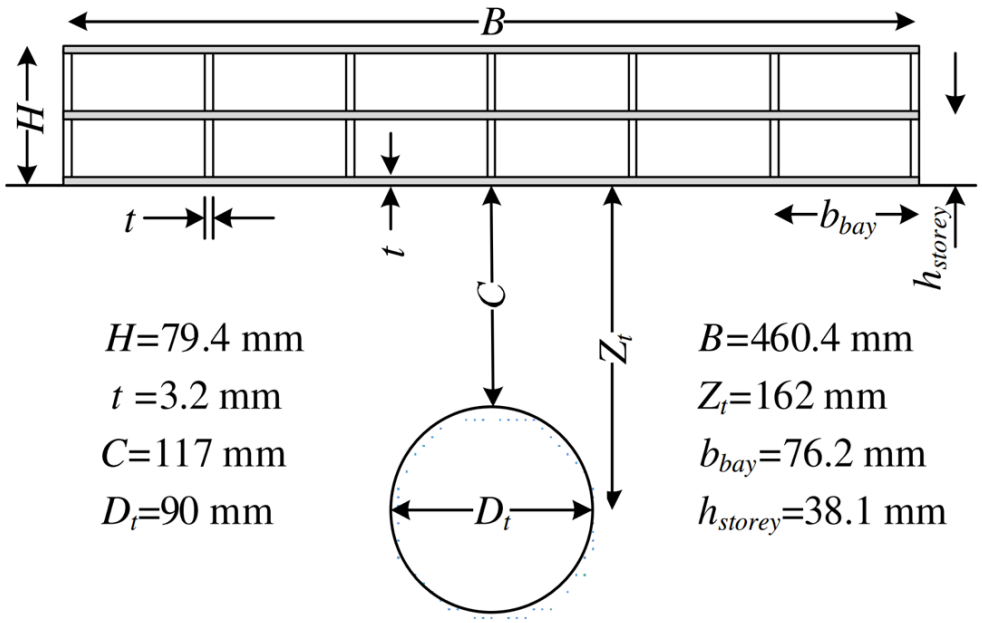

Figure 5.1. Layout of the F2t3b6L centrifuge test considered as a reference for the numerical analyses (Xu et al., 2019).

5.2 Material properties

In this study, the soil behaviour was numerically simulated adopting the SANISAND constitutive model proposed by Dafalias and Manzari (2004), capable of reproducing the influence of the stress state on the initial stiffness and its degradation during tunnelling induced strains. The initial relative density of the Leighton Buzzard Sand was 90% in the considered centrifuge test. A summary of the adopted material parameters is provided in Table 4.2. This constitutive model is implemented in PLAXIS as a user-defined model in DLL file. Table 5.1 shows a view of the SANISAND parameters as displayed in the PLAXIS 2D and 3D

simulations. The general parameters used for the soil elements include $\gamma = 15.60\,\mathrm{kN/m^3}$, $D_r = 0.88$, and $e = 0.68$.

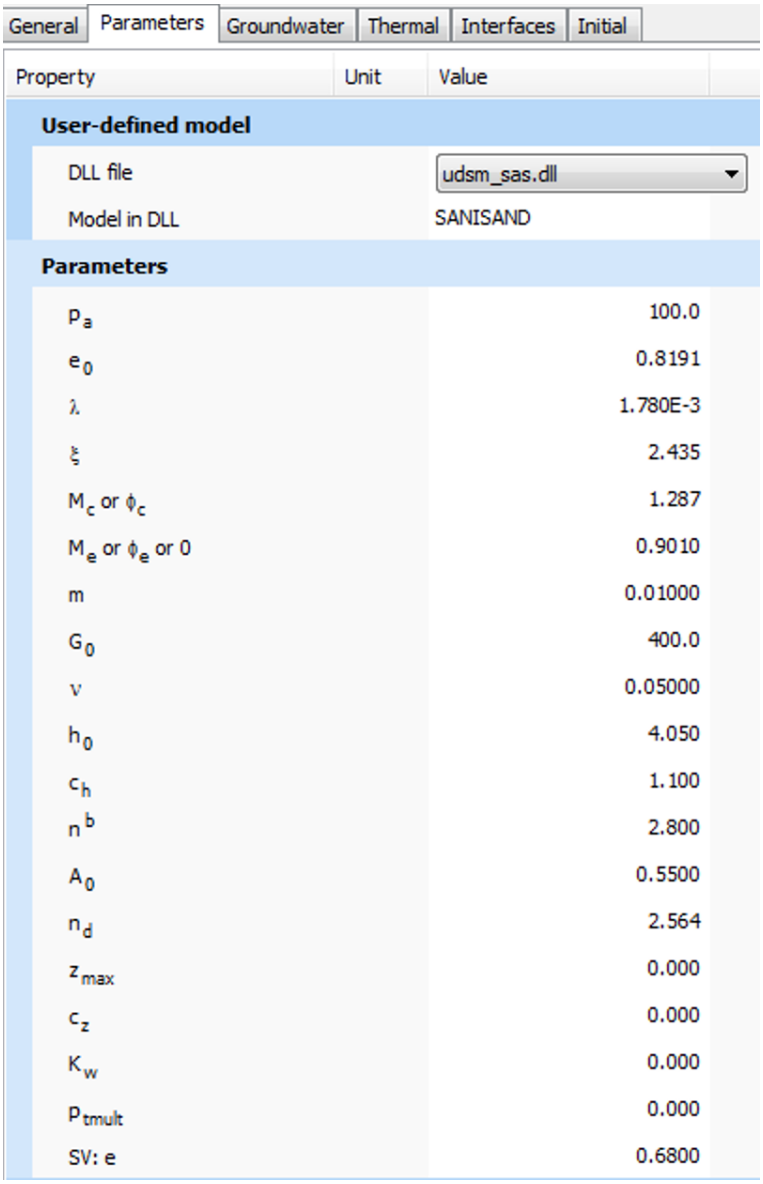

Figure 5.2. Parameters of SANISAND model in PLAXIS 2D and 3D.

5.3 Performed analyses in PLAXIS 2D

Two different numerical analyses were performed to validate the numerical approach against experimental results in centrifuge tests. The first analysis is named “Greenfield” and was executed to simulate the soil behaviour during tunnelling excavation without considering the existence of the frame. The second analysis, named “Frame”, was instead carried out to evaluate soil deformations and building movements, thus including the bare frame.

The numerical analyses in PLAXIS 2D included the following stages: 1) gravity activation in the soil domain, assuming a coefficient of earth pressure at rest $K_0 = 1 - \sin\varphi = 0.5$; 2) activation of the frame and the soil-structure interface elements; 3) deactivation of soil elements inside the tunnel and application of incremental displacements at the boundary nodes. At the latter stage, modelling of tunnel excavation was obtained by applying a displacement boundary condition at the tunnel periphery.

The influence of node numbers wa preliminary assessed by considering 20, 38, 40, and 60 nodes. A number of 38 nodes, equally spaced along the tunnel perimeter, was finally chosen as an optimum number of nodal displacements. In PLAXIS, the prescribed-displacements in horizontal and vertical directions (U_x and U_y) were applied to 38 nodes on tunnel perimeter, fixing the tunnel invert arch (Boldini et al., 2018). Figure 5.3 shows a schematic view of the tunnel contraction before and after applying the prescribed displacements at the tunnel cross-section. In this study, three values of tunnel volume loss are used, namely $V_{l,t}$=0.4%, 1.0% and 2.0%. A tunnel volume loss of $V_{l,t} = 0.4\%$, represents a good tunnelling performance, typically achieved by the use of earth pressure balance (EPB) or slurry shield machines, while $V_{l,t} =$ 1.0% and 2.0% are more typical associated to traditional tunnel excavations.

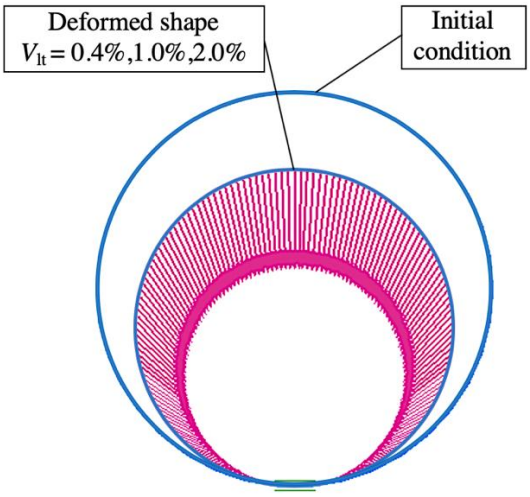

Figure 5.3. Schematic view of prescribed-displacements applied on cross-section area of the tunnel.

5.3.1 Greenfield

The general layout and the generated mesh for simulation of "Greenfield" conditions are shown in Figure 5.4. A full-size model is used to model the soil domain, which extends 43.52m and

21.9m in the directions x and y, respectively. The 15-node triangular elements are selected to model the soil layers. The mesh in Figure 5.4(a) is characterised by 744 elements and 6041 nodes. Nodes at the bottom of the mesh were constrained in all directions, while those along lateral faces were restrained for normal displacements. Figure 5.4(a and b) shows the configuration of the model for the initial phase and for the last stage corresponding to the application of the displacement field (spcify here the tunnel volume loss). The resulting contour of total displacement is shown in Figure 5.5. A comparison between the experimental and numerical results is investigated in section 5.3.3.

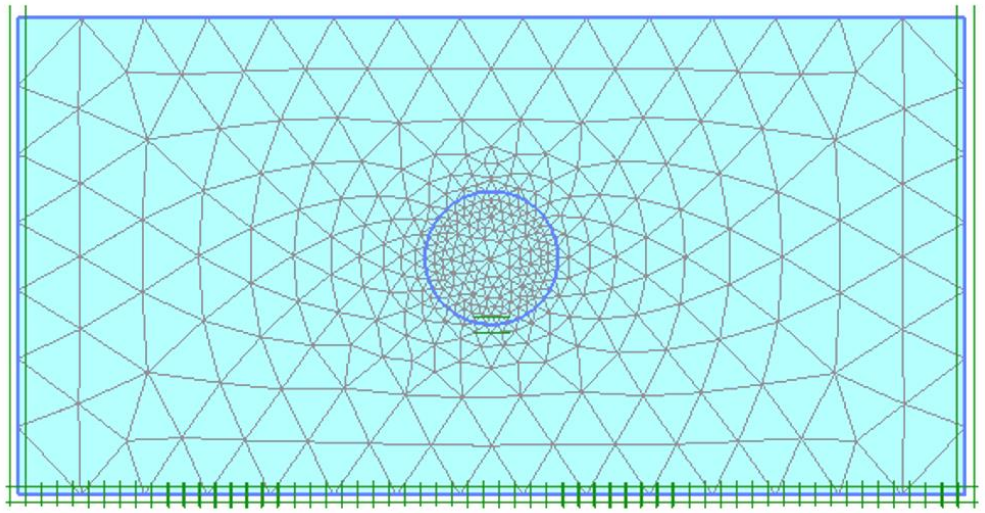

(a)

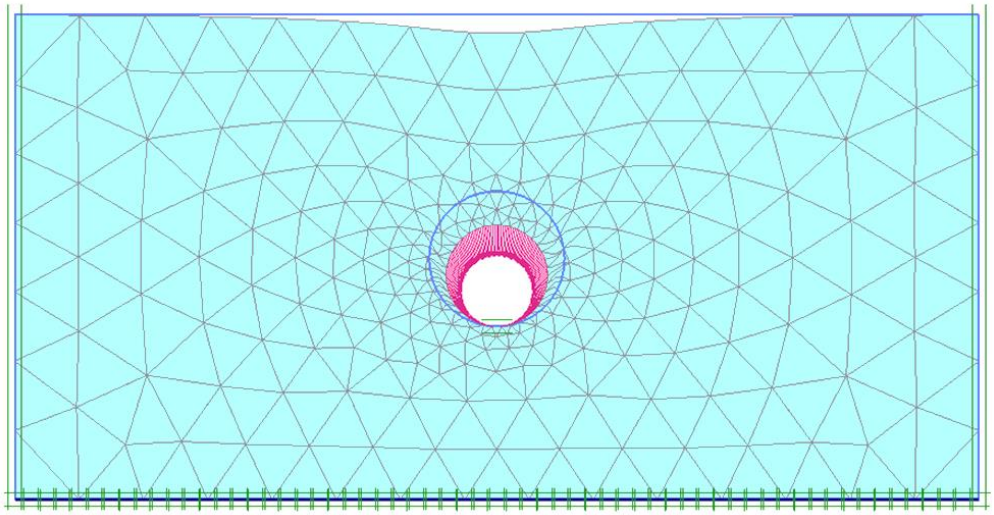

(b)

Figure 5.4. Image of the soil mesh adopted for "Greenfield" model in PLAXIS 2D a) before tunnelling b) after tunnelling ($\boldsymbol{V_{l,t} = 1.0\%}$).

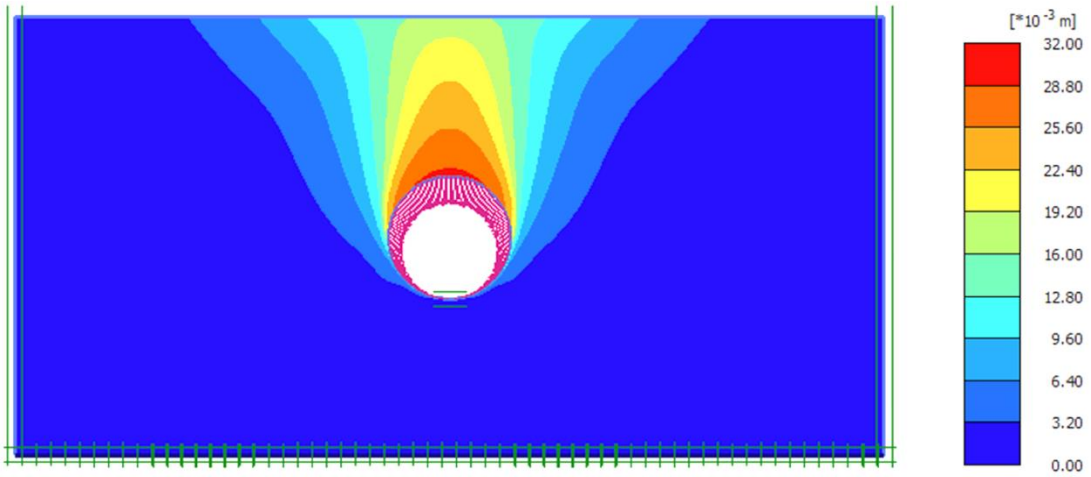

Figure 5.5. Contour of total displacements for "Greenfield" model ($\boldsymbol{V_{l,t} = 1.0\%}$) in PLAXIS 2D.

5.3.2 Frame structure

In experimental tests, the structural elements were assembled by welding two aluminum alloy plates and 12 angle sections. As mentioned before, a quasi-rigid connection was achieved by welding 60% of the length along the longitudinal direction. For the simulation of frames, a linear-elastic and isotropic material was considered for all structural elements. The parameters adopted for the structural elements include a Young's modulus $E = 53.8$ GPa, a Poisson's ratio $\nu = 0.334$ and the unit weight of the material is equal to $\gamma = 27\,\mathrm{kN/m^3}$. Note that in the model, the adopted Young's modulus of the structure is lower than that typically used in aluminum to capture the presence of welds in the beam-pillar connection nodes. In centrifuge testing, to replicate a rough soil-structure interface, a thin layer of sand was glued beneath the structure in the test. In numerical analyses, a friction angle of 32° (the constant volume friction angle of the Fraction E) was used for the interface with a null tensile strength.

The analyses to simulate the "Frame" models have an addtional phase than the analyses for the "Greenfield" models, for the activation of the frame and the soil-structure elements.

Figure 5.6(a) illustrates the mesh generation of "Frame" model with 4973 elements and 42137 nodes. The deformation of the mesh at the end of the calculation is shown in Figure 5.6(b). The total displacement contour for "Frame" model is plotted in Figure 5.7.

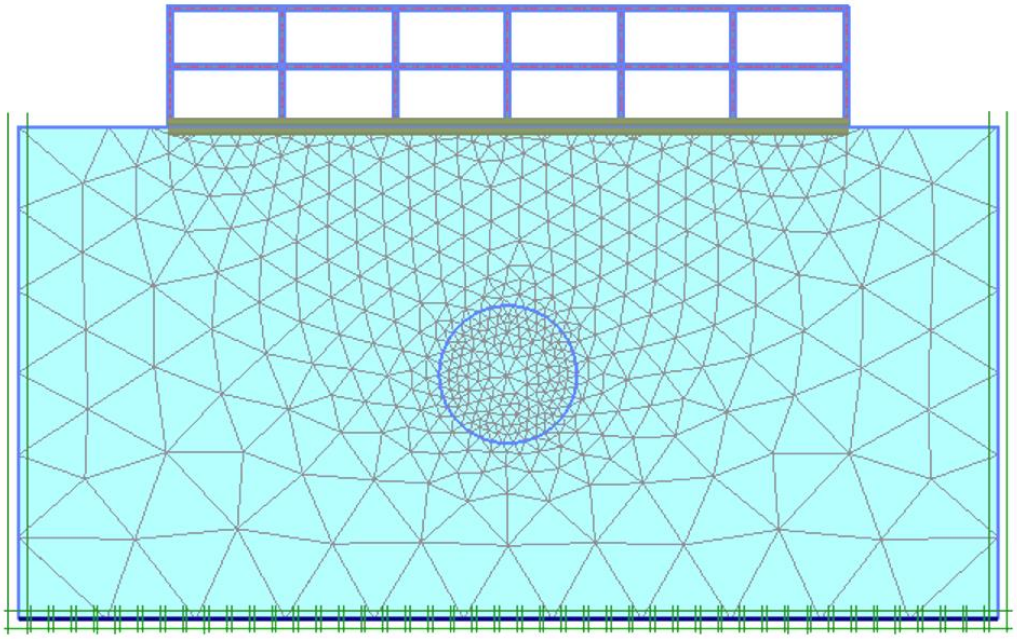

(a)

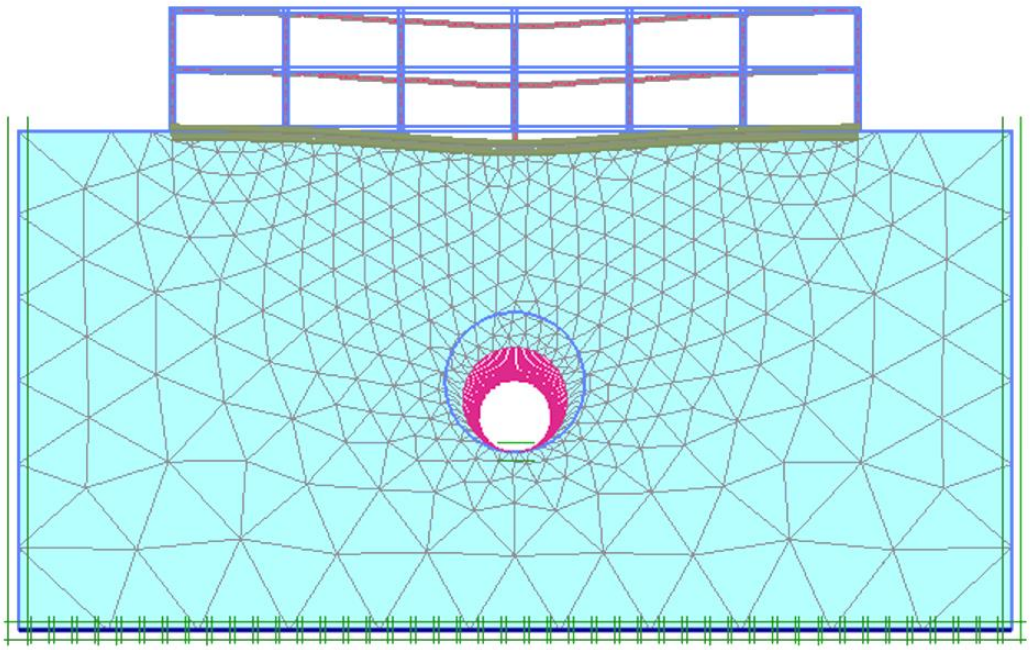

(b)

Figure 5.6. Image of the mesh generation for "Frame" model in PLAXIS 2D a) before tunnelling b) after tunnelling ($\boldsymbol{V_{l,t} = 1.0\%}$).

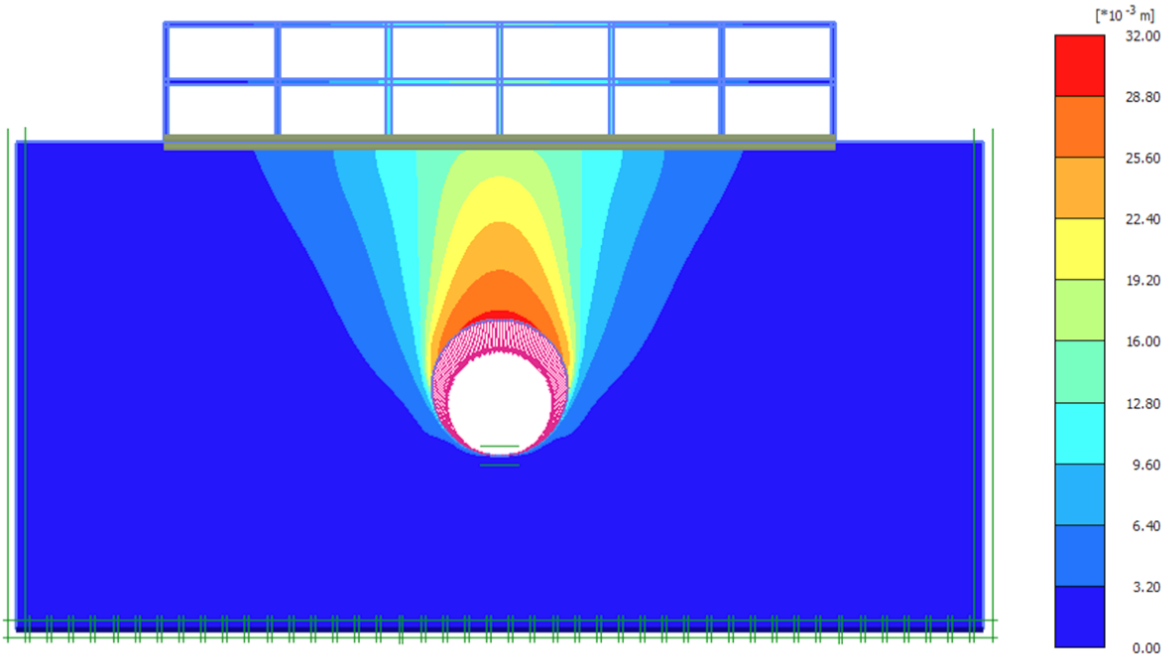

Figure 5.7. Contour of total displacements for "Frame" model ($\boldsymbol{V_{l,t} = 1.0\%}$) in PLAXIS 2D.

5.3.3 Validation of the numerical results

The numerical results of "Greenfield" and "Frame" models are compared with centrifuge results in Figure 5.8(a-f). Figure 5.8(a and b), (c and d), and (e and f) show the vertical and horizontal displacements at the ground surface for $V_{l,t}$= 0.4%, 1.0% and 2.0%, respectively. The centrifuge data which are presented in Xu et al. (2019) are the most appropriate centrifuge results to compare with numerical predictions.

Inspection of Figure 5.8(a-f) reveals that there is a good agreement between numerical and experimental results for both cases of "Greenfield" and "Frame" models, with a slight underestimation of vertical displacements at the soil surface and foundation depth together with the overestimation of the soil horizontal displacements in the numerical solutions if compared to centrifuge tests. Despite this, the foundation horizontal displacements and deformations are minimal.

Xu et al. (2019) reported a gap formed between the soil and the frame foundation interface. In these numerical results, a gap formation is forming and increasing in magnitude with the

volume loss of the tunnel, consistently with the experimental evidence. Slipping also occurs at the soil-foundation interface, as suggested by the negligible movements of the structure in contrast to those of the soil. A good match between experimental and numerical results is observed for the soil horizontal displacements at the larger volume loss.

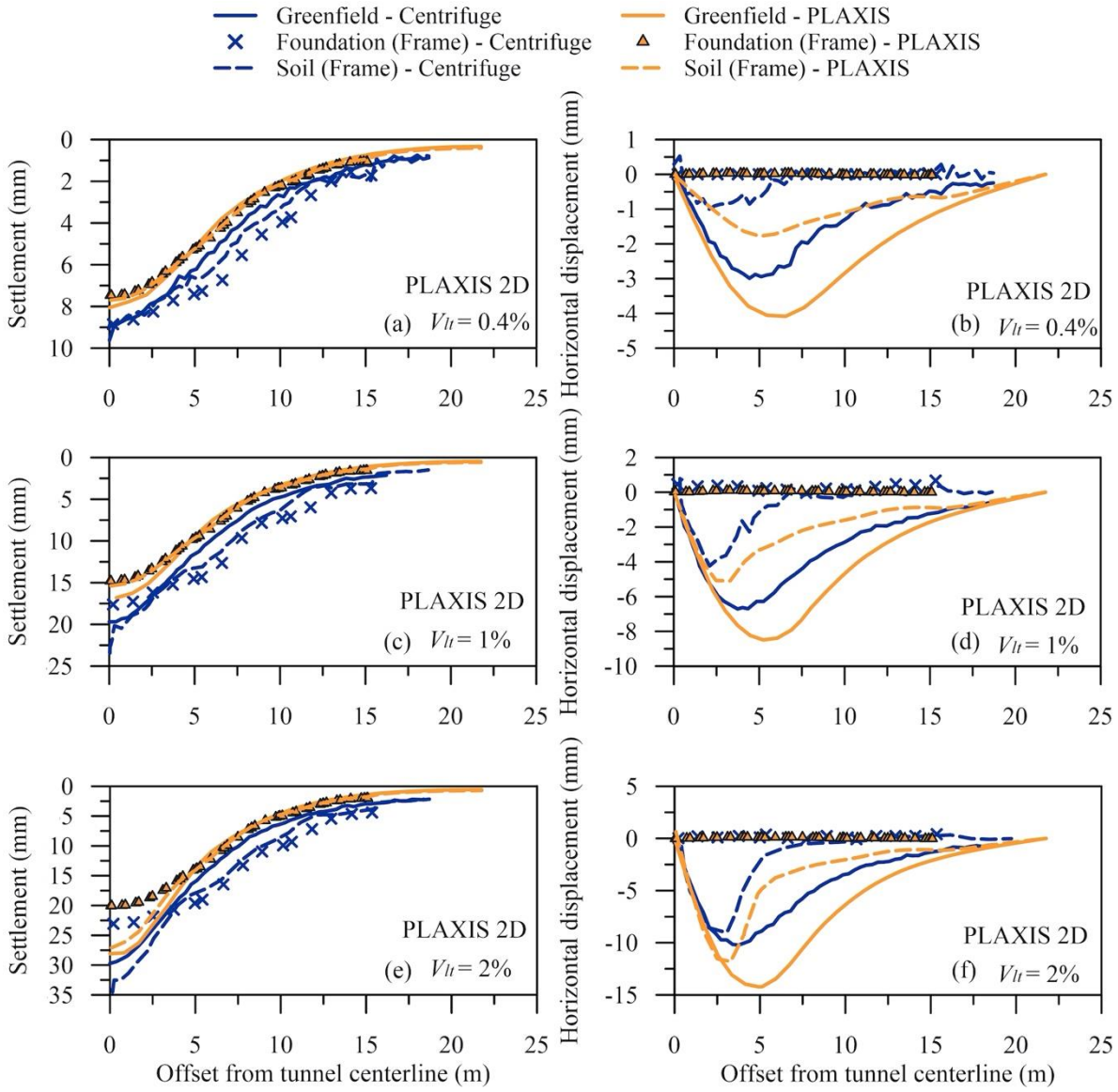

Figure 5.8. Comparison between centrifuge results and numerical predictions (PLAXIS 2D) in "Greenfield" and "Frame" cases ($\boldsymbol{V_{l,t} = 0.4\%,\ 1.0\%,\ \text{and}\ 2.0\%}$) for vertical and horizontal displacements at the ground surface.

5.4 Performed analyses in PLAXIS 3D

In this part of the thesis, two 3D numerical analyses were performed. Both 3D analyses are equivalent to the 2D "Greenfield" and "Frame" analyses that were done in PLAXIS 2D; in fact, these 3D numerical analyses were performed to gain confidence in the 3D model. Identical stages and incremental displacements at the boundary nodes (with 38 nodes at the tunnel cross section) on the tunnel were used to simulate the numerical analyses in PLAXIS 3D.

5.4.1 Greenfield

The 3D model of "Greenfield" conditions has a soil volume 43.52m wide, 21.9m deep, and 17.7m thick in the longitudinal direction. Taking advantage of the plain-strain conditions of the problem, which is discussed in sections 5.4.2 and 4.5.3, only a slice of the 3D prototype was considered, having a length of 8.772m parallel to the tunnel axis. Note that this length corresponds to the assumed spacing in the longitudinal direction between masonry infills, as clarified later. As shown in Figure 5.9, nodes at the bottom of the mesh were constrained in all directions, while those along lateral faces were restrained for normal displacements. The general layout and mesh generation of the problem are shown in Figure 5.10(a and b) for the initial phase and the last phase of applying the displacement fields. Again, also in the 3D model, the 6-node triangular elements are used to model the volume elements of the soil. The mesh generation which is illustrated in Figure 5.10(a) has 10738 elements and 15820. The number of elements for the other volume losses are approximately similar. Finally, the contour of total displacement of "Greenfield" model for the final results is shown in Figure 5.11.

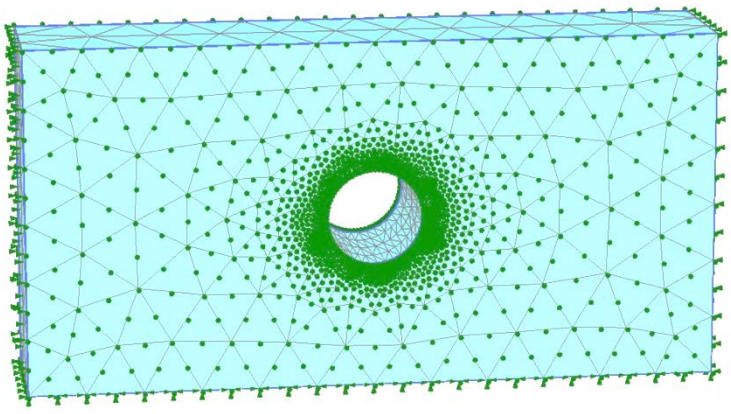

Figure 5.9. Application of boundary conditions in PLAXIS 3D model.

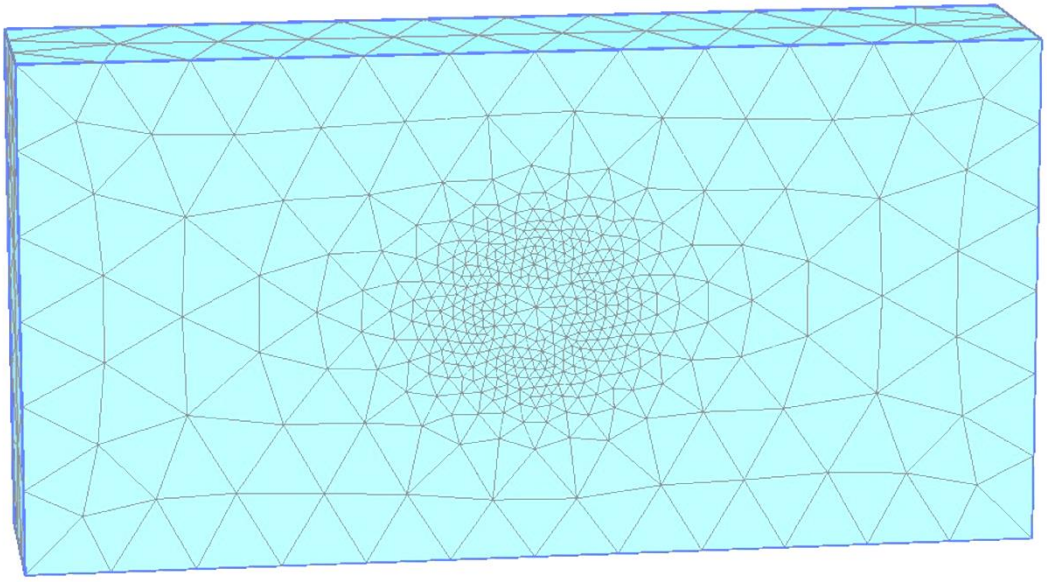

(a)

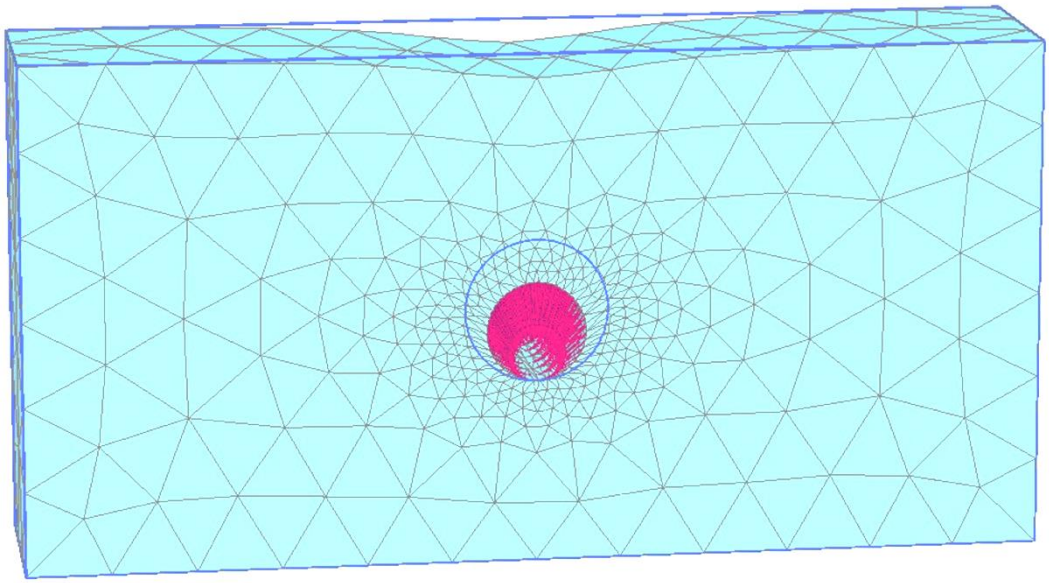

(b)

Figure 5.10. Image of the soil mesh adopted for "Greenfield" model in PLAXIS 3D a) before tunnelling b) after tunnelling ($\boldsymbol{V_{l,t} = 1.0\%}$).

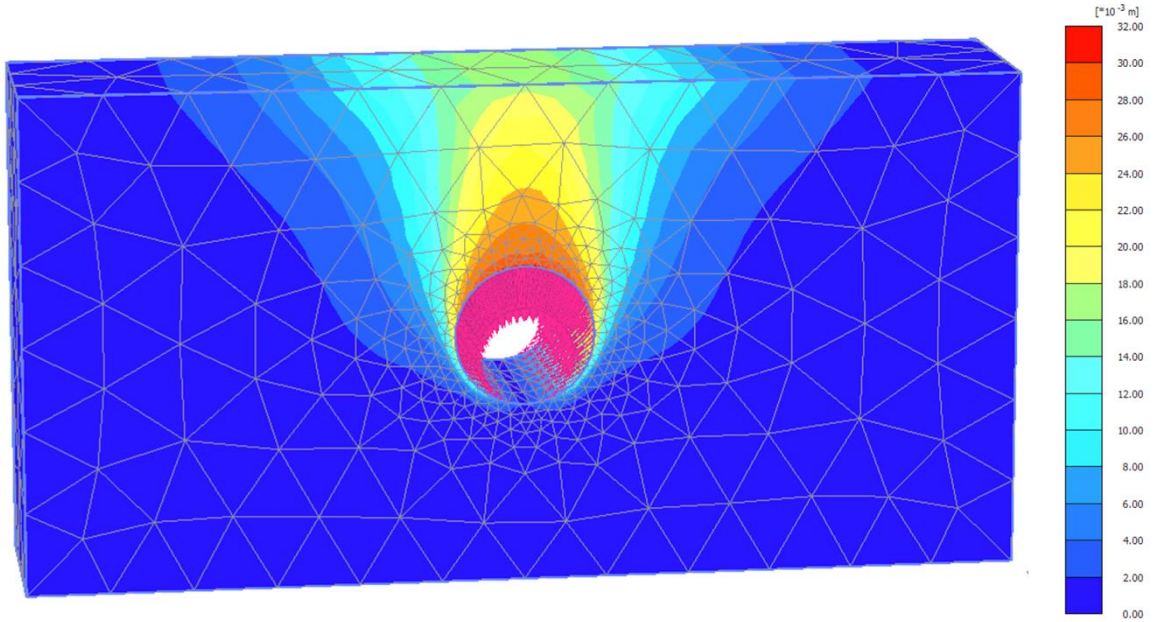

Figure 5.11. Contour of total displacements for "Greenfield" model ($\boldsymbol{V_{l,t} = 1.0\%}$) in PLAXIS 3D.

5.4.2 Frame structures

The frame was discretised with solid elements as in PLAXIS 2D analyses; the use of solid elements for the structure was preferred to plate elements to have a direct estimate of the tunnelling-induced strain distribution. For the structural elements, a linear elastic constitutive law was adopted, with parameters mentioned in section 5.3.2. The soil-structure interface is activated in 3D modelling by considering the same parameters in 2D modelling. In three-dimensional modelling of frame structures, only half of the problem was modelled, considering the symmetry with respect to the tunnel axis. In a way similar to "Greenfield" modelling, only a slide of 8.772m parallel to the tunnel axis was considered for the full 3D prototype (Figure 5.12) .

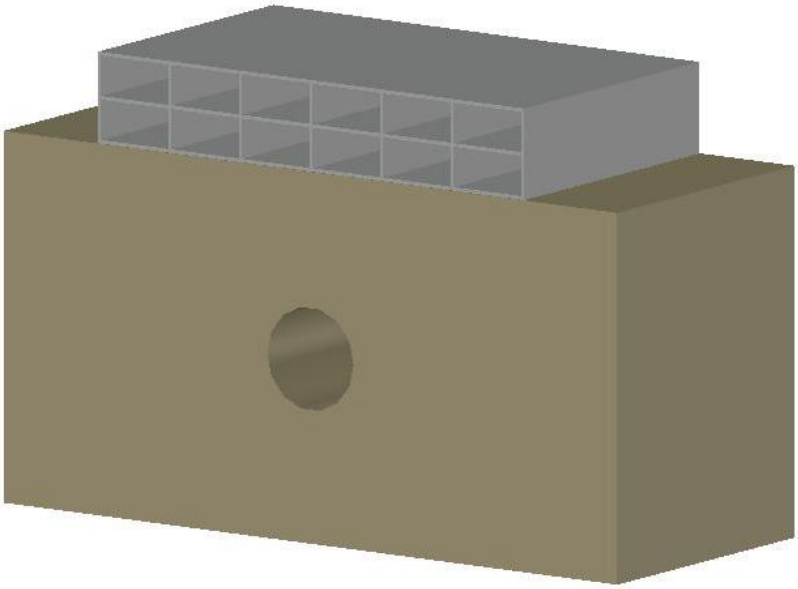

Figure 5.12. Schematic view of central frame and soil.

Figure 5.13(a) illustrates the mesh generation of "Frame" model with 16740 elements and 21981 nodes, and the deformed configuration of this simulation is shown in Figure 5.13(b). The total displacement contour for "Frame" model is plotted in Figure 5.14.

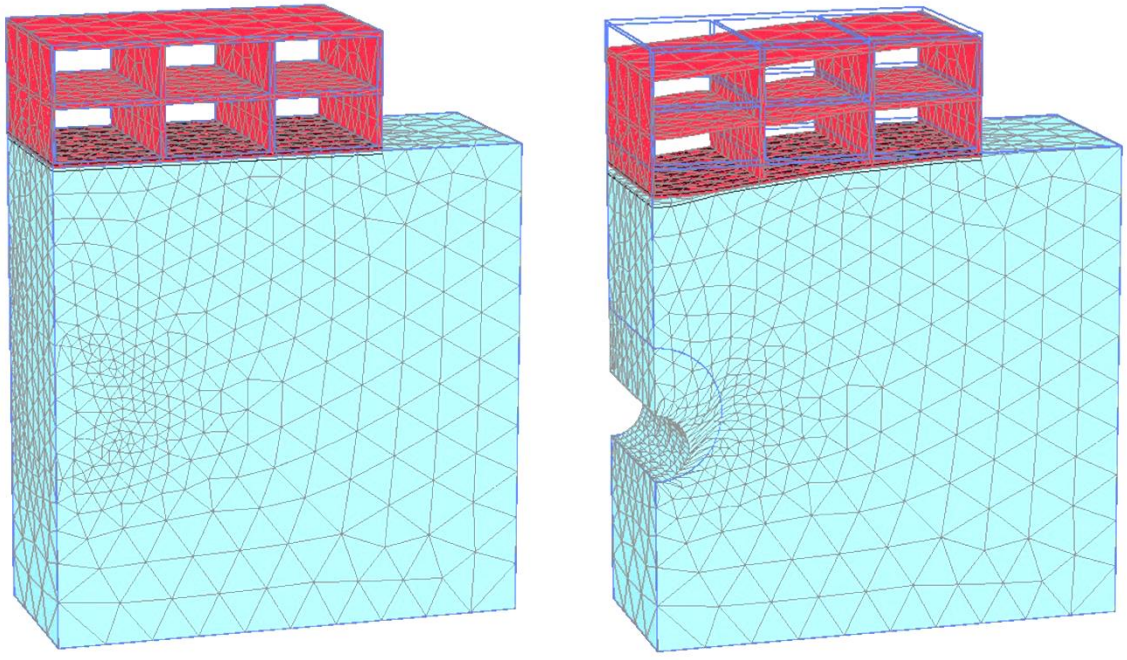

(a) (b)

Figure 5.13. Image of the mesh generation for "Frame" model in PLAXIS 3D a) before tunnelling b) after tunnelling (scaled up 200 times for $\boldsymbol{V_{l,t} = 1.0\%}$).

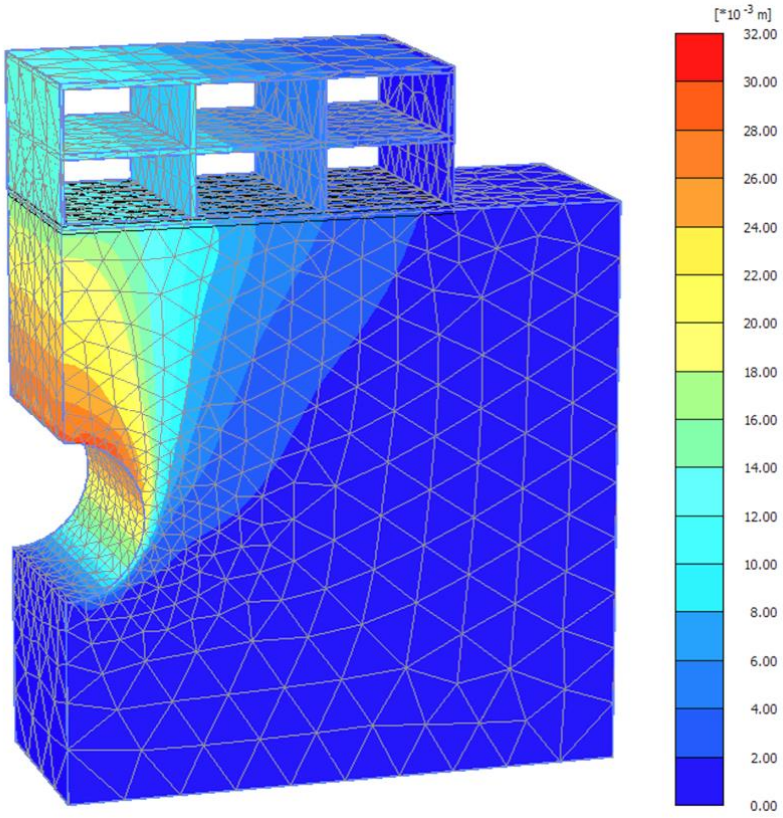

Figure 5.14. Contour of total displacements for "Frame" model ($\boldsymbol{V_{l,t} = 1.0\%}$) in PLAXIS 3D.

5.4.3 Validation of the numerical results

Figure 5.15 shows the vertical and horizontal displacements at the ground surface and foundation obtained from 3D modelling of greenfield and active bare frame for $V_{l,t} = 0.4\%$, 1.0%, and 2.0%.

A brief look at Figure 5.8 and Figure 5.15 shows that the numerical results in 3D modelling behaved differently, compared to 2D modelling, through the activation of frame structure. The vertical displacements of soil and foundation in the case of "Frame" 3D analysis indicate that the gap is formed at the larger volume losses (e.g., $V_{l,t} = 1.0\%$, and 2.0%), consistently with the experimental evidence, while 2D numerical results were characterised by the gap formation only at $V_{l,t} = 2.0\%$. In addition, 3D results have a better match with experiments in terms of horizontal displacements of the soil beneath the frame in comparison to 2D results for different volume losses of the tunnel. The sliding movement of frame is occurred due to the null movements in the transverse direction for both 2D and 3D results. In summary, these numerical

results show the robustness of 3D modelling to simulate the main features of this complex soil-structure interaction problem. As such, all the numerical analyses in the next chapter are simulated by PLAXIS 3D. Also, simulation of masonry infills in 2D modelling in not possible because of adopting plain strain conditions.

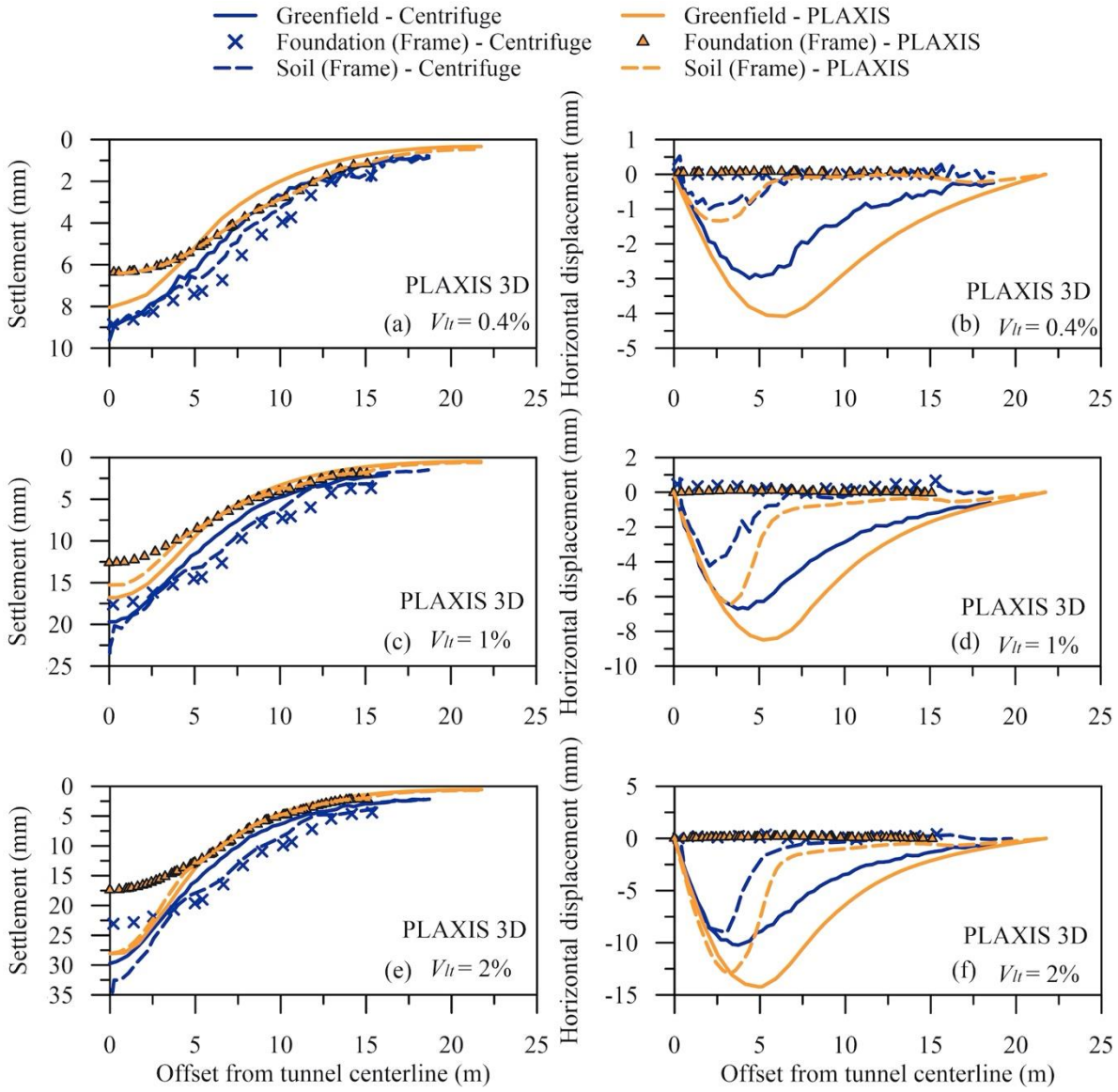

Figure 5.15. Comparison between centrifuge results and numerical predictions (PLAXIS 3D) in "Greenfield" and "Frame" cases ($\boldsymbol{V_{l,t} = 0.4\%,\ 1.0\%,\ \text{and}\ 2.0\%}$) for vertical and horizontal displacements at the ground surface.

Chapter. 6. Tunnel frame with infills

To study the effects of the infill walls in the frame, masonry infills were added to the frame in the central transverse section of the model. In numerical modelling, the infill walls were created in PLAXIS 3D with solid elements, similarly as for the soil and frame structures, to have evidence of tensile strain distribution. For the infills, a linear elastic constitutive law was set with the constants equal to $E = 4.0$ GPa, $\nu = 0.2$, and $\gamma = 13\ \mathrm{kN/m^3}$ (Cobanoglu et al., 2017). Modelling of infill walls requires the use of a very dense mesh discretization for the infills themself. A thickness of 0.25m was assumed for the infills. Figure 6.1(a and b) shows the positioning of the infill walls inside the frame structures with their prototype dimensions for two heights of the building. A slice of the frame structure was taken as a portion with a length of 8.772m parallel to the tunnel axis from the full 3D model shown in Figure 6.1(a and b). The other dimensions were selected as those of the F2t3b6L test.

The full stiffness and weight of the infills were used to produce realistic conditions (named "Frame with stiff infills"). Additionally, a further analysis was carried out with weightless and fully flexible infills (named "Frame with flexible infills") to assess the relative influence of the stiffness and weight of the infill panels on the expected damage. Both analyses were performed with the four stages mentioned in chapter 5, activating the infills during the third stage.

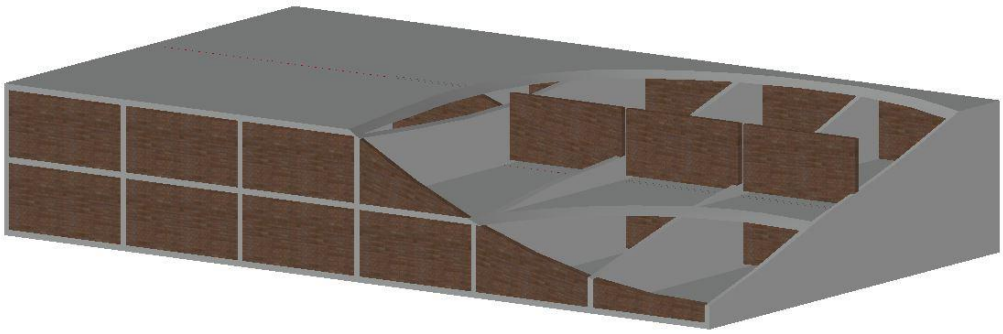

(a)

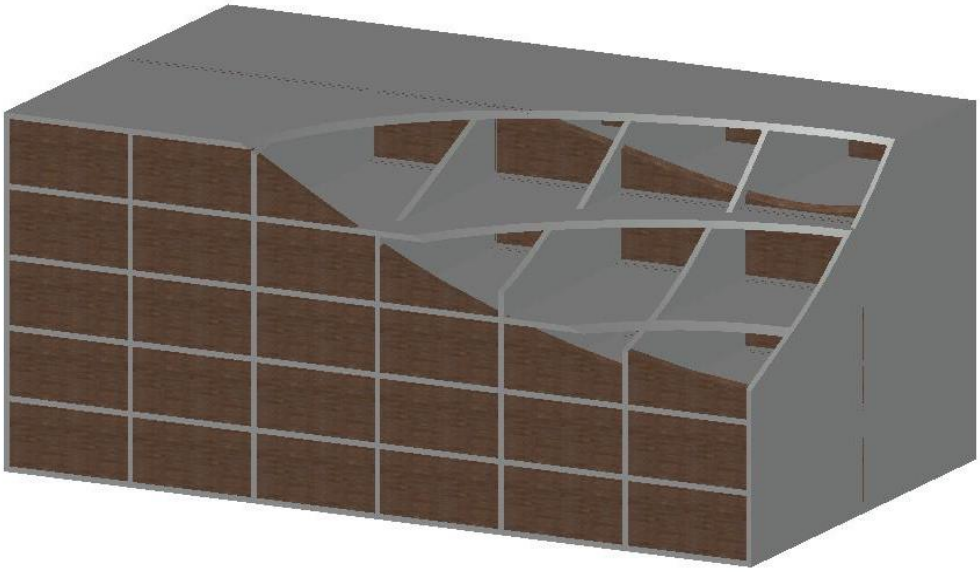

(b)

Figure 6.1. Detail of the frame structure with masonry infills for (a) 2-storey and (b) 5-storey buildings

In this study, eight framed building models were considered to investigate the effect of the eccentricity and height of the building, using the same thickness (t) of the building elements (foundation, elevated slabs, and walls) as for the F2t3b6L test. Figure 6.2(a-c) shows the geometrical view of all framed models analysed in this study.

The frame models were labelled based on their characteristics as (x)Se(y)L/S: x indicated the number of storeys, y the eccentricity (*e*/*B*= 0, 0.2, 0.5), and the suffixes L and S for transversely long and short structures, respectively. Furthermore, all of these cases were classified into three subsets considering the effect of the infill walls. As mentioned in chapter 5, these three subsets included the bare frame and the frame with flexible and stiff infills, corresponding respectively to the suffix "_Bare", "_Flex", and "_Stiff" (Figure 6.2). As an example, the labels of the 5Se05L model were "5Se05L_Bare", "5Se05L_Flex", and "5Se05L_Stiff" for the three subsets related to infill walls. Considering the three values of the tunnel volume loss taken into account (e.g., $V_{l,t} = 0.4\%,\ 1.0\%,\ \text{and}\ 2.0\%$), a total number of 72 numerical models were run.

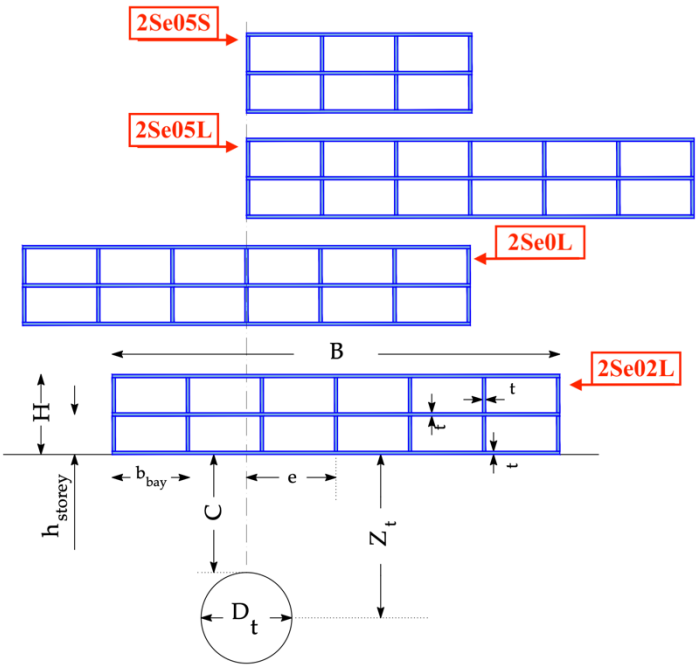
2Se05S
2Se05L
2Se0L
B
2Se02L
H
t
t
t
b bay
e
h storey
C
Z t
D t

(a)

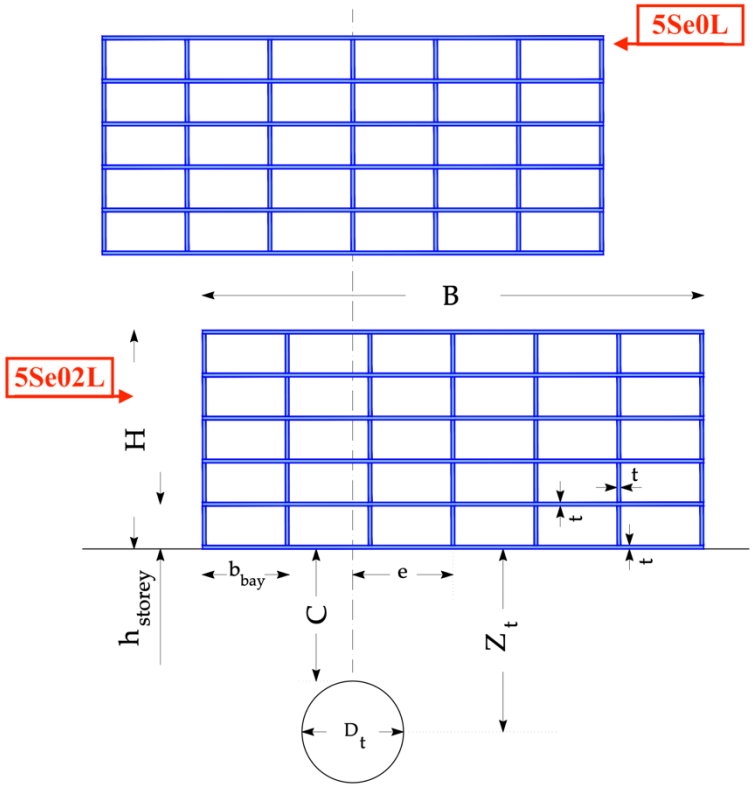
5Se0L
B
5Se02L
H
t
t
t
b bay
e
h storey
C
Z t
D t

(b)

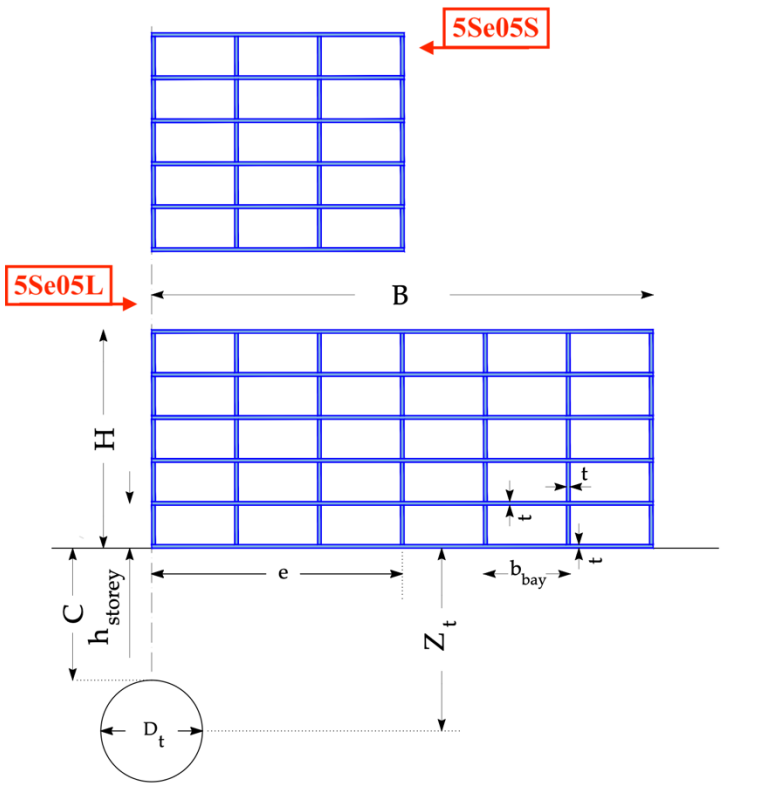

(c)

Figure 6.2. Geometrical view of numerical models (a) 2Se0L, 2Se02L, 2Se05L, and 2Se0S, (b) 5Se0L and 5Se02L, (c) 5Se05L and 5Se05S

6.1 Central structures: the effects of building length

To investigate the effects of building length for centred structures, the numerical models 2Se0L and 5Se0L were run in PLAXIS 3D for different volume losses.

6.1.1 Numerical model: 2Se0L

The deformed configurations of frames 2Se0L_Flex and 2Se0L_Stiff for $V_{l,t} = 1.0\%$ are illustrated in Figure 6.3(a and b), with displacements scaled up 200 times. As shown in the figures below, only half of the problem was modelled, considering the symmetry with respect to the tunnel axis. Figure 5.13(b) and Figure 6.3(a) illustrate that the same response is obtained for models 2Se0L_Bare and 2Se0L_Flex, as expected. Comparison between Figure 6.3(a and b) shows that the gap size at the soil-structure interface is larger in the frame with stiff infills than in the bare frame.

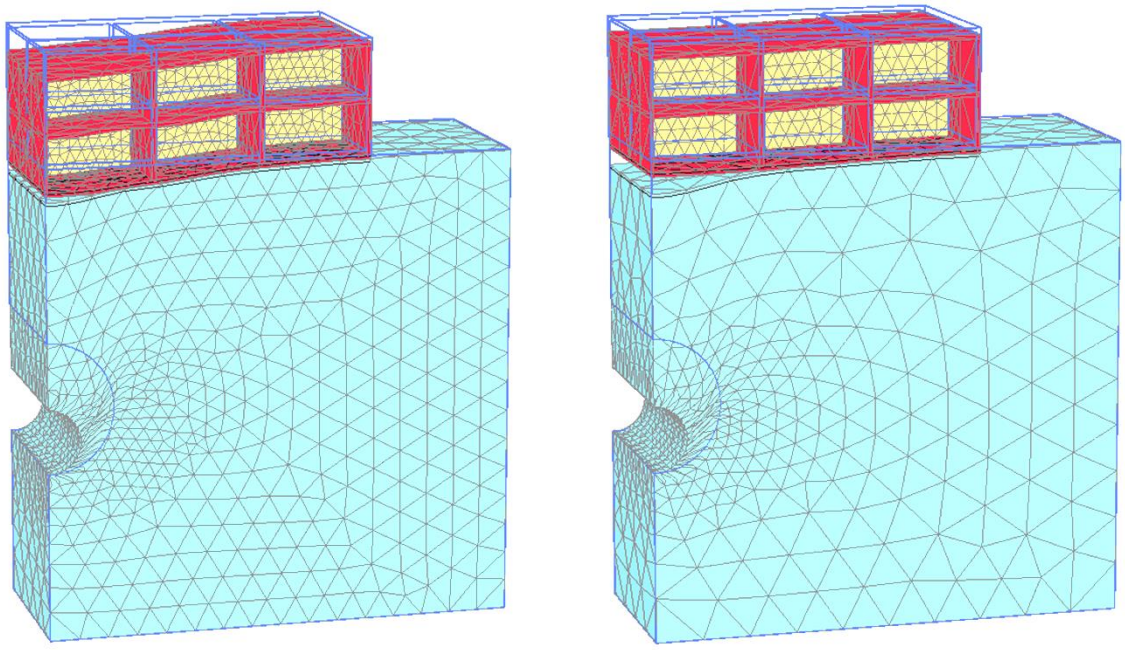

(a) (b)

Figure 6.3. Comparison between deformed configurations for a) **2Se0L_Flex** b) **2Se0L_Stiff** models in PLAXIS 3D ($\boldsymbol{V_{l,t} = 1.0\%}$).

Figure 6.4(a-f) summarises the results of analyses with stiff and flexible infill panels for models 2Se0L_Bare, 2Se0L_Flex, and 2Se0L_Stiff. The gap at the soil-structure interface in frames with stiff infill panels starts appearing at $V_{l,t} = 0.4\%$, while the analysis with flexible infill panels does not manifest this behaviour. Also, the gap formation is concentrated in the central part of the structure, and it grows at larger volume losses. This implies that the activation of stiffer infills is associated to a stiffer response in terms of vertical displacements at the frame foundation level.

While the ground surface for the frame with stiff infills was characterised by larger horizontal displacements than in the case of the frame with flexible infills, the movements at the foundation level are nearly zero for all frames. Also, it can be observed that the horizontal displacements of the soil beneath the frame with stiff infills are similar to those obtained in the greenfield case by increasing the volume loss of the tunnel.

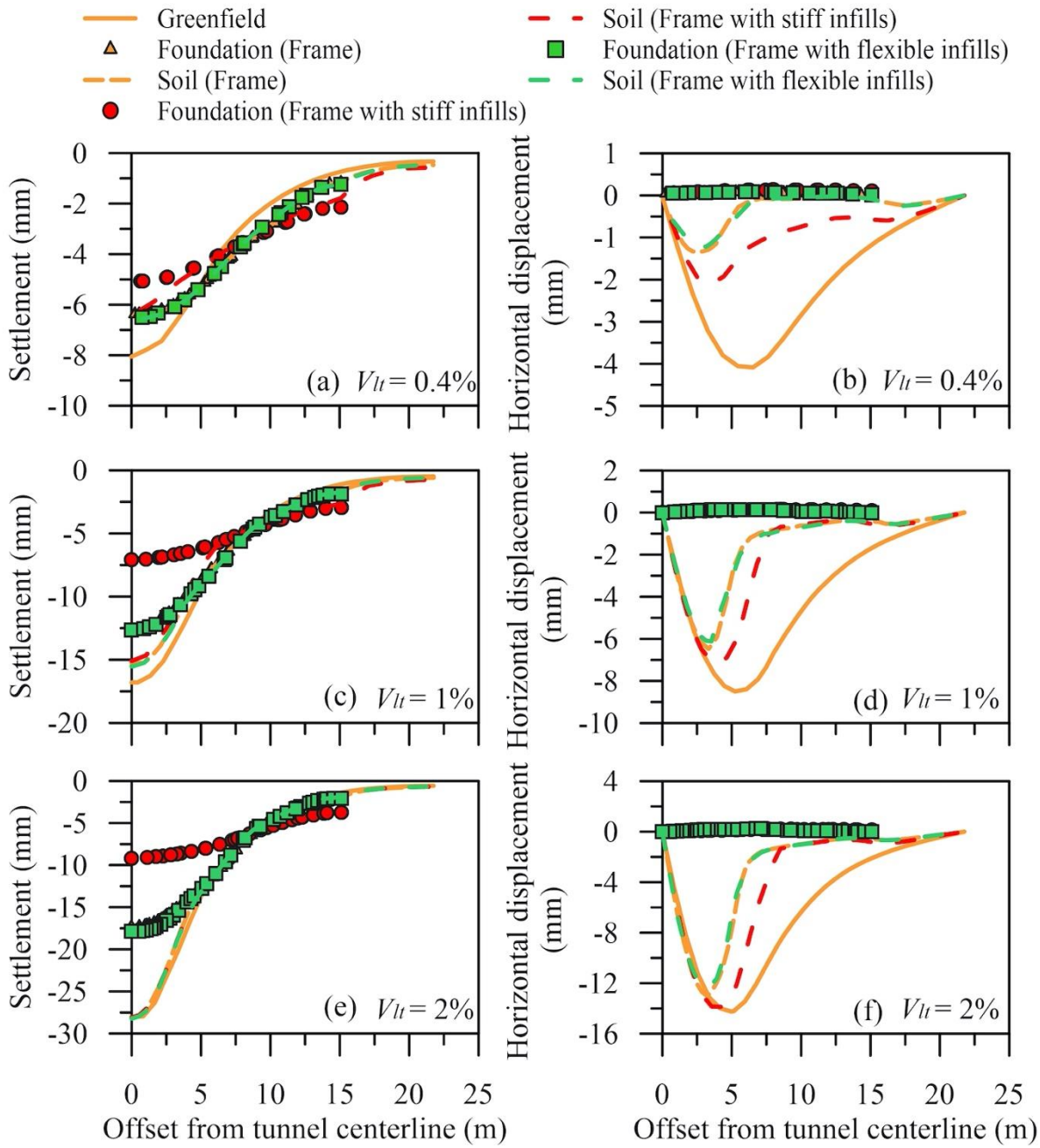

Figure 6.4. Comparison between numerical predictions for models **2Se0L_Bare**, **2Se0L_Flex**, and **2Se0L_Stiff** ($\boldsymbol{V_{l,t} = 0.4\%,\ 1.0\%,\ \text{and } 2.0\%}$).

6.1.2 Numerical model: 5Se0L

The deformed configurations of the frame model 5Se0L (i.e. 5-storey building) for flexible and stiff infill panels are reported in Figure 6.5. These results show that the gap is only formed when stiff infill panels are activated. The gap size in the 2-storey building analysis (Figure 6.3) was however larger than that in the 5-storey building one, possibly related to the structural

stiffness and weight of the building. In other words, despite the greater stiffness, the higher the pressure at the foundation, the smaller the gap formation for centred structures.

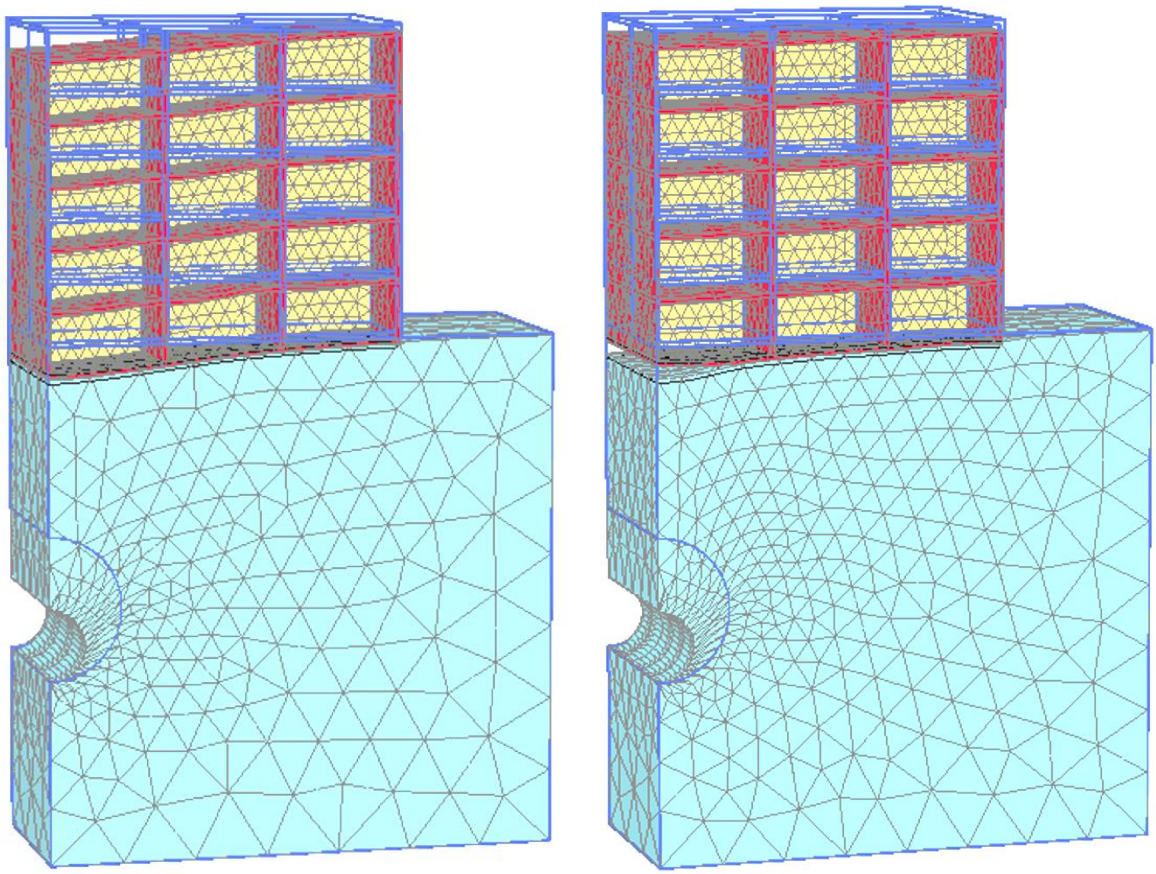

(a) (b)

Figure 6.5. Comparison between deformed configurations for a) **5Se0L_Flex** b) **5Se0L_Stiff** models in PLAXIS 3D ($\boldsymbol{V_{l,t} = 1.0\%}$).

In Figure 6.6, the settlements indicate that the foundations of stiffer frames settled slightly more than the flexible frames at the edges of the framed building models; also this behaviour is more evident for 5-storey buildings than 2-storey buildings. In Figure 6.6, the flexible frame with 5-storey buildings is characterised by a gap formation beneath the centrally located structures only for the higher value of volume losses (e.g., $V_{lt} = 2.0\%$), similarly to the case of the flexible frame for 2-storey buildings (Figure 6.4(c and e)). The foundation settlements depicted in Figure 6.4 and Figure 6.6 indicate that an increase in stiffness decreases the distortions of centrally located structures. Slipping also occurs at the soil foundation interface, as suggested by the negligible movements of the structure in contrast to those of the soil, which coincide with those obtained in greenfield conditions right above the tunnel.

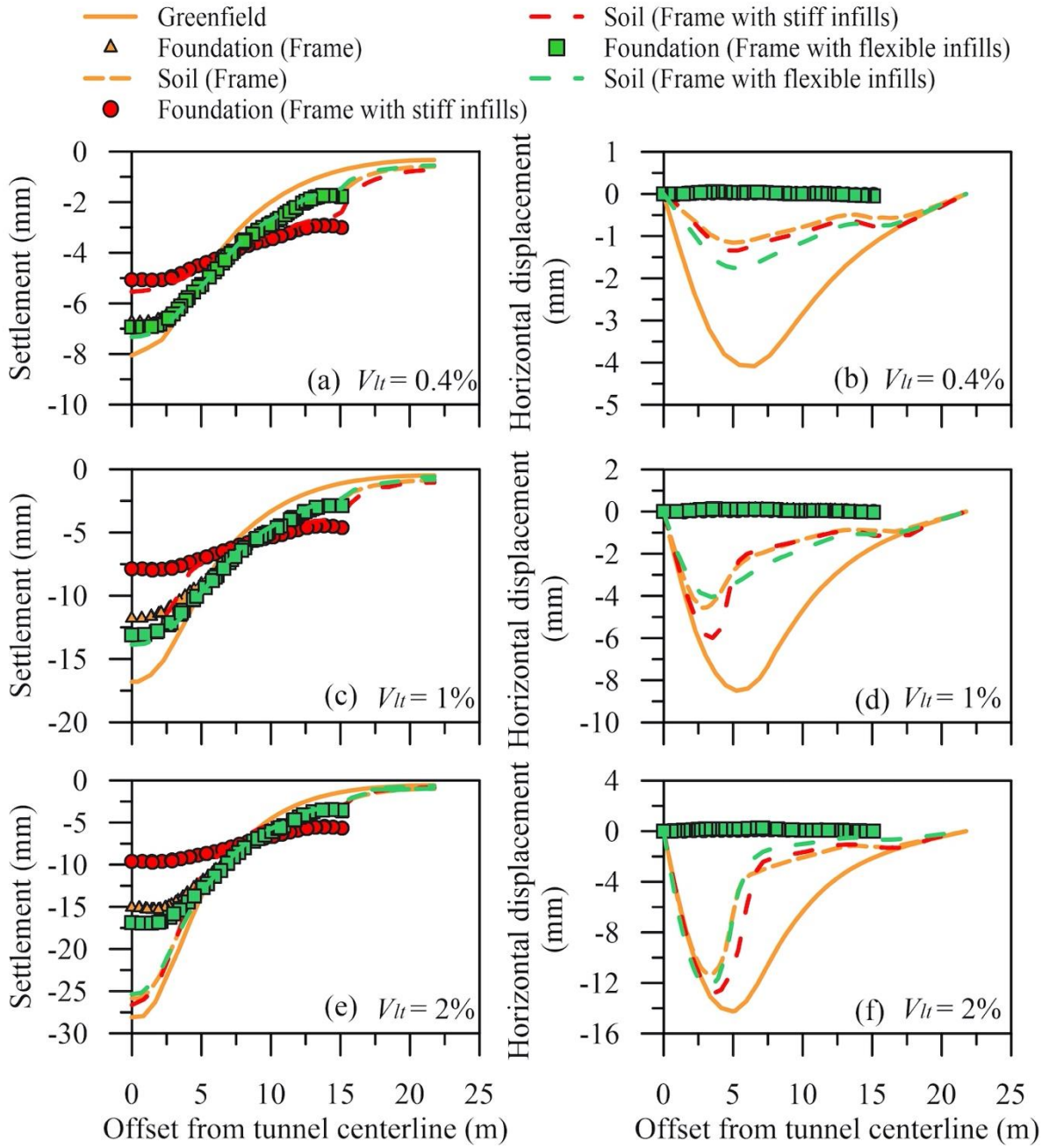

Figure 6.6. Comparison between numerical predictions for models **5Se0L_Bare**, **5Se0L_Flex**, and **5Se0L_Stiff** ($V_{l,t}$ = 0.4%, 1.0%, and 2.0%).

6.2 Eccentric structures: the effects of building tilt

As shown in Figure 6.2, a total of 3 cases were considered or each of the 2-storey and 5-storey eccentric buildings. To sum up, considering also the three selected values of the tunnel volume loss, a total of 54 models were simulated in PLAXIS 3D to explore the effects of eccentricity.

The results in all 2-storey (e.g., models 2Se02L, 2Se05L, 2Se05S) and 5-storey models (e.g., models 5Se02L, 5Se05L, 5Se05S) are illustrated in the following figures:

6.2.1 Numerical model: 2Se02L

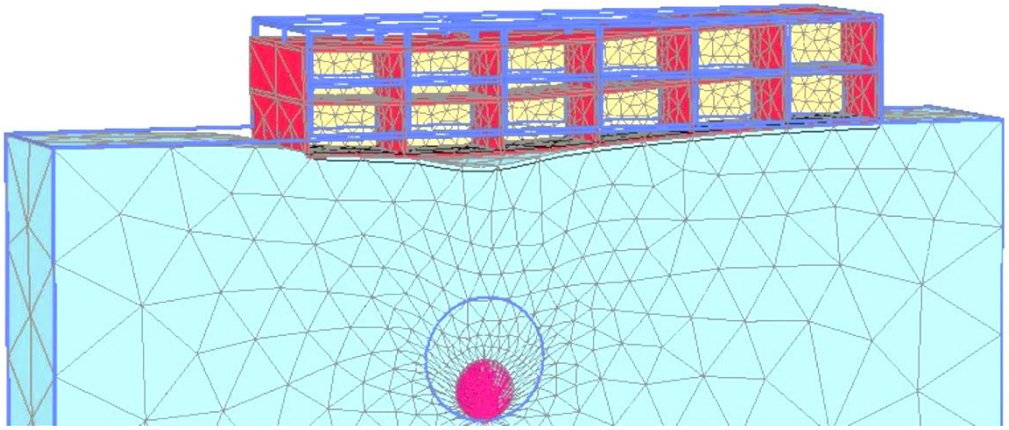

(a)

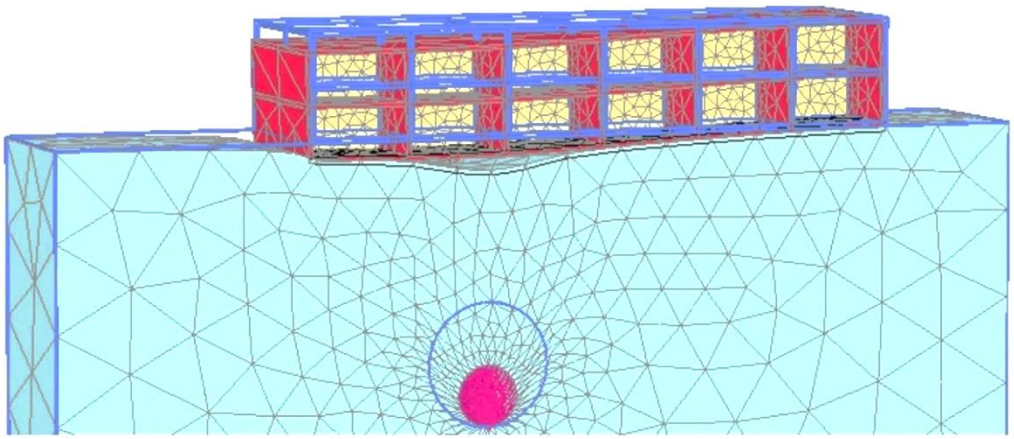

(b)

Figure 6.7. Comparison between deformed configurations (scaled up 100 times) for a) **2Se02L_Flex** b) **2Se02L_Stiff** models in PLAXIS 3D ($\boldsymbol{V_{l,t} = 1.0\%}$).

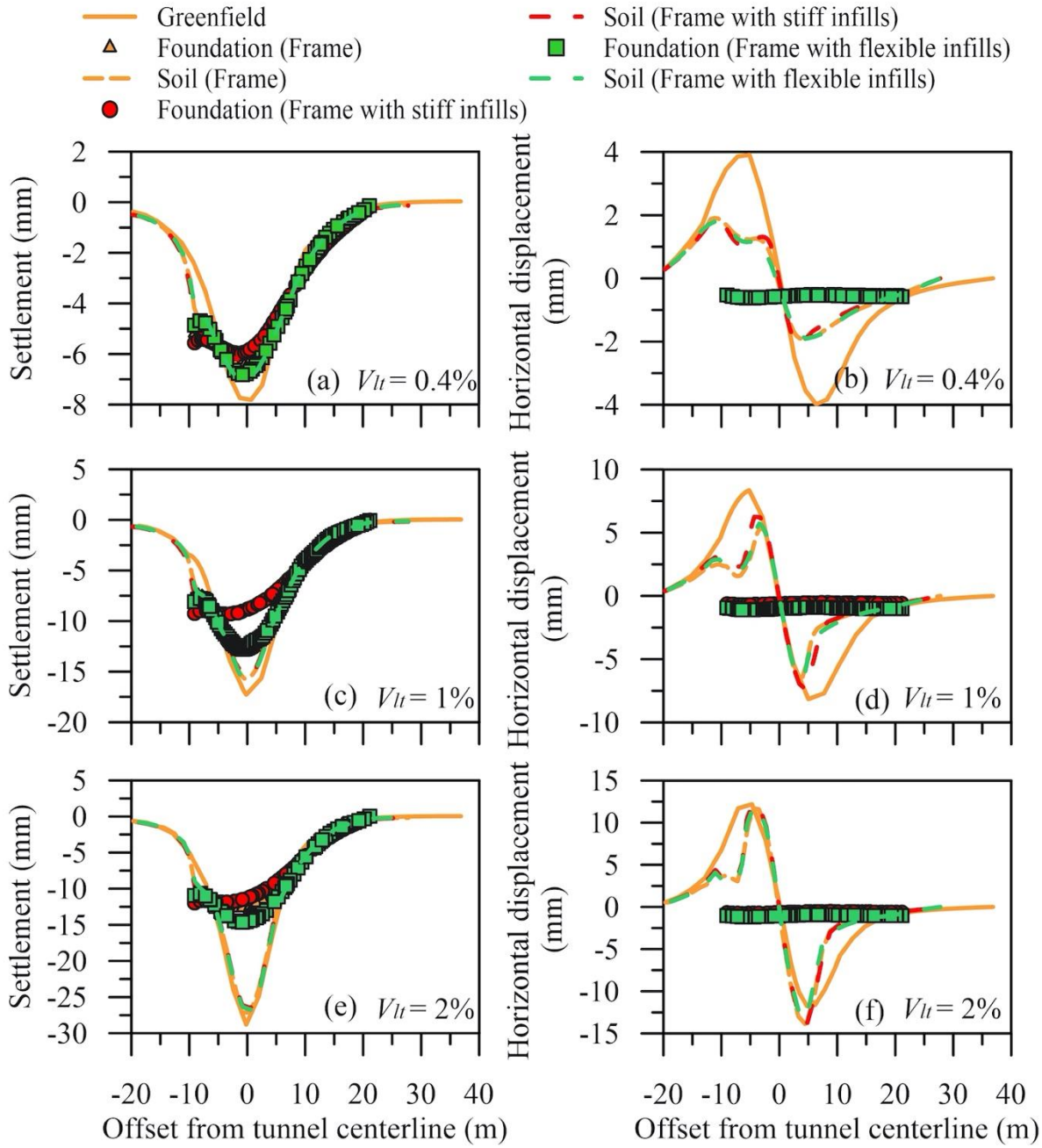

Figure 6.8. Comparison between numerical predictions for models **2Se02L_Bare**, **2Se02L_Flex**, and **2Se02L_Stiff** ($\boldsymbol{V_{l,t} = 0.4\%,\ 1.0\%,\ \text{and}\ 2.0\%}$).

Figure 6.7 illustrates the deformed configurations for the eccentic frames (*e*/*B*= 0.2) with flexible and stiff infills. As it can be seen in Figure 6.7, the frame movement to the left is notable in comparison with the initial position of the frame. Figure 6.8 shows that the gap formation clearly develops by increasing the volume loss of the tunnel, and also it occurs beneath the left side of the centreline due to the position of the building. In Figure 6.8, settlements of soil beneath the frame are nearly close to greenfield condition at the larger volume loss of tunnel (e.g., $V_{lt} = 1.0\%,\ \text{and}\ 2.0\%$). The ground surface displacements on the

left edge of the frame are increased if compared with the greenfield displacements, thus leading to an extra depression in a surface. This evidence could be related to the movements of the frame on its left side due to the horizontal displacements of the foundation (Figure 6.8).

6.2.2 Numerical model: 2Se05L

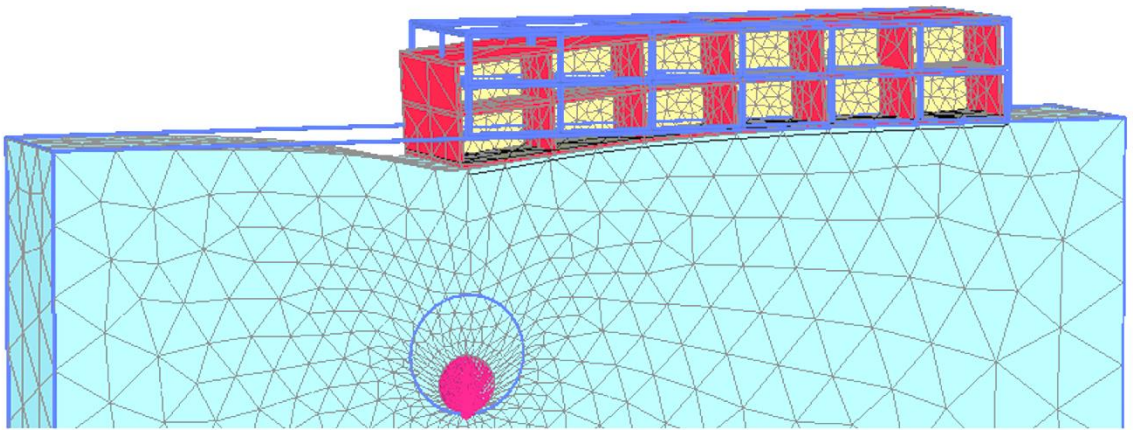

(a)

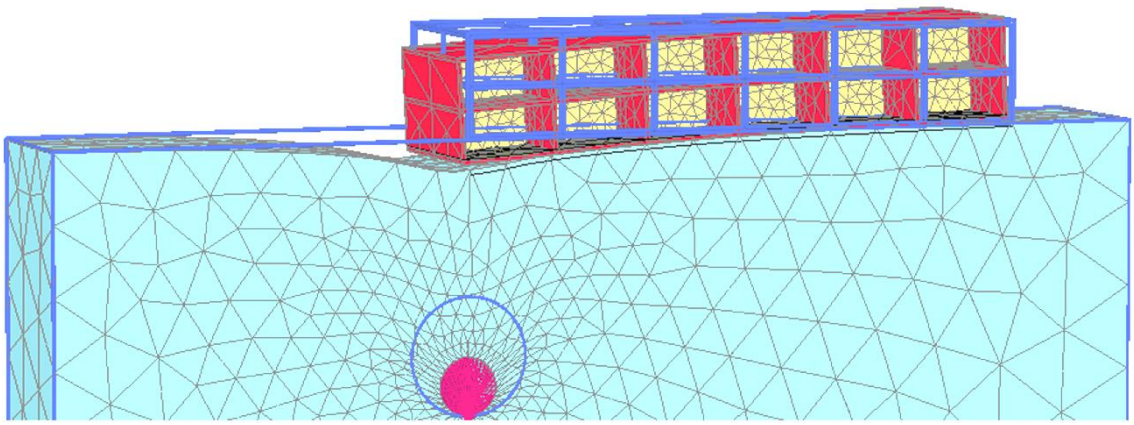

(b)

Figure 6.9. Comparison between deformed configurations (scaled up 100 times) for a) **2Se05L_Flex** b) **2Se05L_Stiff** models in PLAXIS 3D ($\boldsymbol{V_{l,t} = 1.0}$%).

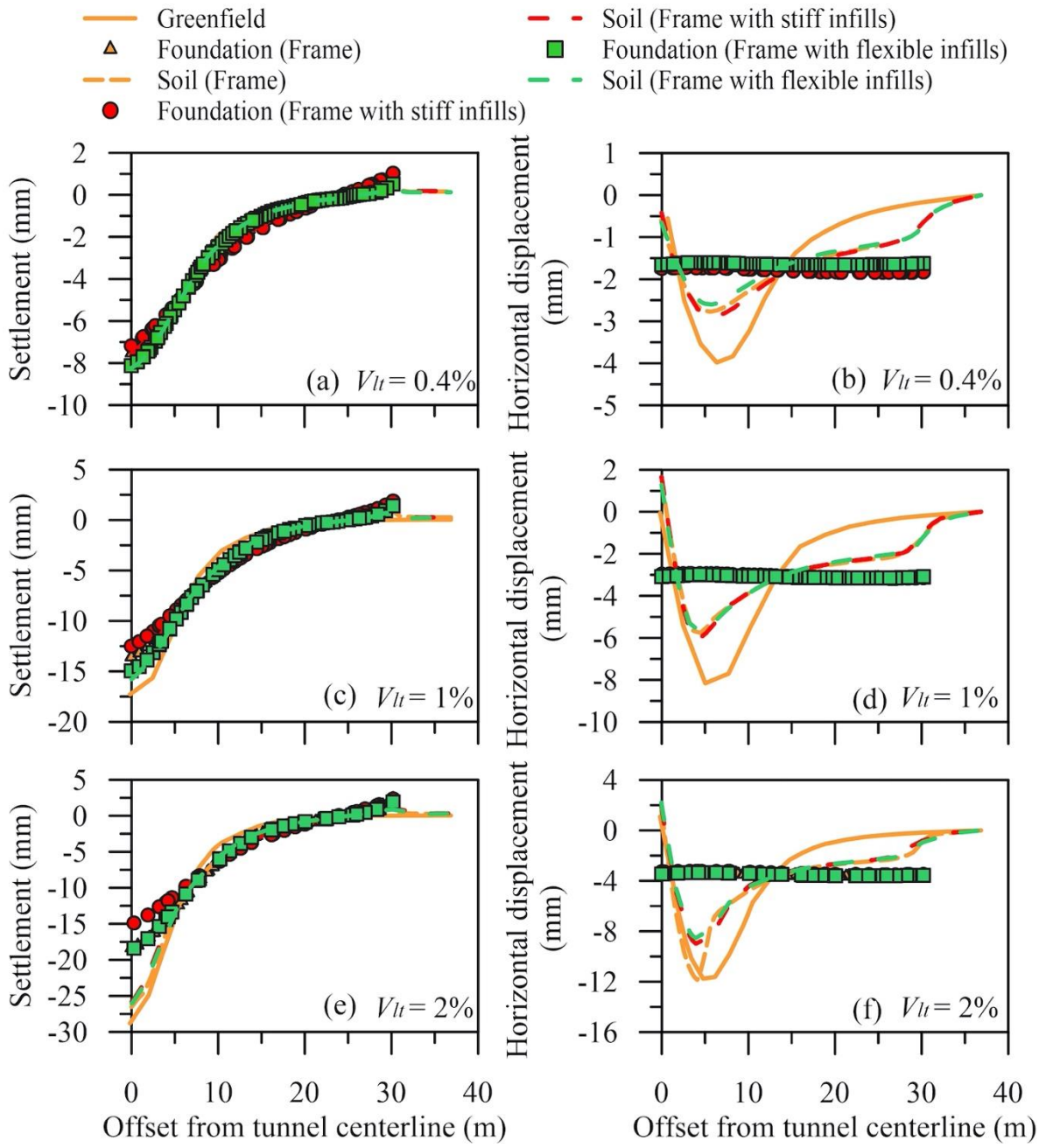

Figure 6.10. Comparison between numerical predictions for models **2Se05L_Bare**, **2Se05L_Flex**, and **2Se05L_Stiff** ($\boldsymbol{V_{l,t}}$ **= 0.4%, 1.0%, and 2.0%**).

The formation of a gap for the frame with stiff infills is evident in the deformed configuration shown in Figure 6.9. In Figure 6.10, the vertical displacements of the foundation for frames with flexible and stiff infill panels have almost the same values. The size of the gap formation, only observed for tunnel volume loss equal to 1.0% and 2.0%, is considerably smaller than the previous models (such 2Se0L and 2Se02L). The other observation related to Figure 6.10 is that the right side of the frame experienced an upward movement due to the increment of eccentricity. The horizontal displacements of the foundations in the model 2Se05L are

considerably larger than those in the model 2Se02L. The horizontal displacements of the soil beneath the frame on the right side are larger than the greenfield movements.

6.2.3 Numerical model: 2Se05S

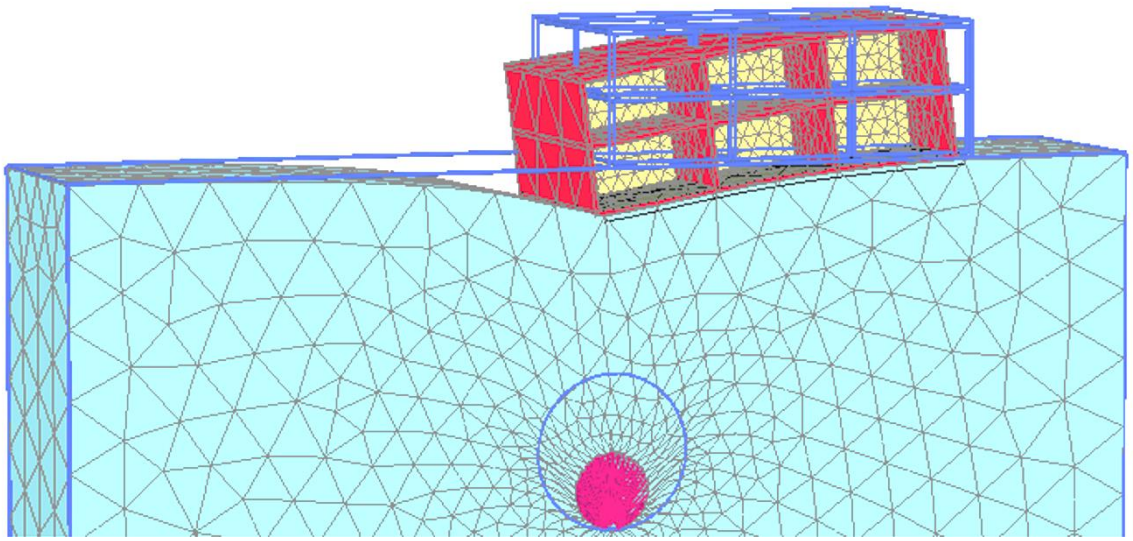

(a)

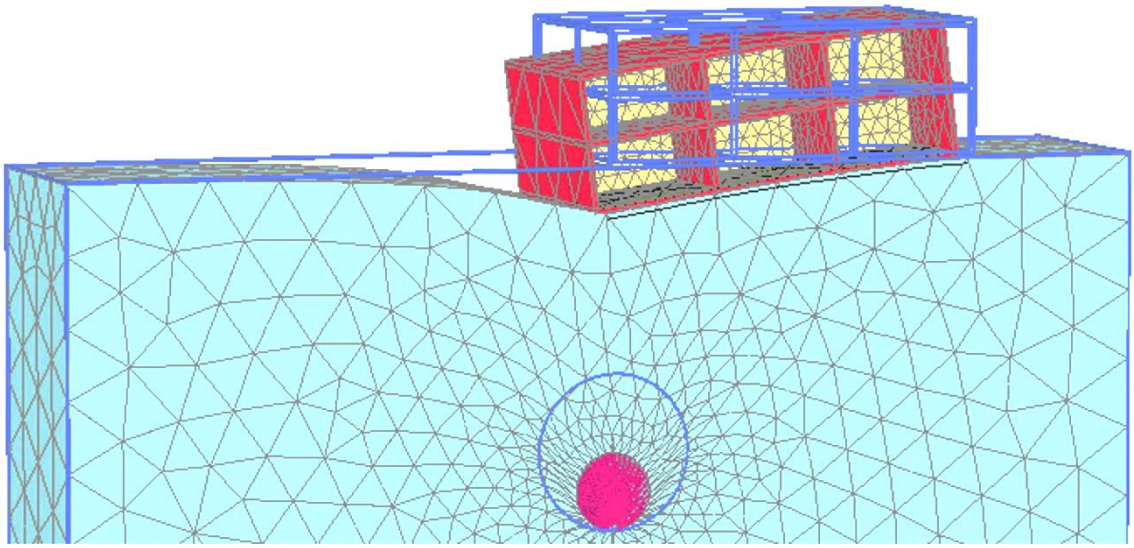

(b)

Figure 6.11. Comparison between deformed configurations (scaled up 100 times) for a) **2Se05S_Flex** b) **2Se05S_Stiff** models in PLAXIS 3D ($\boldsymbol{V_{l,t} = 1.0\%}$).

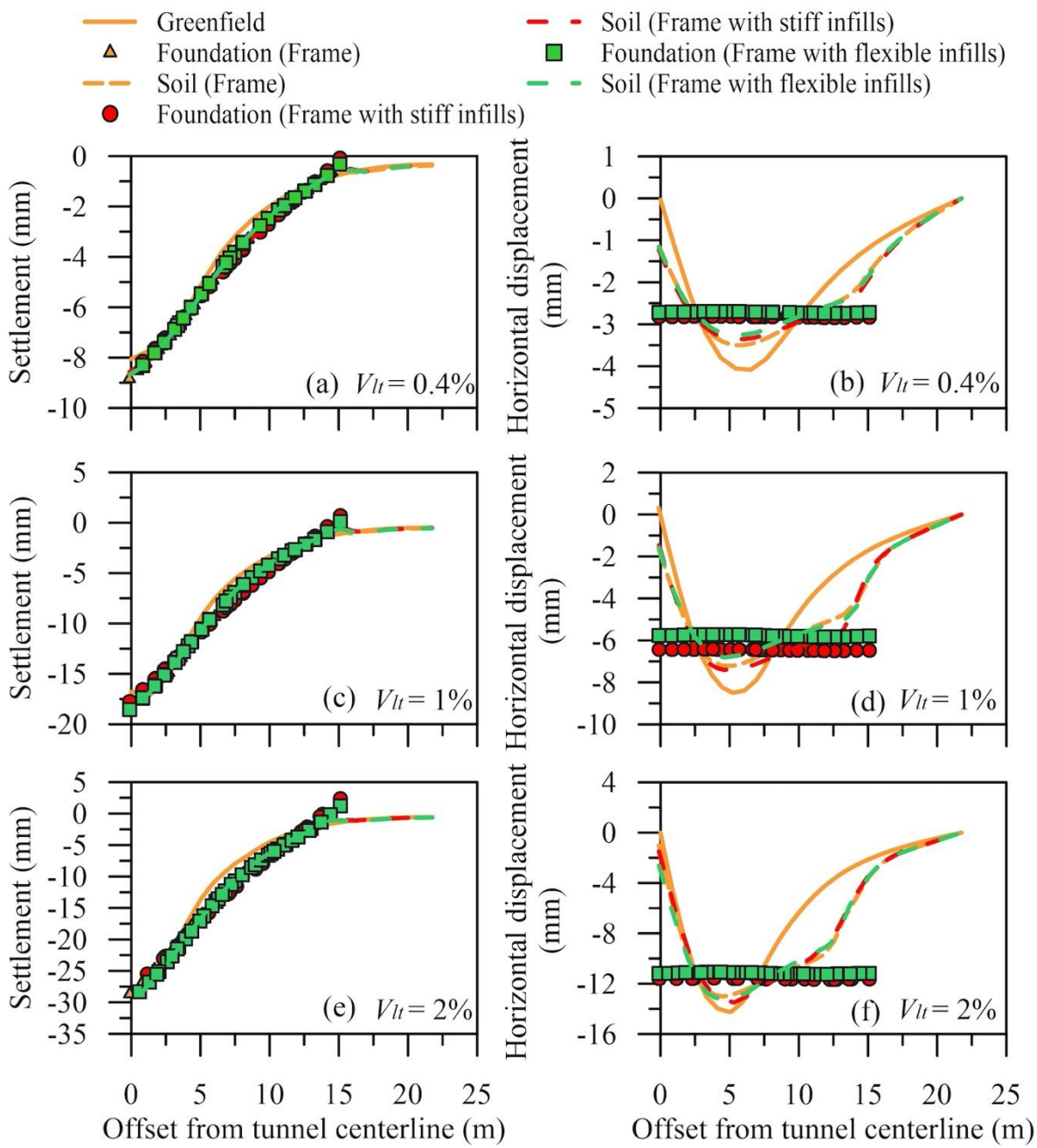

Figure 6.12. Comparison between numerical predictions for models **2Se05S_Bare**, **2Se05S_Flex**, and **2Se05S_Stiff** ($V_{l,t}$ = **0.4%, 1.0%, and 2.0%**).

The results obtained for the short frames in Figure 6.12 are similar to those of long frames with the same eccentricity ($e/B = 0.5$), with few differences. Firstly, larger settlements were experienced all along the short frame's foundation, while the longer frames were characterised by noticeable settlements only in some parts. This statement is clearly evident in the deformed

configurations included in Figure 6.11 and Figure 6.9. Secondly, the horizontal displacements in short frames are significantly larger than those in the longer frames.

6.2.4 Numerical model: 5Se02L

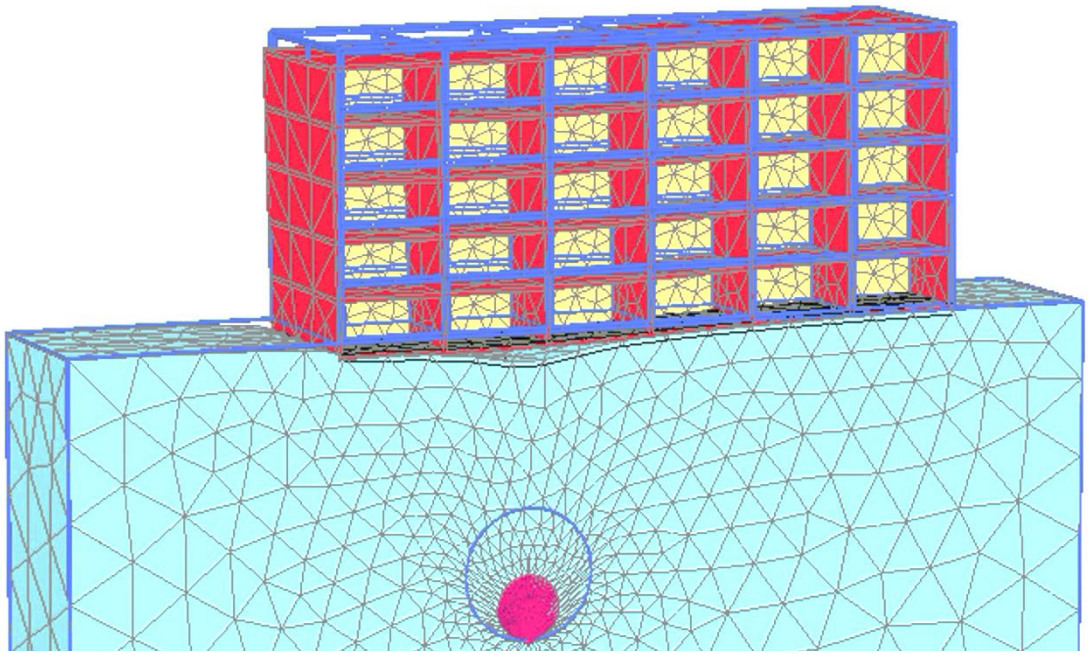

(a)

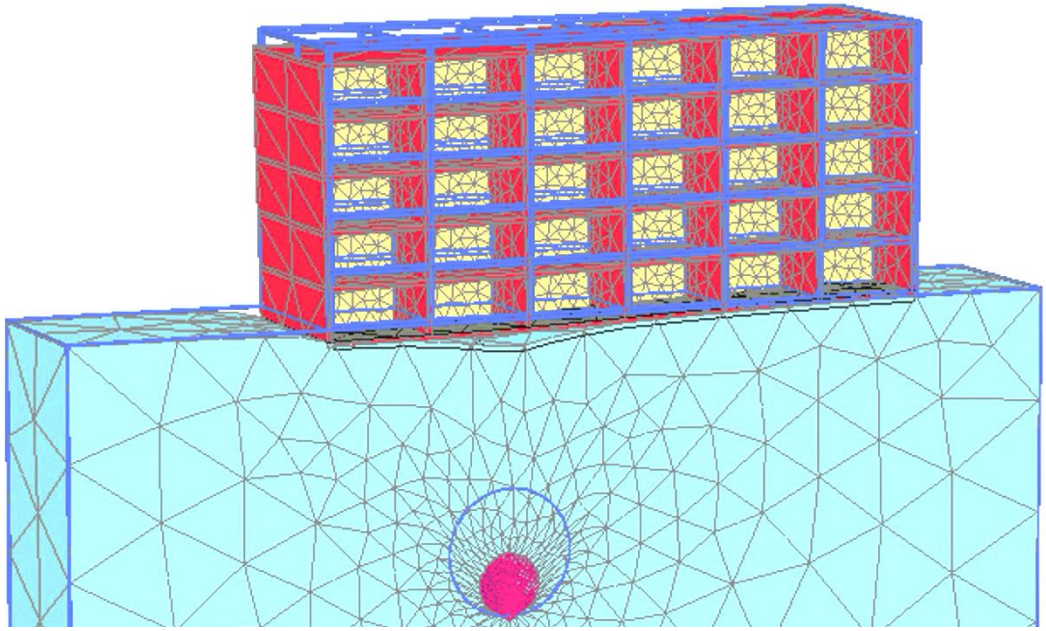

(b)

Figure 6.13. Comparison between deformed configurations (scaled up 100 times) for a) **5Se02L_Flex** b) **5Se02L_Stiff** models in PLAXIS 3D ($\boldsymbol{V_{l,t} = 1.0}$%).

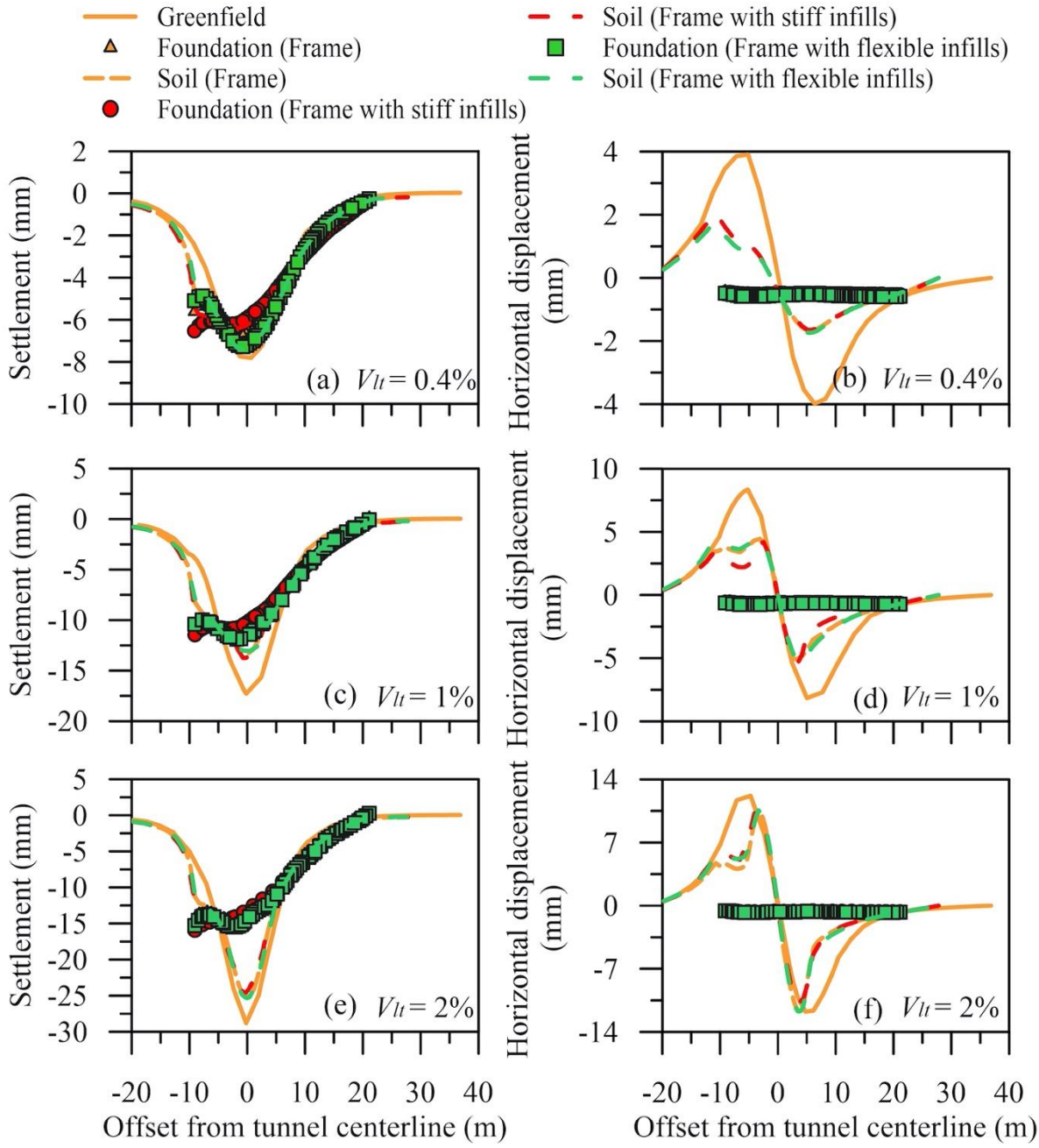

Figure 6.14. Comparison between numerical predictions for models **5Se02L_Bare**, **5Se02L _Flex**, and **5Se02L _Stiff** ($V_{l,t}$ = **0.4%, 1.0%, and 2.0%**).

Vertical and horizontal displacements calculated in both models 5Se02L and 2Se02L have almost the same trends (shown in Figure 6.8 and Figure 6.14). A comparison between these two data indicates that an increase in the number of storeys (that increase both weight and stiffness) decreased the gap size at the soil-structure interaction but the increase in stiffness only (as when adding the stiff infills) clearly increased the gap size. Also, stiffening the

structures decreases settlement of the soil beneath the frame. Moreover, the 5-storey structure is embedded in the surface on the left edge of the foundation due to the movement of the frame to the left.

6.2.5 Numerical model: 5Se05L

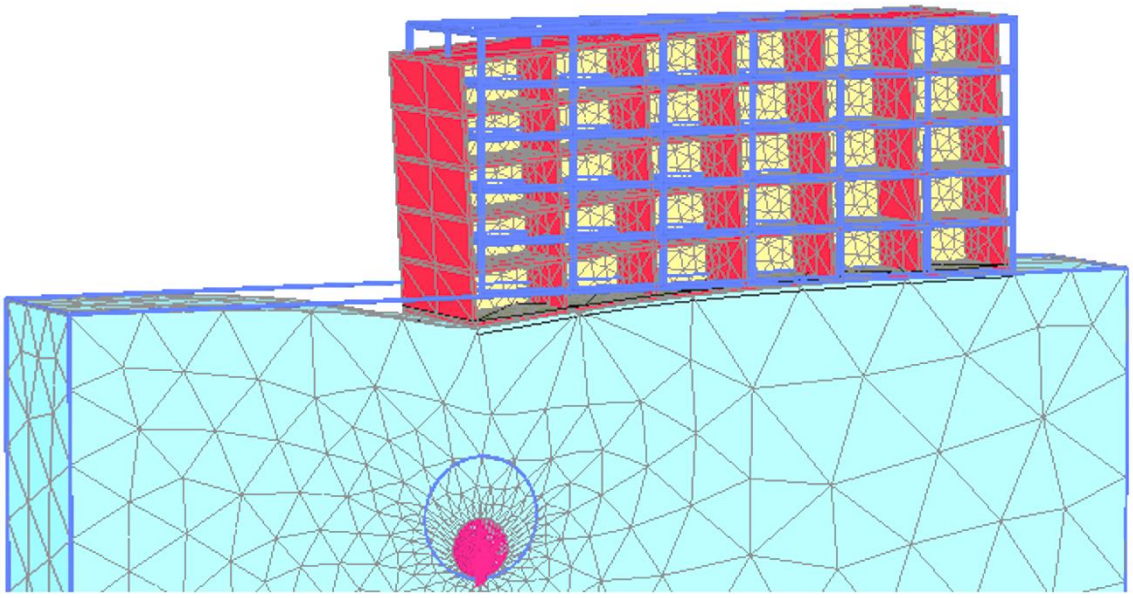

(a)

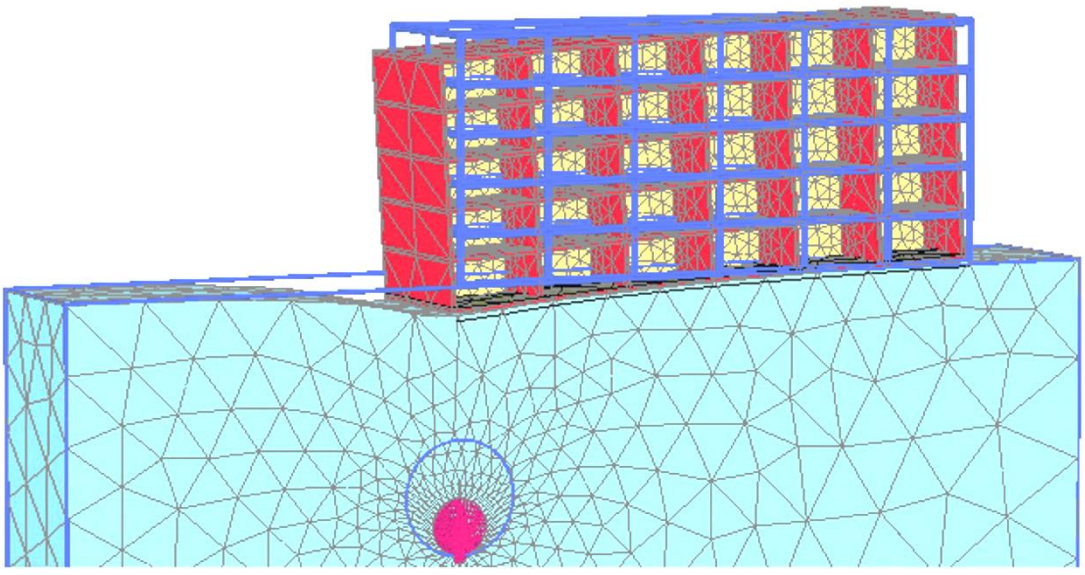

(b)

Figure 6.15. Comparison between deformed configurations (scaled up 100 times) for a) **5Se05L_Flex** b) **5Se05L_Stiff** models in PLAXIS 3D ($\boldsymbol{V_{l,t} = 1.0}$%).

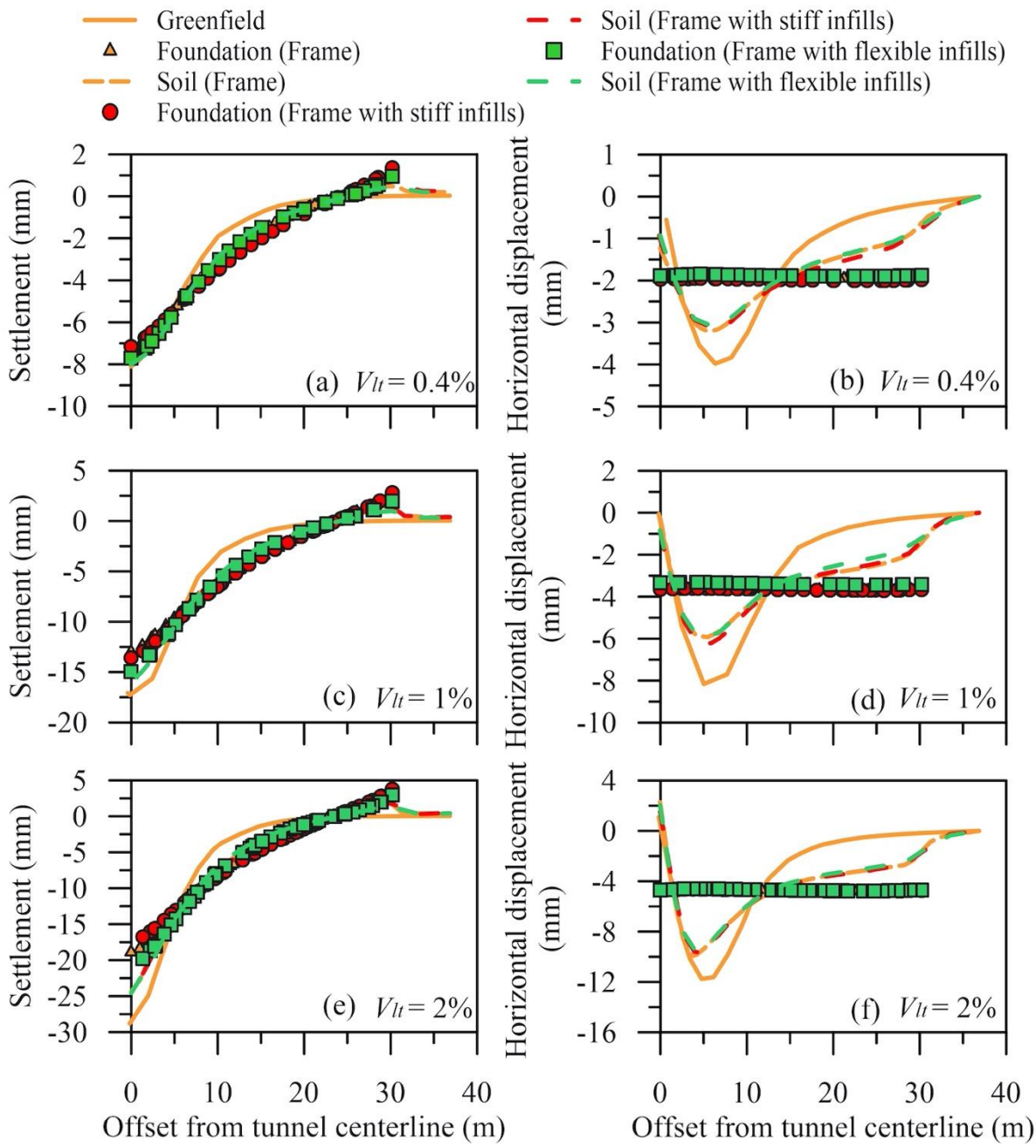

Figure 6.16. Comparison between numerical predictions for models **5Se05L_Bare**, **5Se05L _Flex**, and **5Se05L _Stiff** ($V_{l,t}$ = 0.4%, 1.0%, and 2.0%).

The trends of vertical and horizontal displacements for the model 5Se05L are roughly similar to those of the model 2Se05L with only slight differences. Indeed, stiffening the structure decreases the gap beneath the left edge of the foundation and increases the upward movements of the right edge of the foundation. Also, horizontal displacements of foundations for framed buildings experienced larger values for 5-storey buildings in comparison with 2-storey buildings.

6.2.6 Numerical model: 5Se05S

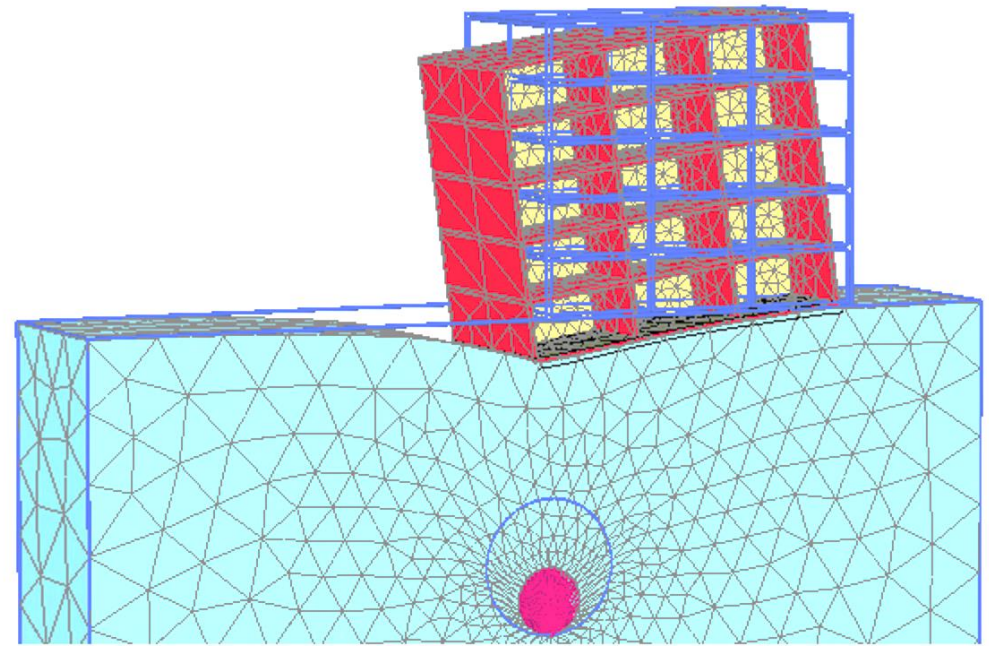

(a)

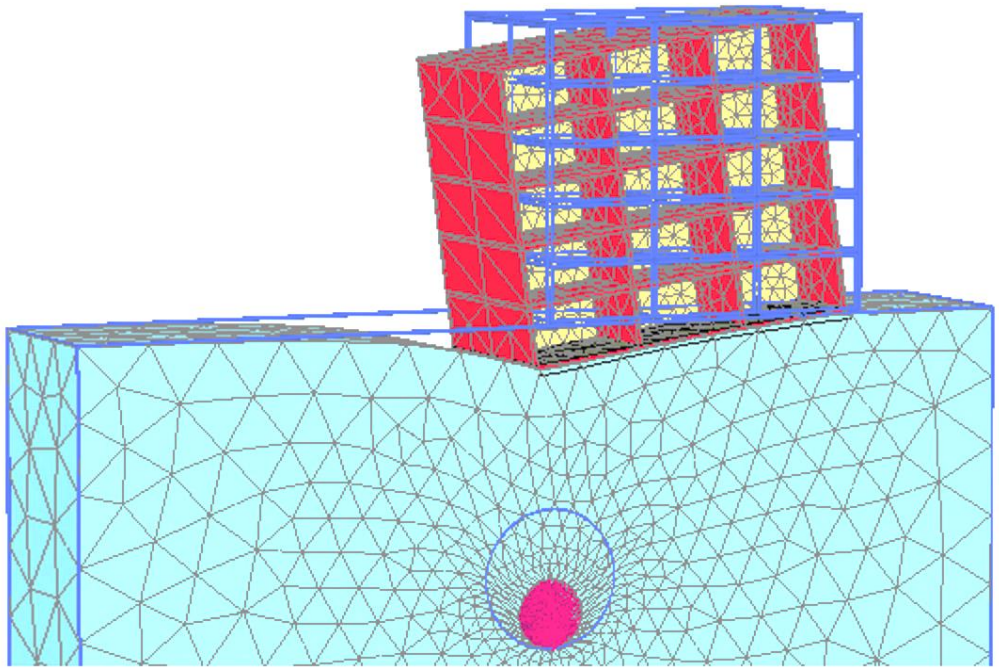

(b)

Figure 6.17. Comparison between deformed configurations (scaled up 100 times) for a) **5Se05S_Flex** b) **5Se05S_Stiff** models in PLAXIS 3D ($\boldsymbol{V_{l,t} = 1.0}$%).

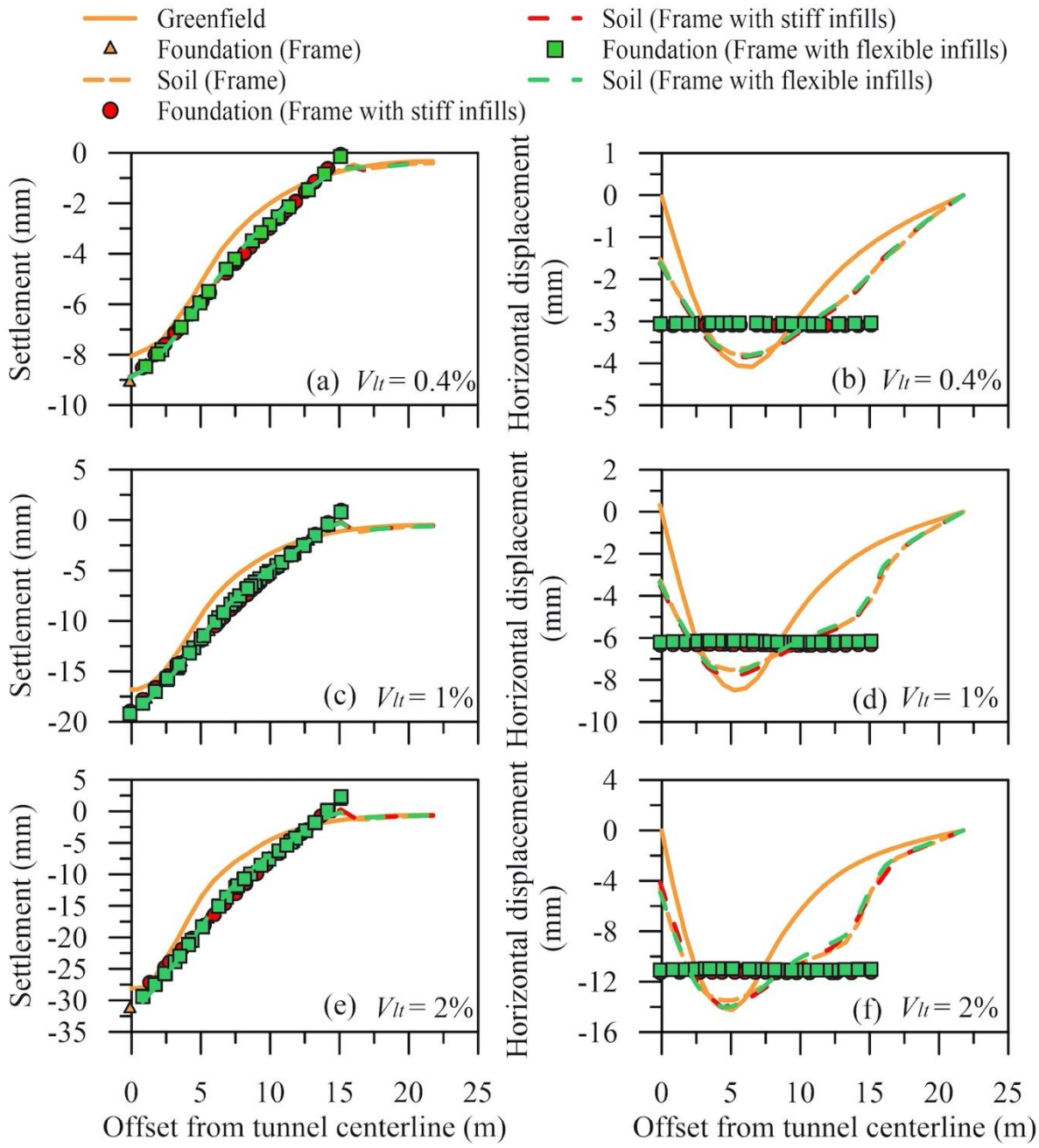

Figure 6.18. Comparison between numerical predictions for models **5Se05S_Bare**, **5Se05S _Flex**, and **5Se05S _Stiff** ($V_{l,t}$ = 0.4%, 1.0%, and 2.0%).

The vertical and horizontal displacements of model 5Se05S are coincident with those of the model 2Se05S. By considering the frame as a cantilever beam, comparison between Figure 6.18 and Figure 6.16 indicates that increasing the length of the frame produces enough support, leading to a reduction in settlements and movements at the other end of the frame positioned above the tunnelling. Accordingly, the results for long and short frames display that the height of the structure has negligible effects on the reduction of settlements. Besides, short frames experienced the largest values on horizontal movements at the foundation in comparison to

long frames. As it is shown in the deformed configurations, the eccentric (short) frames can tilt to accommodate ground settlements, while the centred frames not.

6.3 Evaluation of deformation and damage parameters

The effects of the frame stiffness and infills on the building deformations (i.e. angular distortions and maximum tensile strains) were estimated to evaluate the intensity of damage within the panels. In this study, the angular distortion and maximum tensile strains were determined for different bays in frame structures. The angular distortion (β) is the shearing distortion of the bay that was defined in detail in chapter 2. According to Eq. 2.24, the angular distortion was computed based on the tilt and slope of each bay. In centred buildings, the average angular distortion (β) of each bay was computed from foundation settlements assuming no tilt (Son and Cording, 2005). Because of the centred position of the tunnel beneath the structure and the presence of axially stiff floors, the angular distortion (β) of each bay is given by the slope computed from the bay edges (i.e. the beta value is the ratio between the differential settlement and the bay length). In eccentric buildings, the angular distortion (β) is estimated by subtracting the tilt from the slope using the top and bottom corner displacements of each bay.

The other damage parameter considered later is the maximum tensile strain (ε_t) of each infill panels. Tensile strains are estimated with two approaches: 1) directly inferred from the solid finite elements, 2) from the angular distortion using the expression $\alpha \times \beta/2$, which was modified from Son and Cording (2005) by introducing the coefficient $\alpha = 2$ proposed by Boone (1996) to account for the slab-to-column fixity at the edges. Tensile strain distributions were used to evaluate the efficiency of the second (approximated) approach (using β in estimating the tensile strains).

The calculated angular distortion of bays for all models are plotted in Figure 6.19, Figure 6.21, Figure 6.23, Figure 6.25, Figure 6.27, Figure 6.29, Figure 6.31, and Figure 6.33. As expected, results for the bare frame and the frame with flexible infills are similar in all models. In addition, maximum tensile strains inferred from angular distortions and from panels in numerical modelling of PLAXIS are plotted in Figure 6.20, Figure 6.22, Figure 6.24, Figure 6.26, Figure 6.28, Figure 6.30, Figure 6.32, and Figure 6.34. Also, the contours for maximum tensile strain distribution of panels are exported from PLAXIS in section 6.4 to examine the

level of damage based on limiting tensile strains. Indeed, to assess the distortion level of panels, indicators are used for the range of angular distortions and the category of damage.

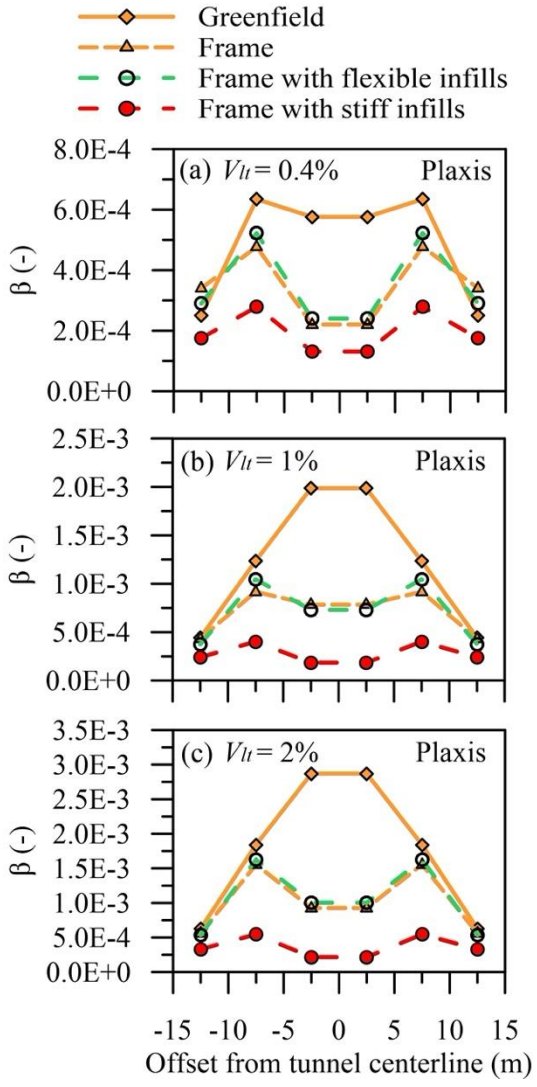

Figure 6.19. Angular distortion of bays for model **2Se0L** ($\boldsymbol{V_{l,t} = 0.4\%,\ 1.0\%,\ \text{and } 2.0\%}$).

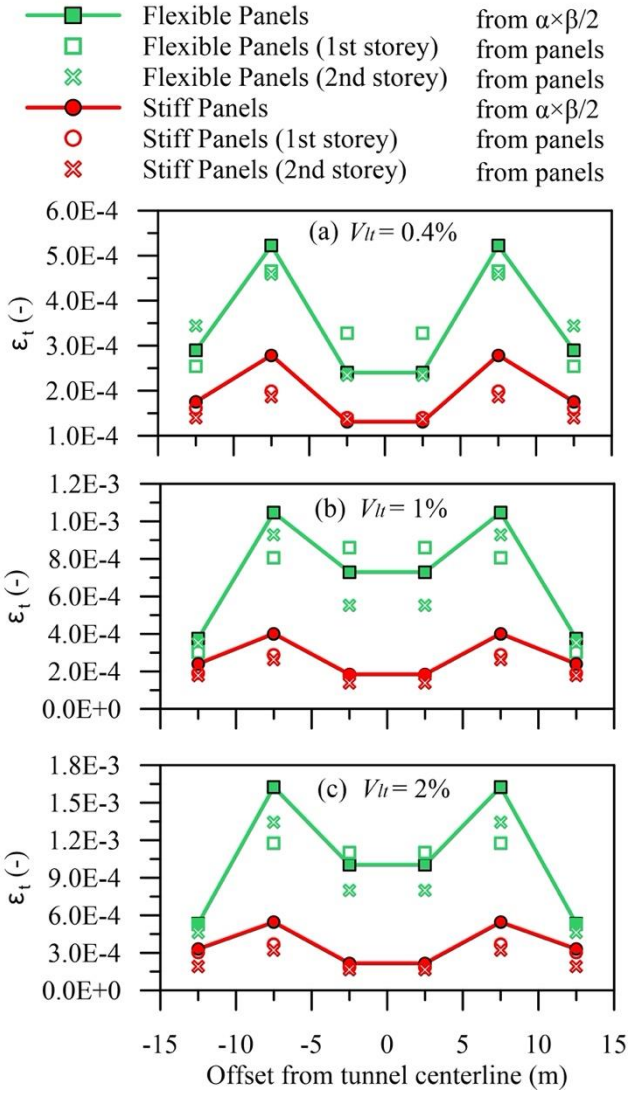

Figure 6.20. Maximum tensile strains inferred from angular distortions and from panels for model **2Se0L** ($\boldsymbol{V_{l,t} = 0.4\%,\ 1.0\%,\ \text{and } 2.0\%}$).

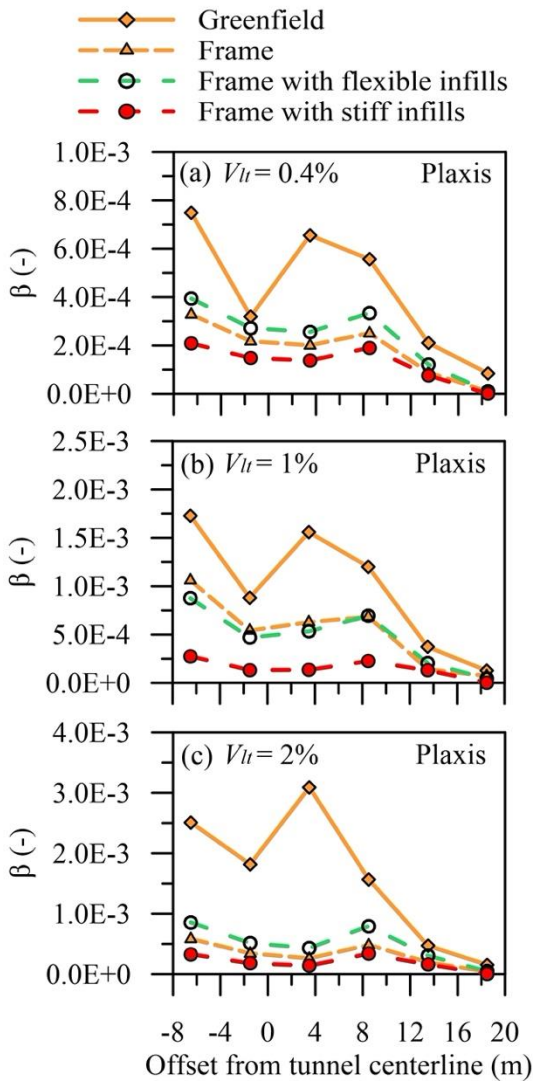

Figure 6.21. Angular distortion of bays for model **2Se02L** ($\boldsymbol{V_{l,t} = 0.4\%,\ 1.0\%,\ \text{and } 2.0\%}$).

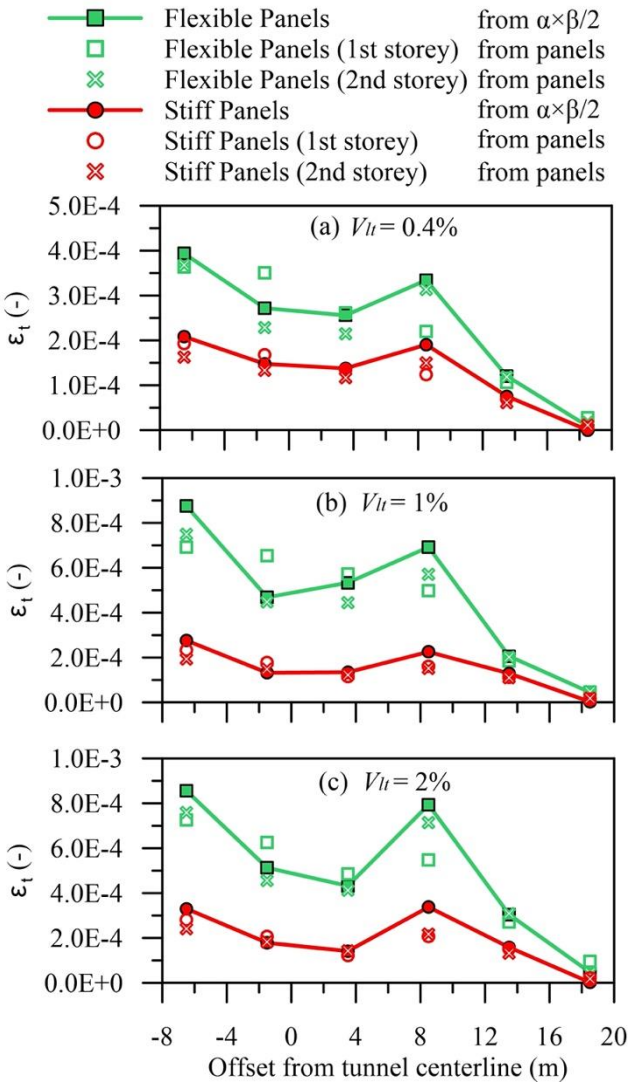

Figure 6.22. Maximum tensile strains inferred from angular distortions and from panels for model **2Se02L** ($\boldsymbol{V_{l,t} = 0.4\%,\ 1.0\%,\ \text{and } 2.0\%}$).

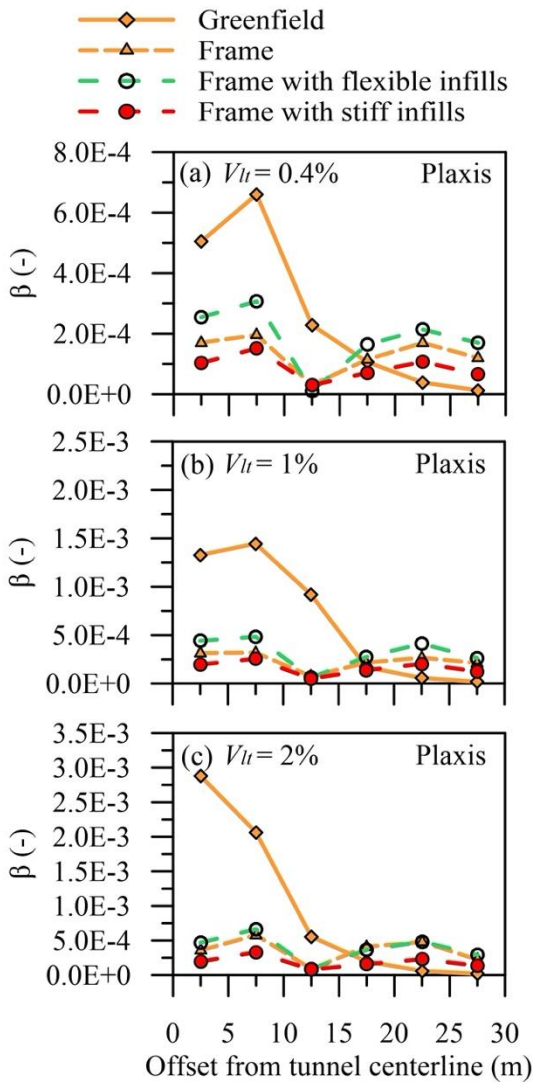

Figure 6.23. Angular distortion of bays for model **2Se05L** ($\boldsymbol{V_{l,t} = 0.4\%,\ 1.0\%,\ \text{and } 2.0\%}$).

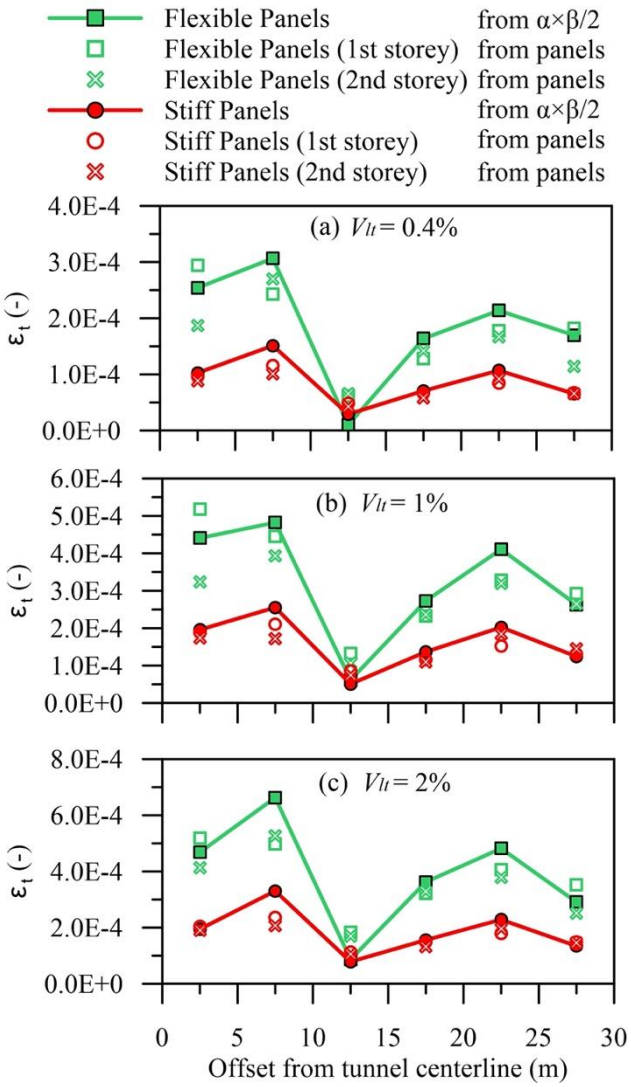

Figure 6.24. Maximum tensile strains inferred from angular distortions and from panels for model **2Se05L** ($\boldsymbol{V_{l,t} = 0.4\%,\ 1.0\%,\ \text{and } 2.0\%}$).

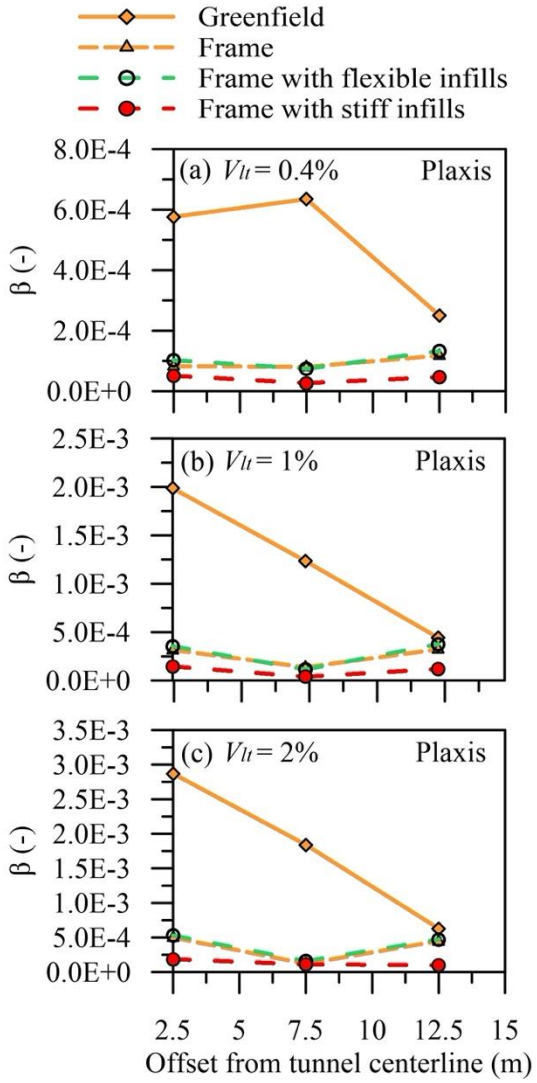

Figure 6.25. Angular distortion of bays for model **2Se05S** ($\boldsymbol{V_{l,t} = 0.4\%,\ 1.0\%,\ \text{and } 2.0\%}$).

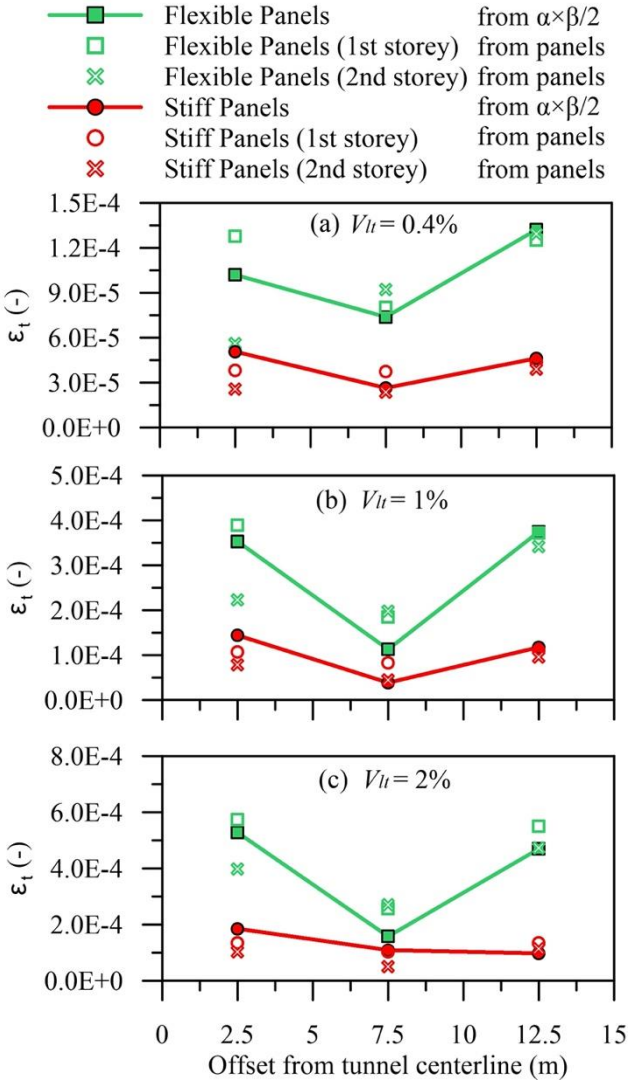

Figure 6.26. Maximum tensile strains inferred from angular distortions and from panels for model **2Se05S** ($\boldsymbol{V_{l,t} = 0.4\%,\ 1.0\%,\ \text{and } 2.0\%}$).

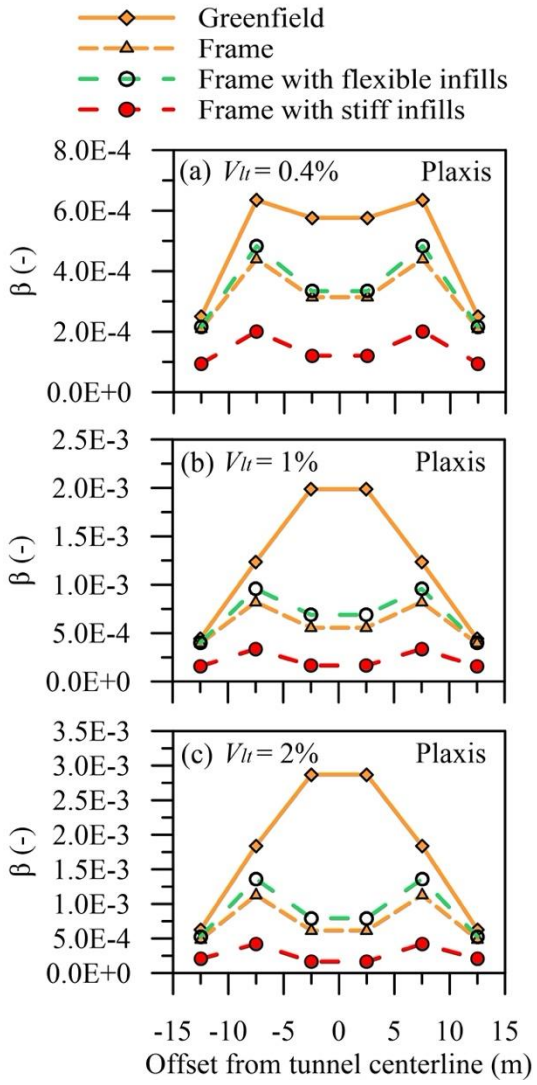

Figure 6.27. Angular distortion of bays for model **5Se0L** ($\boldsymbol{V_{l,t} = 0.4\%,\ 1.0\%,\ \text{and } 2.0\%}$).

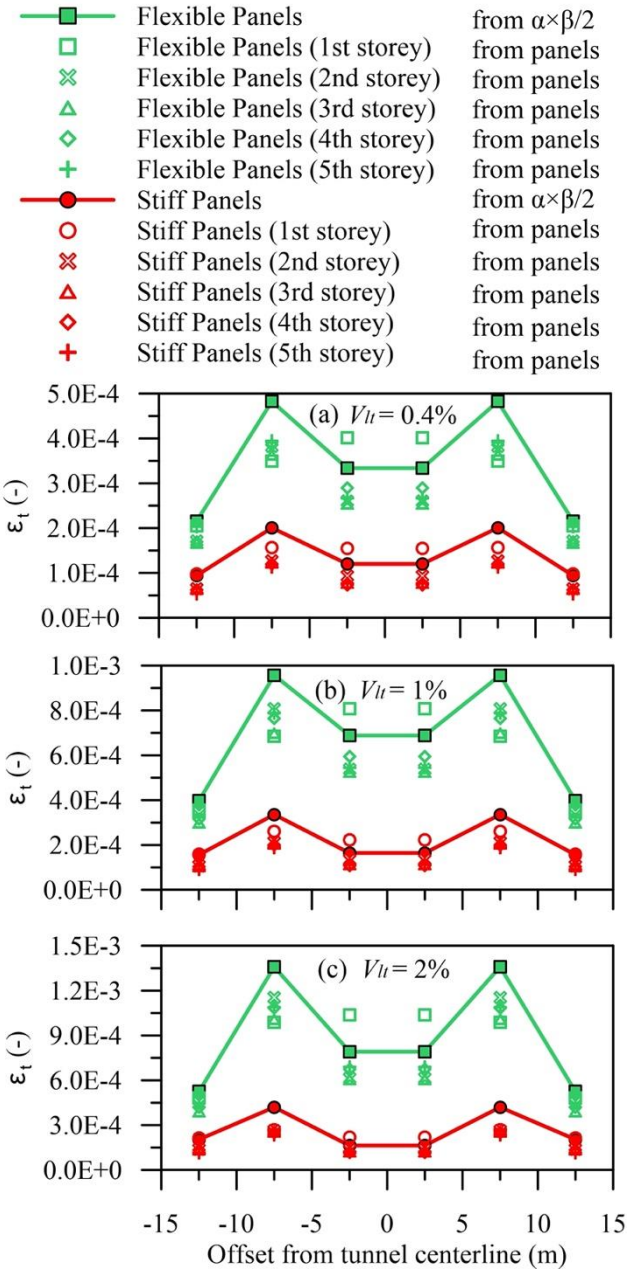

Figure 6.28. Maximum tensile strains inferred from angular distortions and from panels for model **5Se0L** ($\boldsymbol{V_{l,t} = 0.4\%,\ 1.0\%,\ \text{and } 2.0\%}$).

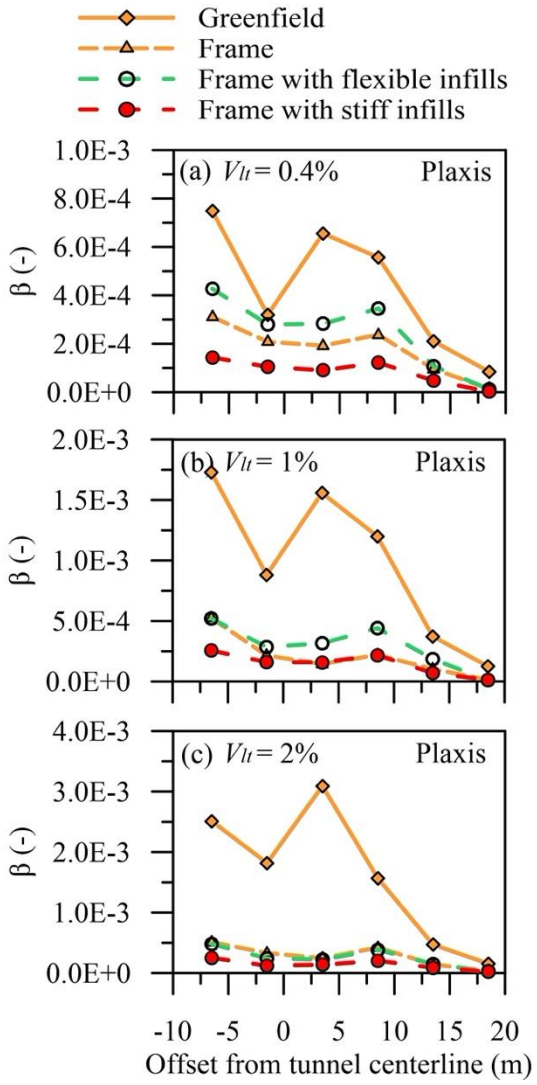

Figure 6.29. Angular distortion of bays for model **5Se02L** ($\boldsymbol{V_{l,t} = 0.4\%,\ 1.0\%,\ \text{and } 2.0\%}$).

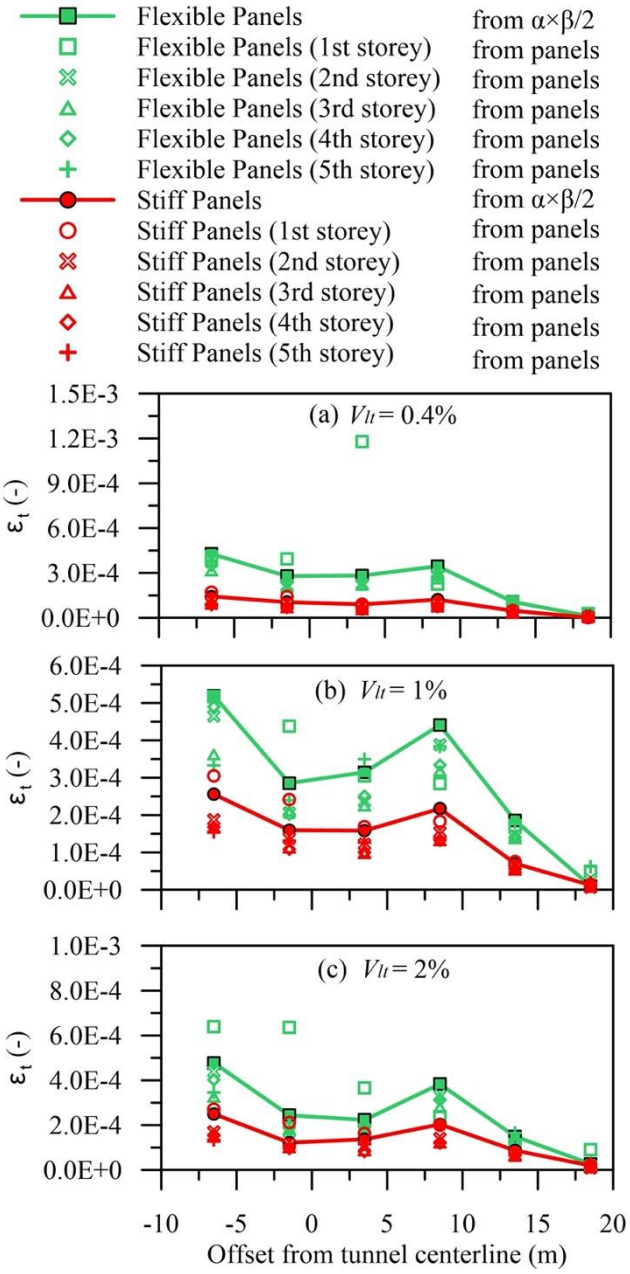

Figure 6.30. Maximum tensile strains inferred from angular distortions and from panels for model **5Se02L** ($\boldsymbol{V_{l,t} = 0.4\%,\ 1.0\%,\ \text{and } 2.0\%}$).

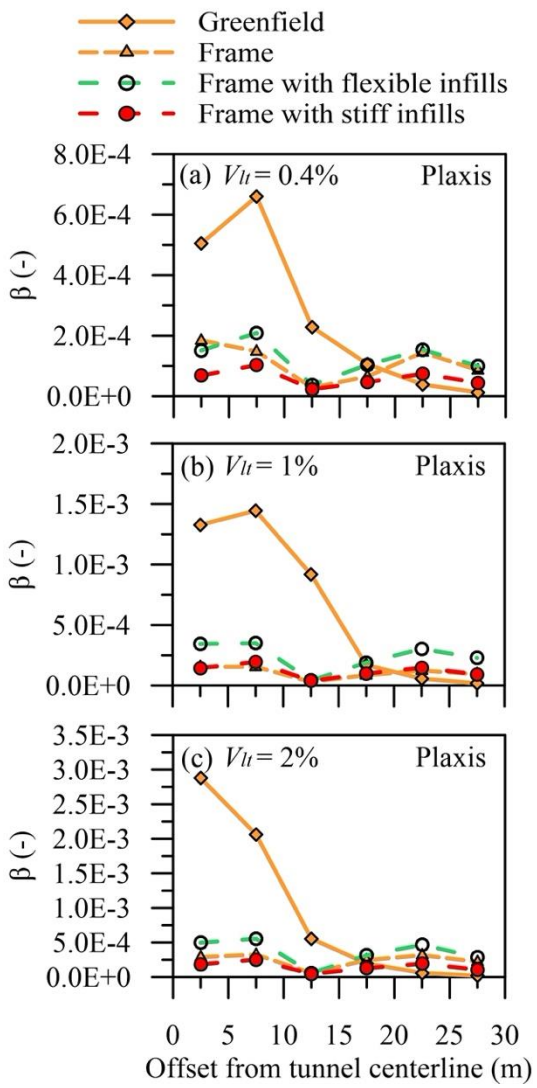

Figure 6.31. Angular distortion of bays for model **5Se05L** ($\boldsymbol{V_{l,t} = 0.4\%,\ 1.0\%,\ \text{and } 2.0\%}$).

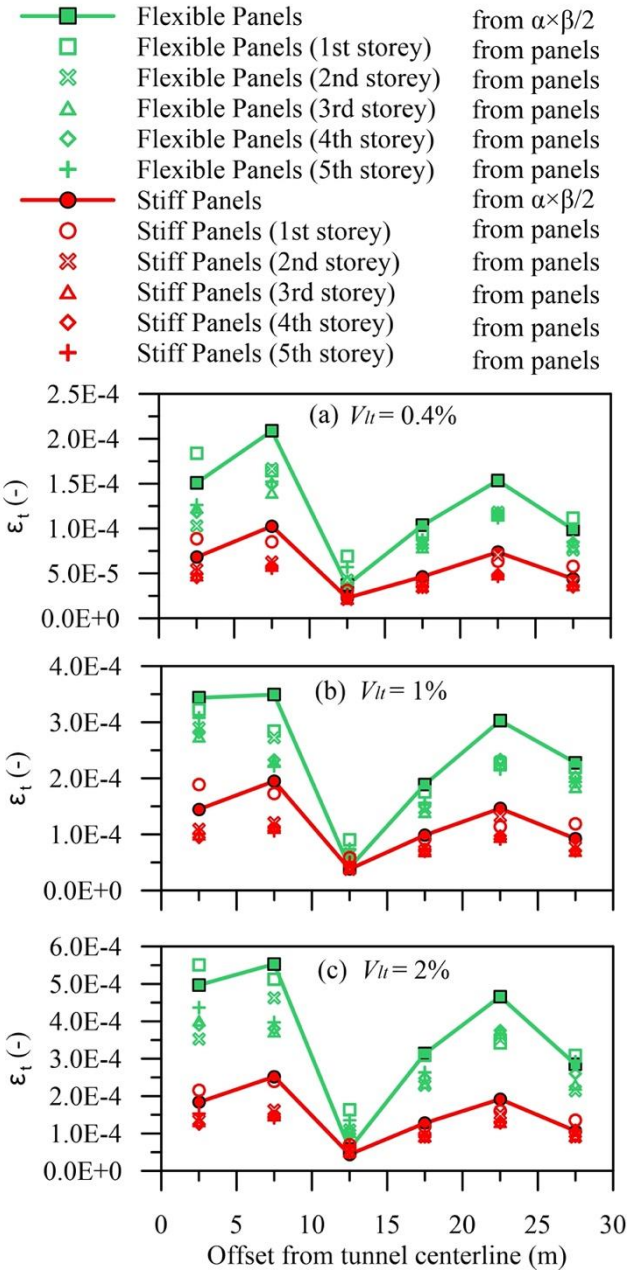

Figure 6.32. Maximum tensile strains inferred from angular distortions and from panels for model **5Se05L** ($\boldsymbol{V_{l,t} = 0.4\%,\ 1.0\%,\ \text{and } 2.0\%}$).

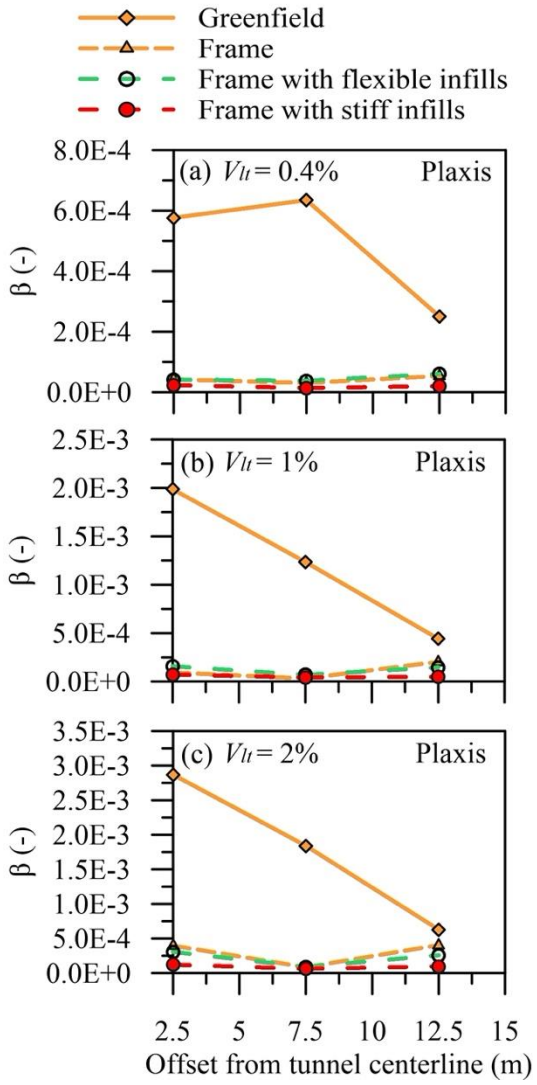

Figure 6.33. Angular distortion of bays for model **5Se05S** ($\boldsymbol{V_{l,t} = 0.4\%,\ 1.0\%,\ \text{and } 2.0\%}$).

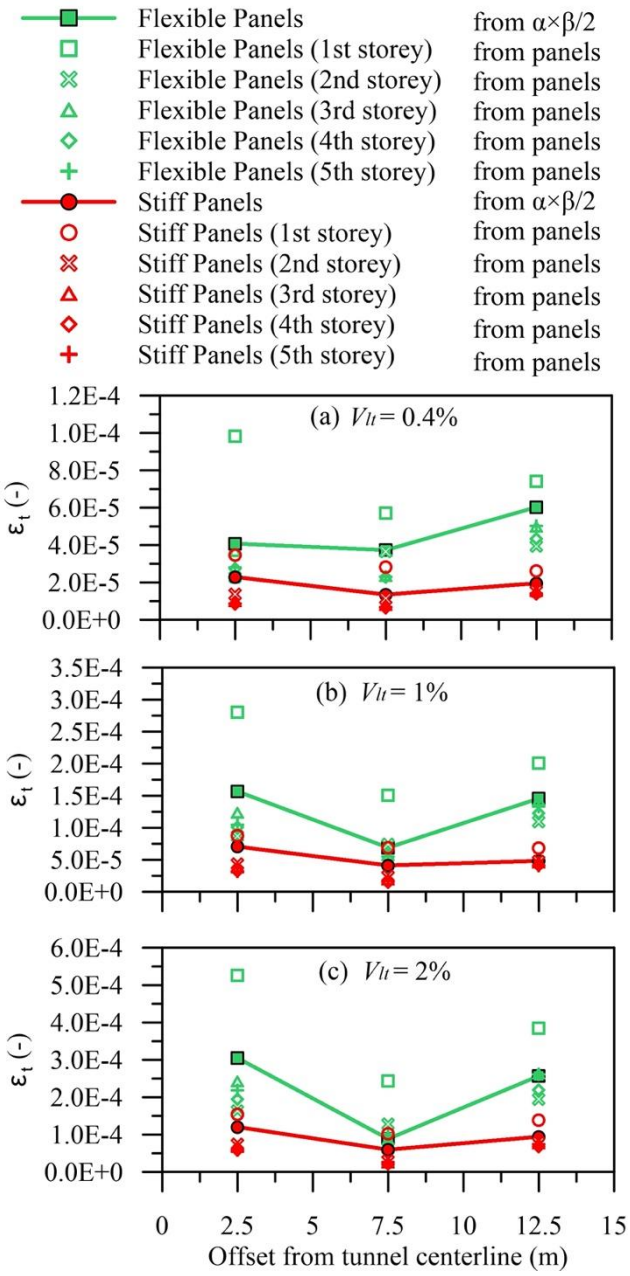

Figure 6.34. Maximum tensile strains inferred from angular distortions and from panels for model **5Se05S** ($\boldsymbol{V_{l,t} = 0.4\%,\ 1.0\%,\ \text{and } 2.0\%}$).

Figure 6.19 and Figure 6.27 display angular distortions induced within the bays for centred-long frames 2Se0L and 5Se0L. The bare frame stiffness decreased the distortions of the central bays above the tunnel with respect to the greenfield case, resulting in approximately halved maximum values of β. This was due to the frame stiffness, which prevented further settlements at the centreline to be transmitted from the ground to the structure (Franza et al., 2020). On the

other hand, the presence of stiff infills reduced the building distortions to an approximately uniform value, similar to the greenfield angular distortion of the external bays.

On the contrary, the angular distortion for the eccentric-long frames 2Se02L, 2Se05L, 5Se02L, and 5Se05L show that the increase in building stiffness (due to additional storeys or stiff infill panels) decreased the angular distortion. It seems that the formation of a gap leads to a decrease in the forces transmitted by the soil to the structure and, thus, a reduction in the level of structural distortions.

Furthermore, the short frames 2Se05S and 5Se05S, which can be regarded as half of the long frame, experienced the smallest angular distortion for all tunnel volume losses. A comparison among the angular distortions in all of these cases indicates that the maximum angular distortion of bays occurred in centred-long frames with 2-storey buildings.

Eventually, results show that the maximum tensile strains inferred from angular distortions are slightly higher than those estimated directly from the panels in all models. As such, it can be considered a conservative approach.

6.4 Level of damage based on limiting tensile strains

To quantify the deformation levels of bays and panels across the frames, the contours of tensile strains were plotted by considering the categories of damage obtained from the thresholds of Boscardin and Cording (1989). Based on these categories, negligible (CAT.1), very slight (CAT.2), and slight (CAT.3) damage classes were related to 0.05%, 0.075%, and 0.15% of tensile strain limits, respectively (see the legend scale in the figures below).

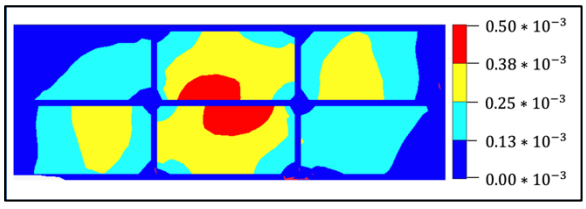

(a) Flexible panels ($V_{l,t} = 0.4\%$)- CAT.1

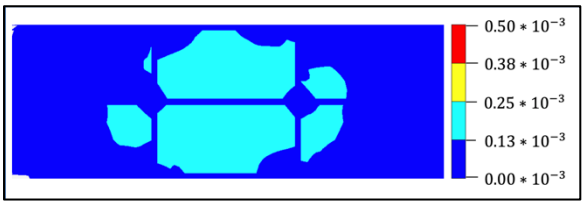

(b) Stiff panels ($V_{l,t} = 0.4\%$)- CAT.1

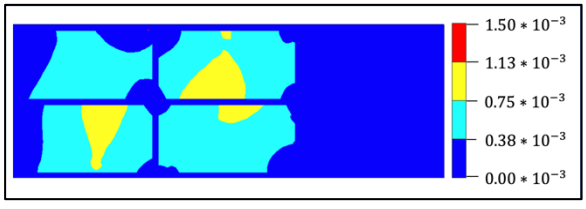

(c) Flexible panels ($V_{l,t} = 1.0\%$)- CAT.3

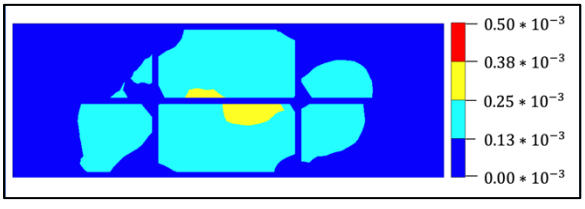

(d) Stiff panels ($V_{l,t} = 1.0\%$)- CAT.1

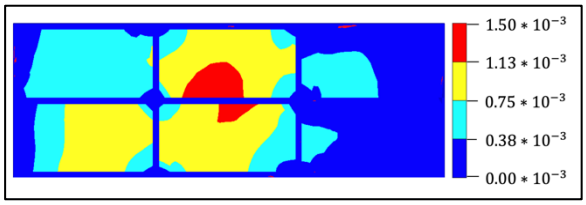

(e) Flexible panels ($V_{l,t} = 2.0\%$)- CAT.3

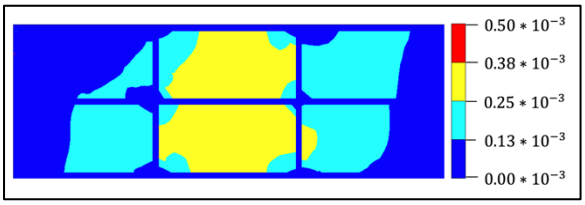

(f) Stiff panels ($V_{l,t} = 2.0\%$)- CAT.1

Figure 6.35. Maximum tensile strains of panels for model **2Se0L**.

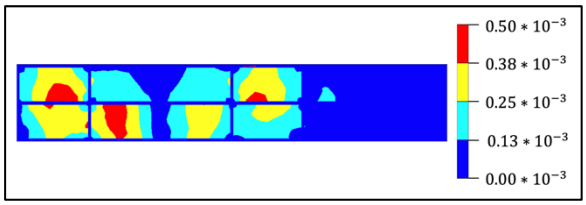

(a) Flexible panels ($V_{l,t} = 0.4\%$)- CAT.1

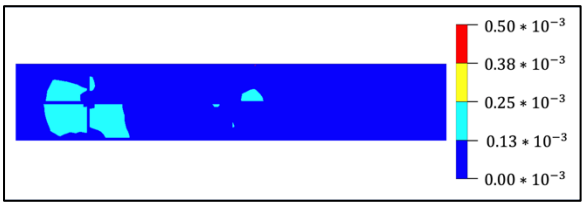

(b) Stiff panels ($V_{l,t} = 0.4\%$)- CAT.1

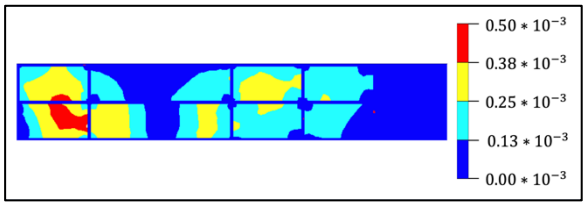

(c) Flexible panels ($V_{l,t} = 1.0\%$)- CAT.1

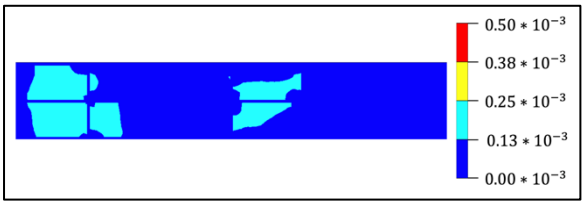

(d) Stiff panels ($V_{l,t} = 1.0\%$)- CAT.1

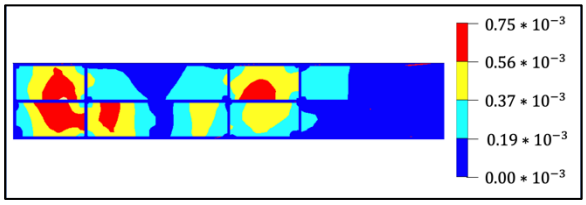

(e) Flexible panels ($V_{l,t} = 2.0\%$)- CAT.2

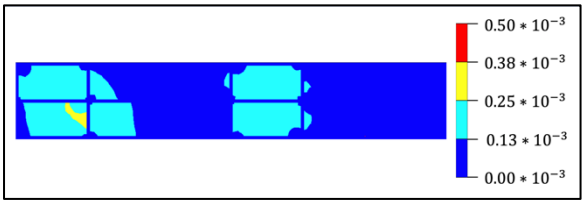

(f) Stiff panels ($V_{l,t} = 2.0\%$)- CAT.1

Figure 6.36. Maximum tensile strains of panels for model **2Se02L**.

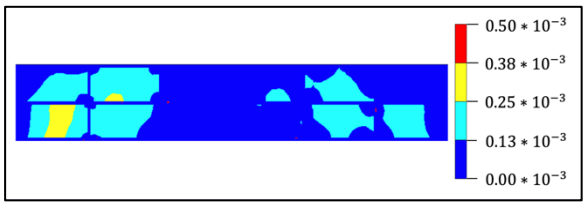

(a) Flexible panels ($V_{l,t} = 0.4\%$)- CAT.1

(b) Stiff panels ($V_{l,t} = 0.4\%$)- CAT.1

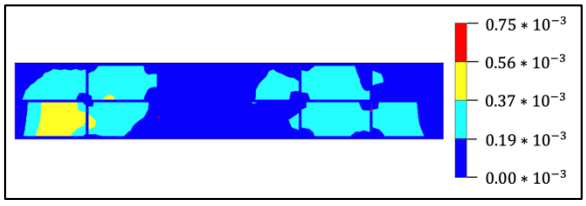

(c) Flexible panels ($V_{l,t} = 1.0\%$)- CAT.2 (d) Stiff panels ($V_{l,t} = 1.0\%$)- CAT.1

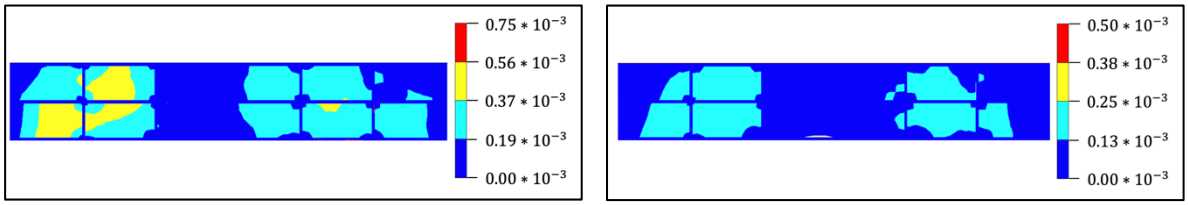

(e) Flexible panels ($V_{l,t} = 2.0\%$)- CAT.2 (f) Stiff panels ($V_{l,t} = 2.0\%$)- CAT.1

Figure 6.37. Maximum tensile strains of panels for model **2Se05L**.

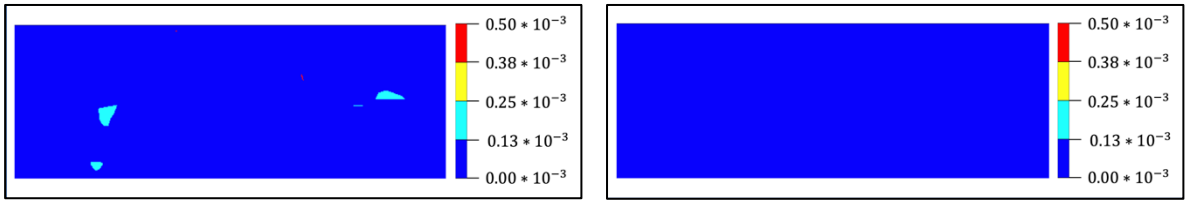

(a) Flexible panels ($V_{l,t} = 0.4\%$)- CAT.1 (b) Stiff panels ($V_{l,t} = 0.4\%$)- CAT.1

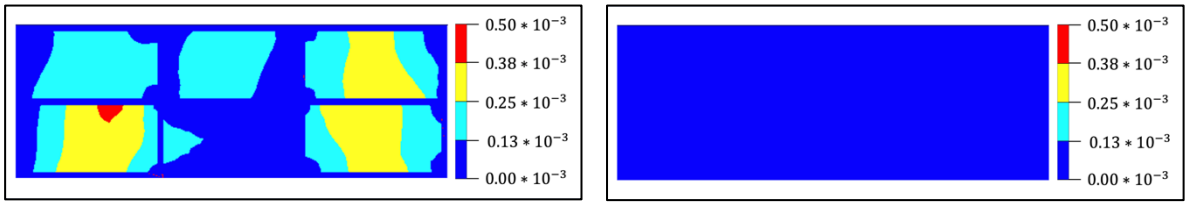

(c) Flexible panels ($V_{l,t} = 1.0\%$)- CAT.1 (d) Stiff panels ($V_{l,t} = 1.0\%$)- CAT.1

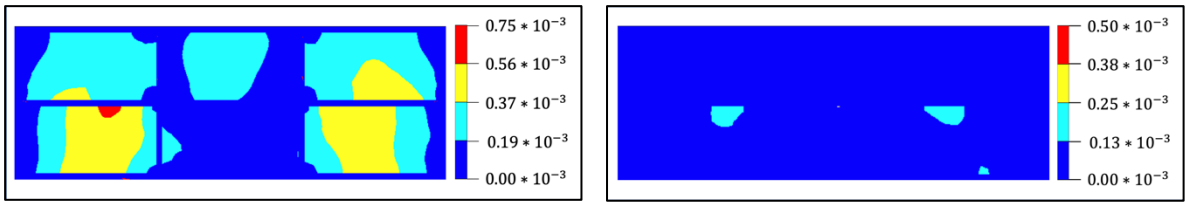

(e) Flexible panels ($V_{l,t} = 2.0\%$)- CAT.2 (f) Stiff panels ($V_{l,t} = 2.0\%$)- CAT.1

Figure 6.38. Maximum tensile strains of panels for model **2Se05S**.

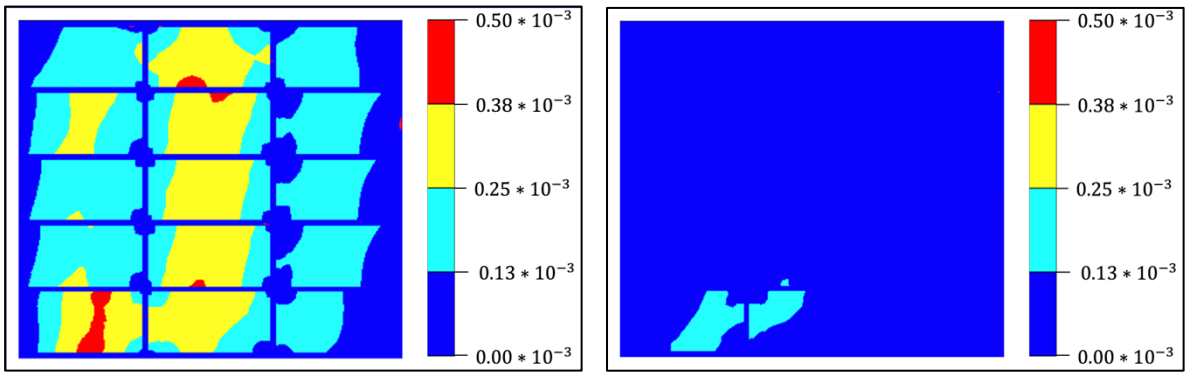

(a) Flexible panels ($V_{l,t} = 0.4\%$)- CAT.1

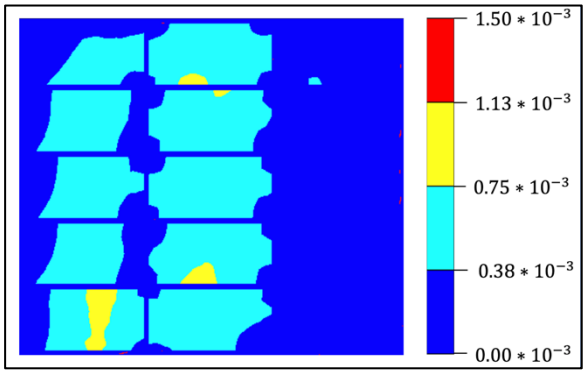

(b) Stiff panels ($V_{l,t} = 0.4\%$)- CAT.1

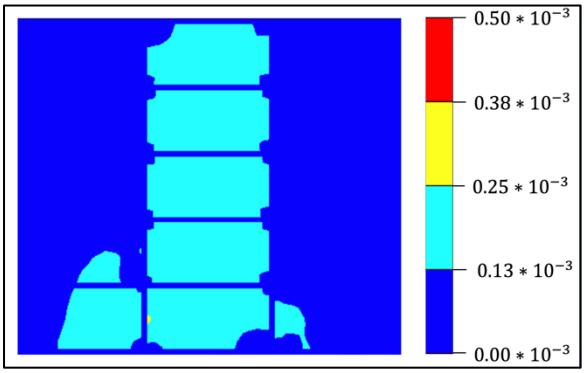

(c) Flexible panels ($V_{l,t} = 1.0\%$)- CAT.3

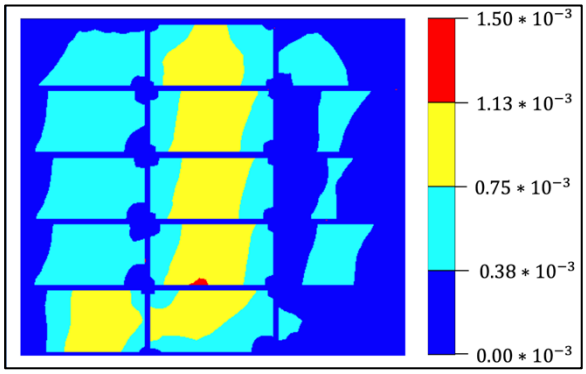

(d) Stiff panels ($V_{l,t} = 1.0\%$)- CAT.1

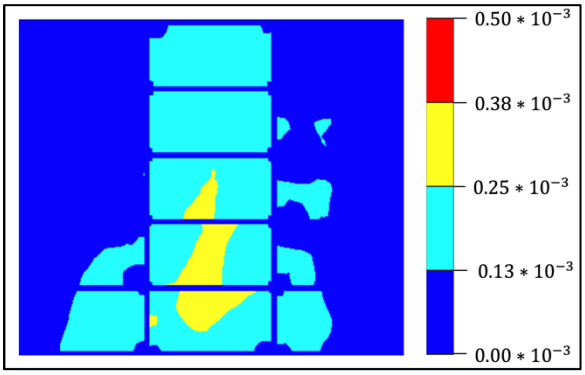

(e) Flexible panels ($V_{l,t} = 2.0\%$)- CAT.3

(f) Stiff panels ($V_{l,t} = 2.0\%$)- CAT.1

Figure 6.39. Maximum tensile strains of panels for model **5Se0L**.

(a) Flexible panels ($V_{l,t} = 0.4\%$)- CAT.2

(b) Stiff panels ($V_{l,t} = 0.4\%$)- CAT.1

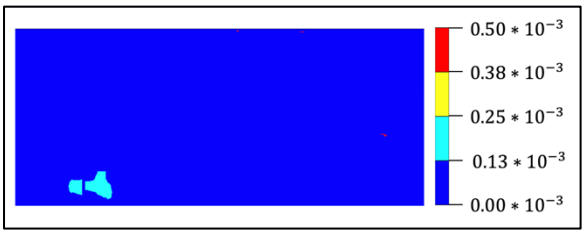

(c) Flexible panels ($V_{l,t} = 1.0\%$)- CAT.2

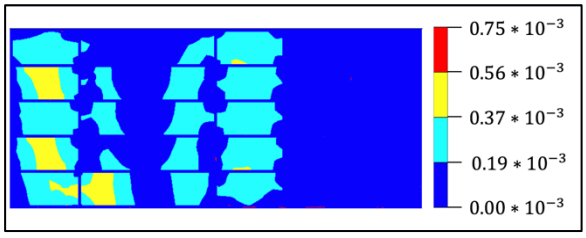

(d) Stiff panels ($V_{l,t} = 1.0\%$)- CAT.1

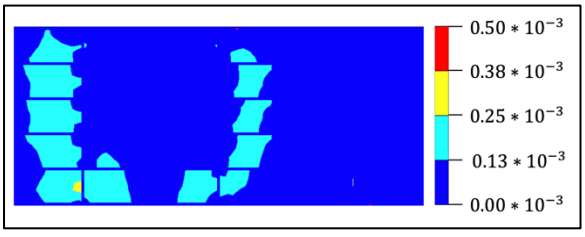

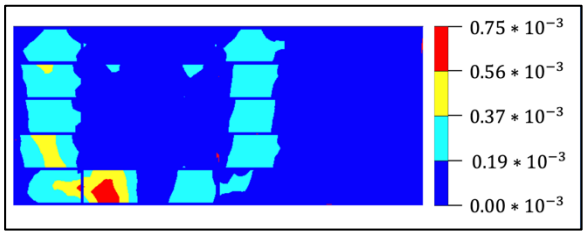

(e) Flexible panels ($V_{l,t} = 2.0\%$)- CAT.2

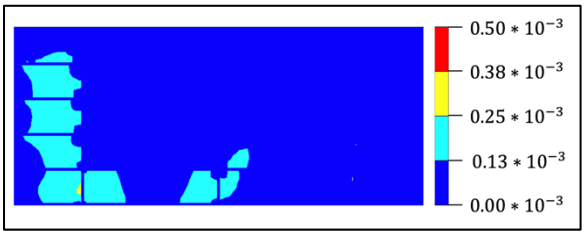

(f) Stiff panels ($V_{l,t} = 2.0\%$)- CAT.1

Figure 6.40. Maximum tensile strains of panels for model **5Se02L**.

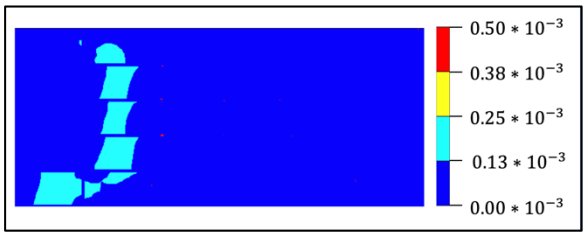

(a) Flexible panels ($V_{l,t} = 0.4\%$)- CAT.1

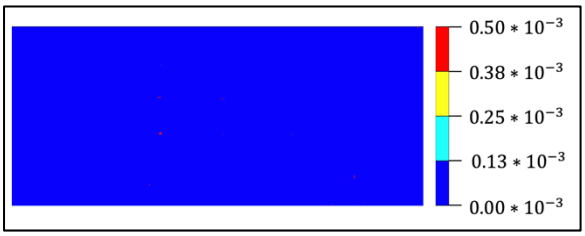

(b) Stiff panels ($V_{l,t} = 0.4\%$)- CAT.1

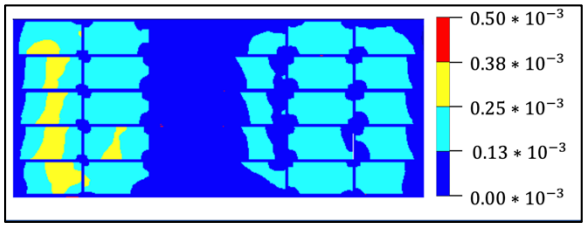

(c) Flexible panels ($V_{l,t} = 1.0\%$)- CAT.1

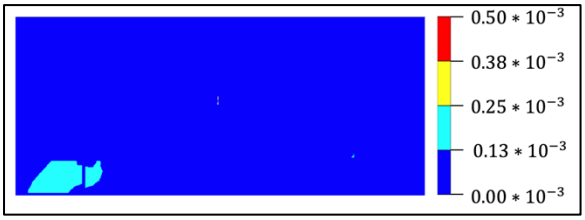

(d) Stiff panels ($V_{l,t} = 1.0\%$)- CAT.1

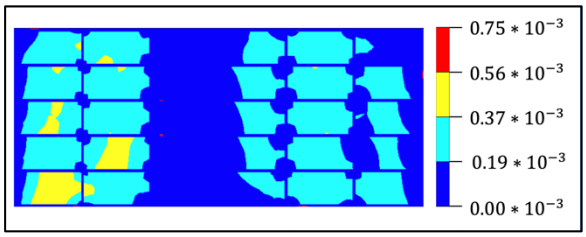

(e) Flexible panels ($V_{l,t} = 2.0\%$)- CAT.2

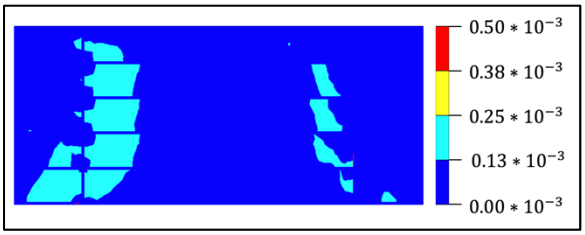

(f) Stiff panels ($V_{l,t} = 2.0\%$)- CAT.1

Figure 6.41. Maximum tensile strains of panels for model **5Se05L**.

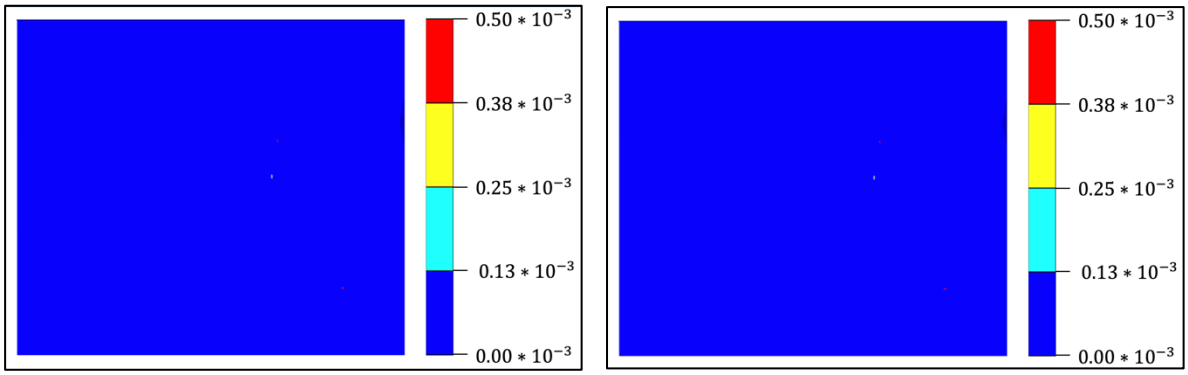

(a) Flexible panels ($V_{l,t} = 0.4\%$)- CAT.1 (b) Stiff panels ($V_{l,t} = 0.4\%$)- CAT.1

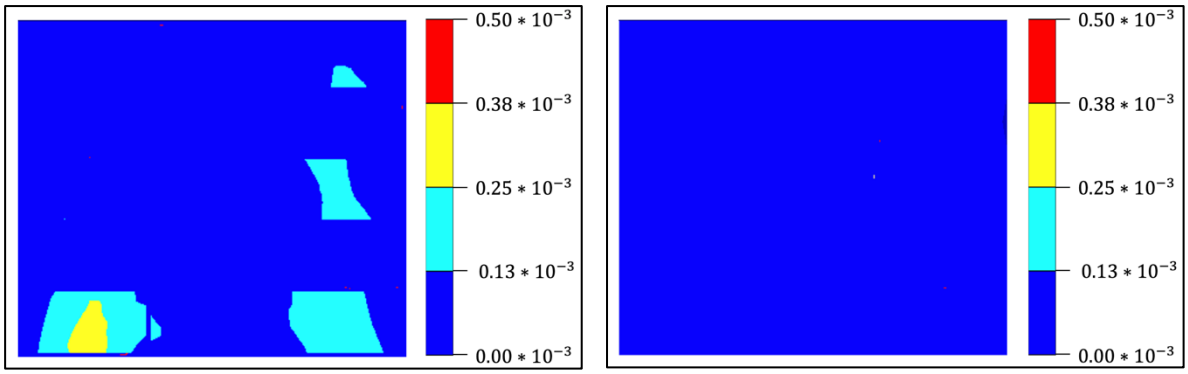

(c) Flexible panels ($V_{l,t} = 1.0\%$)- CAT.1 (d) Stiff panels ($V_{l,t} = 1.0\%$)- CAT.1

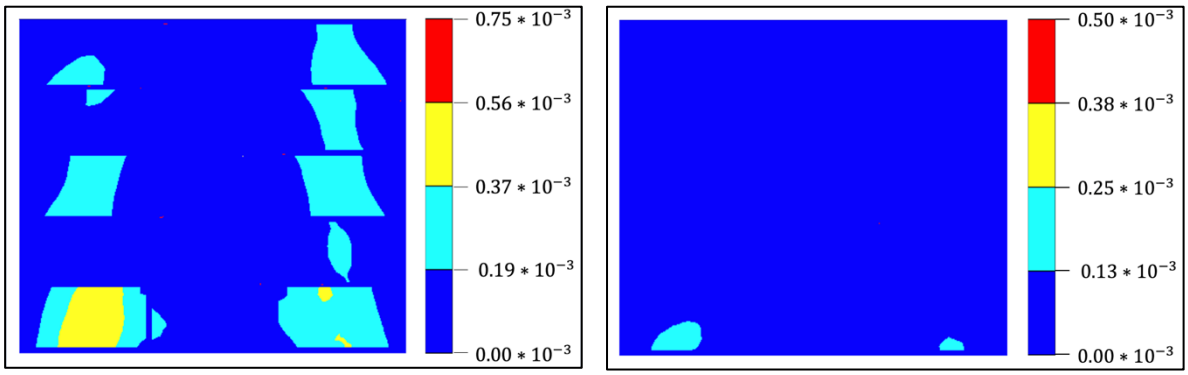

(e) Flexible panels ($V_{l,t} = 2.0\%$)- CAT.2 (f) Stiff panels ($V_{l,t} = 2.0\%$)- CAT.1

Figure 6.42. Maximum tensile strains of panels for model **5Se05S**.

The categories of damage in all cases are sorted based on the types of frame model and tunnel volume losses in Table 6-1. First, all stiff panels in all models underwent low levels of damage (CAT.1). Second, slight damages (CAT.3) was observed only in long centred structures (2-storey and 5-story buildings) for $V_{l,t} = 1.0\%$ and 2.0%. Third, the eccentric frames experienced a maximum tensile strain corresponding to CAT.2 of damage levels for the bare frames ("Flexible Panels" analysis) at different tunnel volume losses.

Table 6-1. Maximum experienced tensile strains based on categories of damage for flexible and stiff panels in all framed structures.

	$V_{l.t}$	Flexible	Stiff		$V_{l.t}$	Flexible	Stiff
2Se0L	0.4%	CAT.1	CAT.1	5Se0L	0.4%	CAT.1	CAT.1
	1.0%	CAT.3	CAT.1		1.0%	CAT.3	CAT.1
	2.0%	CAT.3	CAT.1		2.0%	CAT.3	CAT.1
2Se02L	0.4%	CAT.1	CAT.1	5Se02L	0.4%	CAT.2	CAT.1
	1.0%	CAT.1	CAT.1		1.0%	CAT.2	CAT.1
	2.0%	CAT.2	CAT.1		2.0%	CAT.2	CAT.1
2Se05L	0.4%	CAT.1	CAT.1	5Se05L	0.4%	CAT.1	CAT.1
	1.0%	CAT.2	CAT.1		1.0%	CAT.1	CAT.1
	2.0%	CAT.2	CAT.1		2.0%	CAT.2	CAT.1
2Se05S	0.4%	CAT.1	CAT.1	5Se05S	0.4%	CAT.1	CAT.1
	1.0%	CAT.1	CAT.1		1.0%	CAT.1	CAT.1
	2.0%	CAT.2	CAT.1		2.0%	CAT.2	CAT.1

When the stiffness of the panels was not considered ("Flexible Panels" analysis), the maximum tensile strains occurred in the central bays, and the assessed category of damage was CAT.1 for a tunnel volume loss of 0.4% and up to CAT.3 for 2%, in contrast to the negligible damage estimated for the "Stiff Panels" cases.

On the contrary to the number of storeys, eccentricity and stiffness of infills played the main role in determining the maximum tensile strain . As mentioned, high stiffness of infills leads to almost undamaged outcomes. By increasing the eccentricity from $e/B = 0$ to $e/B = 0.2$, the maximum tensile strain moved from the center to the side of the frame closer to the tunnel, while the level of damage in other side of the frame remained negligible. In case of $e/B = 0.5$, the pattern changes and the central bays of frames stayed in safer zones (i.e., having negligible maximum tensile strains) in comparison with the other bays.

Chapter. 7. The effects of openings in the infill walls

Assessment of the risk of building damage during tunneling requires an adequate description of the effect of structural details for the soil-structure interaction problems. Previous experimental (Farrell, 2011) and computational (Franzius et al., 2006; Goh and Mair, 2014) studies mainly focused on the impact of the overall building stiffness. However, more recent computational modelling research showed the crucial role of building details, including stress localization effects in the vicinity of wall openings (Son and Cording, 2005; Giardina et al., 2010; Pickhaver et al., 2010; Yiu et al., 2017). Pickhaver et al. (2010) used a 3D finite element analysis to estimate the influence of tunneling on an existing masonry structure with openings, and also an equivalent beam element formulation was developed to represent the behaviour of the building. Furthermore, Yiu et al. (2017) focused on the interaction between the soil and the building, and the influence of explicitly modelled window and door openings. It resulted that useful damage predictions were obtained from 3D analysis of a single facade and foundation, without the need to model a complete building. According to recent studies, there is a lack of experimental and numerical data on the effect of openings in masonry infills for frame structures.

In this chapter, the influence of structural stiffness is investigated by taking into account the presence of openings in masonry infills. As shown in Figure 7.1, the specific opening layout is simulated for the model 2Se0L, and the proportion of openings in the panel is 20% of the total surface. Each window has a dimension of $1.2\text{m} \times 0.95\text{m}$.

The deformed configurations of frames 2Se0L_Flex and 2Se0L_Stiff including openings in infills are illustrated in Figure 7.1. The deformations are scaled up 50 times for $V_{l,t} = 1.0\%$.

In presence of stiff infills, comparison of the deformed configurations for centred frames with and without openings (Figure 7.1 and Figure 6.3) does not show large differences. In fact, the structure has considerable flexural and shear stiffness to resist against deformations imposed by soil movements even if the infills containing openings.

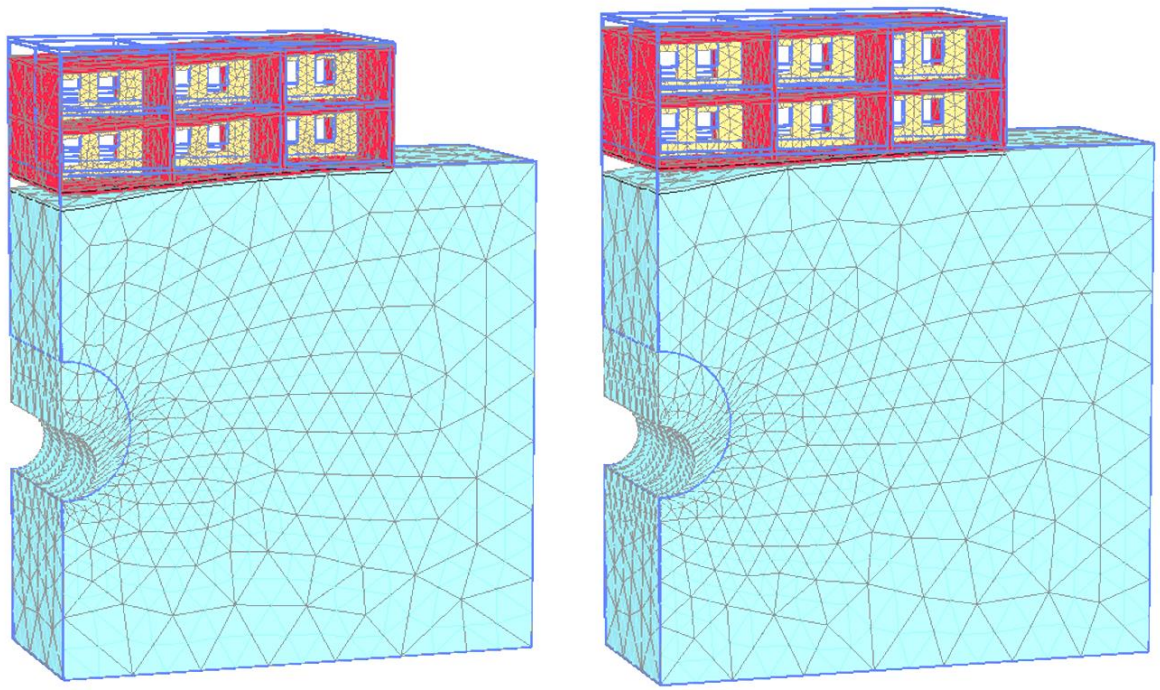

(a) (b)

Figure 7.1. Comparison between deformed configurations for a) **2Se0L_Flex_O** b) **2Se0L_Stiff_O** models in PLAXIS 3D ($\boldsymbol{V_{l,t} = 1.0\%}$).

The horizontal and vertical displacements of centred frames for the cases with openings are shown in Figure 7.2. In the case of stiff infills with openings, the detachment of the soil starts appearing at $V_{l,t} = 1.0\%$ at the central part of the building, while without openings the gap formation starts appearing already for $V_{l,t} = 0.4\%$. On average, the foundation settlement values are always slightly higher when openings in infill walls are included. The fact is that the presence of openings reduces the overall building stiffness and the behavior tends to move toward the one where only the frame structure is modelled. In other words, the frame experiences a decrease in structural stiffness and an increase in frame settlements due to the presence of openings in comparison to the frames with a fully masonry infill.

In Figure 7.2, horizontal displacements of the frame foundation are nearly zero as in the previous analyses for the centred structures. In presence of openings, horizontal displacement at the ground surface tends to those of the bare frame; on the contrary, in cases without openings, displacements converge to those of the greenfield case.

Figure 7.3 summarises angular distortions induced within the bays at different tunnel volume losses. As expected, results for the bare frame and the frame with openings in flexible infills are nearly the same. The additional stiffness provided by stiff infills with openings reduces distortions to be similar to those of the greenfield angular ones at the external bays. In centred

structures with stiff infills, the openings increase the angular distortions and decreases the structural stiffness in comparison to the frames with fully masonry infills. Similar to the previous cases, the distortions of the central bays above the tunnel decreases with respect to the greenfield case due to the gap formation mechanism, which prevented further settlements at the centreline.

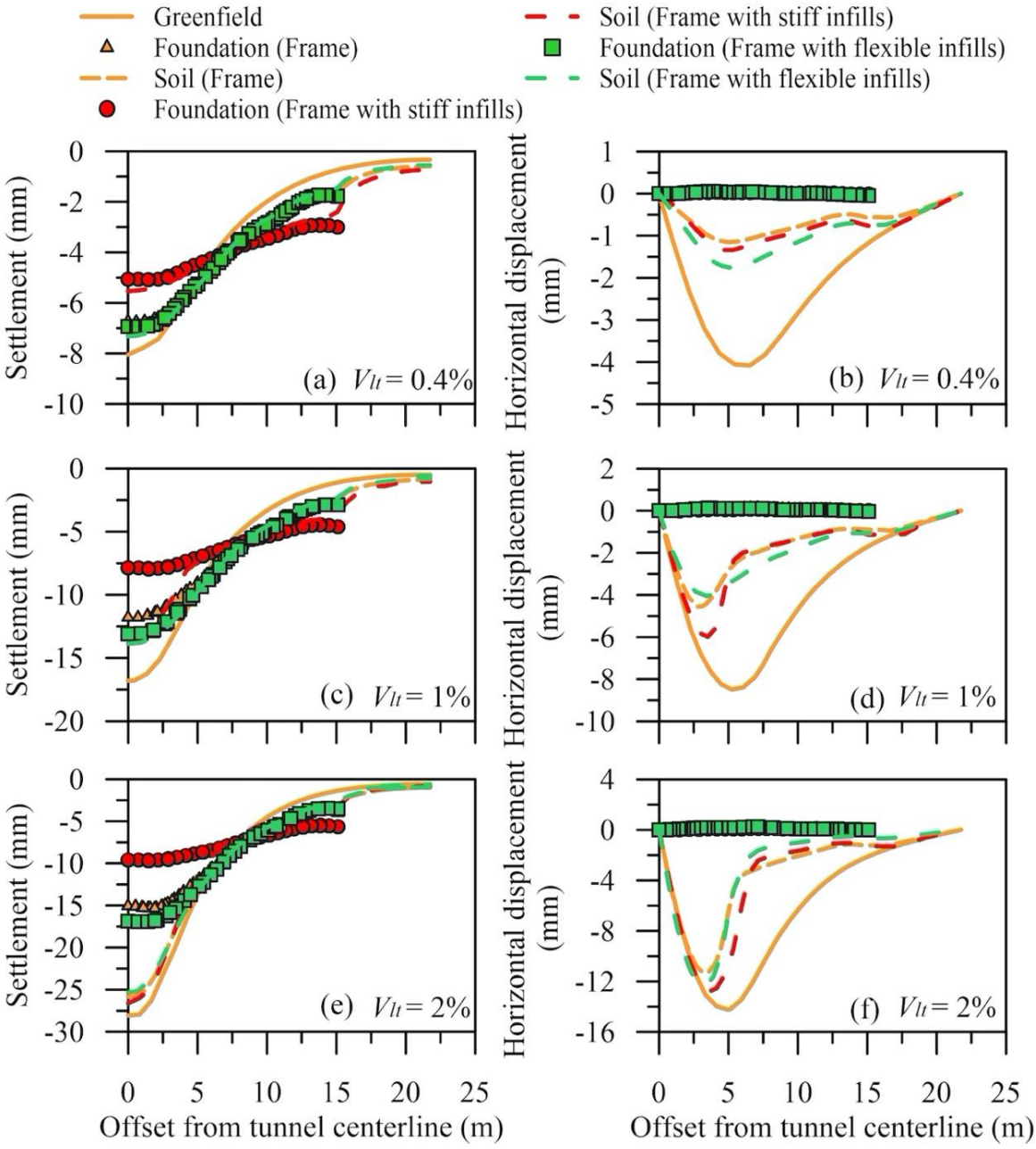

Figure 7.2. Comparison between numerical predictions for models **2Se0L_Bare**, **2Se0L_Flex_O**, and **2Se0L_Stiff_O** ($\boldsymbol{V_{l,t} = 0.4\%,\ 1.0\%,\ \text{and}\ 2.0\%}$).

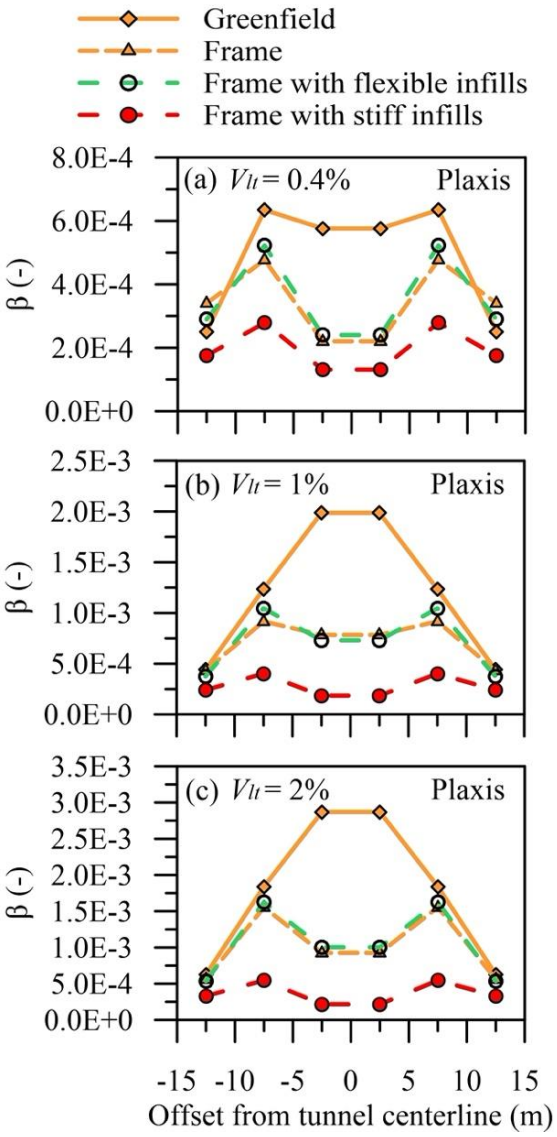

Figure 7.3. Angular distortion of bays for model **2Se0L_O** ($\boldsymbol{V_{l,t} = 0.4\%,\ 1.0\%,\ \text{and}\ 2.0\%}$).

The contours of tensile strains for stiff and flexible infills with openings are plotted in Figure 7.4. The presence of openings for maximum tensile strains in flexible infills produces an incremet in the category of damage from negligible (CAT.1) to very slight (CAT.2) for $V_{l,t} = 0.4\%$, and from slight (CAT.3) to moderate (CAT.4) for $V_{l,t} = 1.0\%$ and 2.0%. Burland (1997) refers the moderate (CAT.4) damage class to 0.3% of the tensile strain limit in which the approximate crack width is between 5 to 15mm. Similarly, the tensile strain distribution in stiff infills indicates that the presence of openings leads to an increase in the damage class from negligible (CAT.1) to very slight (CAT.2) for the larger values of tunnel volume loss (e.g., $V_{l,t} = 1.0\%$ and 2.0%). It is observed that the openings play a vital role in developing the

tensile strains to reach the maximum values in the proximity of window's corners, mainly located in the internal bays above the tunnel. In addition, the principal direction of tensile strains, having an inclination of 45°, indicate the direction of the crack paths. Comparison of tensile strain contours for infills with and without openings in model 2Se0L demonstrates the role of openings on tensile strain. The directions of tensile strain indicate that the cracking patterns are possibly through these directions. Additionally, tunnel volume losses of ($V_{l,t}$ = 1.0% and 2.0%, there is a moderate or high chance to have damages in flexible infills due to the presence of openings.

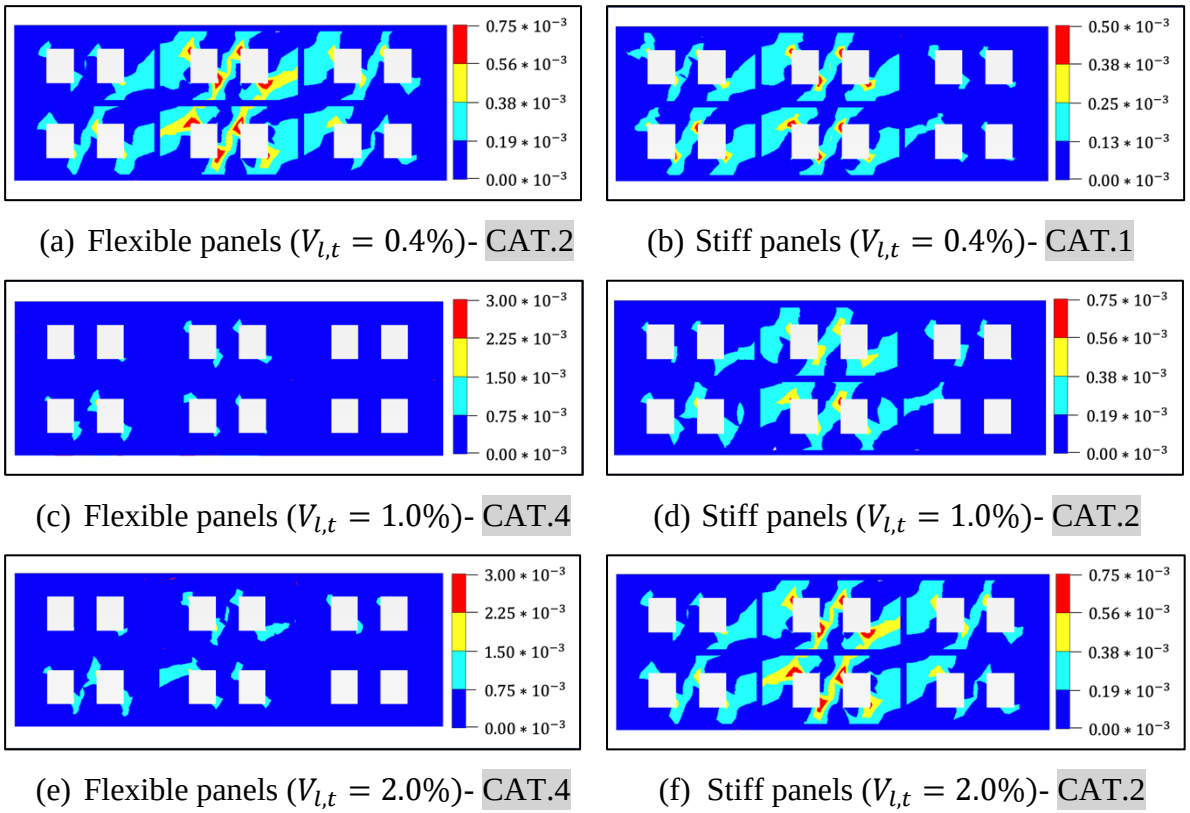

(a) Flexible panels ($V_{l,t}$ = 0.4%)- CAT.2 (b) Stiff panels ($V_{l,t}$ = 0.4%)- CAT.1

(c) Flexible panels ($V_{l,t}$ = 1.0%)- CAT.4 (d) Stiff panels ($V_{l,t}$ = 1.0%)- CAT.2

(e) Flexible panels ($V_{l,t}$ = 2.0%)- CAT.4 (f) Stiff panels ($V_{l,t}$ = 2.0%)- CAT.2

Figure 7.4. Maximum tensile strains of panels for model **2Se0L_O**.

Chapter. 8. Conclusions

A comprehensive numerical study on the response of framed buildings to tunnelling was presented, including the comparison with experimental centrifuge tests conducted at the University of Nottingham. This research illustrates the capability of Finite Element numerical modelling in PLAXIS 2D and 3D, implementing an advanced constitutive law for the soil and a realistic structural model, in predicting the response of bare framed buildings. Then, numerical capabilities were used to investigate the influence of stiff and flexible infill panels, while providing insights into the structural deformation mechanics. Generally, the study focused on the structural deformations induced by the tunnel excavation at different values of the tunnel volume loss. The tunnelling-induced displacements of the buildings and the underlying soil were analysed, and the structure deformations were studied using foundation displacements, angular distortions, and strain-based damage categories. The following conclusions can be drawn from the work.

- results for the bare frame simulation confirmed the robustness of the adopted 3D numerical approach against 2D modelling in replicating experimental outcomes of soil-structure interaction due to tunnelling;
- in modelling frame structures, it is important to include a tensionless soil-foundation interface that allows for the detachment due to the superstructure induced load redistribution;
- the effects of flexible and stiff infills on angular distortions and maximum tensile strains are reported in a few words. Firstly, bare frames (or frames with flexible infills) with a semi-flexible response were found to decrease distortions associated to the greenfield settlement trough. Secondly, the increase of building stiffness (due to additional storeys or stiff infill panels) decreased the angular distortions in long frames. Thirdly, short frames experienced constant and small values for angular distortions along the entire transverse length of the structure. Regarding the evaluation of maximum tensile strains, the number of storeys, eccentricity and stiffness of infills played the main roles. The stiff masonry infills caused almost undamaged outcomes in comparison to flexible infills. In flexible infills, the assessment of resulted damages holds this idea that centred structures exprienced damage class of CAT.3, while the eccentric buildings faced CAT.2. By increasing the eccentricity from $e/B = 0$ to 0.2, the maximum tensile strain of bays moved from the center to the side closed to the tunnel proximity, while the level

of damage in other side of the frame remained negligible. In case of $e/B = 0.5$, the pattern was changed, and the centeral bays of frames experienced negligible damages in comparison with the external bays;

- for centred structures, the presence of the stiff infills further decreases the frame settlements and increases the gap at the soil-structure interface with respect to bare frame and flexible infills. Also, the soil horizontal displacements under the frame with stiff panels are slightly greater in comparison to those calculated without the infills, because of the greater pressure redistribution of the stiffer building towards the foundation edges. Thus stiff infills, which are perfectly bound to the frame columns and slabs, could play an important role in decreasing the risk for damage;
- for eccentric structures, the gap formation beneath the long frames clearly developed by decreasing the eccentricity from $e/B = 0.5$ to 0.2 and by increasing the volume loss of the tunnel. In case of the stiffened structures (due to additional storeys or stiff infill panels), an increase in the number of storeys (that increase both weight and stiffness) decreased the gap size but the increase in stiffness only (as when adding the stiff infills) certainly increased the gap size. Also, the settlement of soil beneath the frame decreased by stiffening the structures. This mechanisms agrees with the conclusion drawn for centred structures. In eccentric structures with $e/B = 0.5$, by considering the frame as a cantilever beam, increasing the length of the frame provided enough support which leads to mitigate the settlements and movements at the other end of the frame positioned over the tunnelling. In case of horizontal movements for eccentric structures with $e/B = 0.2$ and 0.5, shortening the frame length increased the horizontal movements of the foundations in comparison to long frames. Moreover, the eccentric-short frames could tilt to accommodate ground settlements, while the concentric frames prevented the tilt of the frame;
- the effects of the openings in the infills was also briefly investigated. In centered structures with openings, the foundation settlements were slightly higher in comparison to stiff masonry infills since the presence of openings reduced the overall building stiffness, thus resulting in an intermediate building behaviour between the bare frame and the infilled frame with stiff panels. The openings played an important role in developing tensile strains, causing a strain concentration in the proximity of window's corners, mainly in the internal bays above the tunnel. For the larger tunnel volume lossess (e.g., $V_{l,t} = 1.0\%$ and 2.0%), there was a moderate to high chance to have

damages in flexible infills due to the presence of openings. In addition, the principal direction of tensile strains with an inclination of 45° denotes the possible presence of shear crack paths.

References

Amorosi, A., Boldini, D., De Felice, G. & Malena, M. 2012. Tunnelling-induced deformation in a masonry structure: a numerical approach. *Proceedings of the 7th international symposium on geotechnical aspects of underground construction in soft ground, Rome (ed. G. Viggiani)*, 353-359.

Amorosi, A., Boldini, D., De Felice, G., Malena, M. & Sebastianelli, M. 2014. Tunnelling-induced deformation and damage on historical masonry structures. Géotechnique, **64**, 118-130.

Attewell, P. 1982. Predicting the dynamics of ground settlement and its derivatives caused by tunnelling in soil. Ground engineering, **15**, 13-22.

Attewell, P.B., Yeates, J. & Selby, A.R. 1986. Soil movements induced by tunnelling and their effects on pipelines and structures.

Been, K. & Jefferies, M.G. 1985. A state parameter for sands. Géotechnique, **35**, 99-112.

Bilotta, E., Paolillo, A., Russo, G. & Aversa, S. 2017. Displacements induced by tunnelling under a historical building. Tunnelling and Underground Space Technology, **61**, 221-232.

Bishop, A. & Wesley, L. 1975. A hydraulic triaxial apparatus for controlled stress path testing. Géotechnique, **25**, 657-670.

Blasi, G., De Luca, F. & Aiello, M.A. 2018. Brittle failure in RC masonry infilled frames: the role of infill overstrength. Engineering Structures, **177**, 506-518.

Boldini, D., Losacco, N., Bertolin, S. & Amorosi, A. 2016. Modelling of reinforced concrete framed structures interacting with a shallow tunnel. Procedia Engineering, **158**, 176-181.

Boldini, D., Losacco, N., Bertolin, S. & Amorosi, A. 2018. Finite Element modelling of tunnelling-induced displacements on framed structures. Tunnelling and Underground Space Technology, **80**, 222-231.

Boone, S.J. 1996. Ground-movement-related building damage. Journal of geotechnical engineering, **122**, 886-896.

Boscardin, M.D. & Cording, E.J. 1989. Building response to excavation-induced settlement. Journal of geotechnical engineering, **115**, 1-21.

Brinkgreve, R., Kumarswamy, S. & Swolfs, W. 2017. Plaxis reference manual. PLAXIS bv.

Burd, H. 1999. The history of Plaxis. Beyond 2000 in Computational Geotechnics, 35.

Burd, H., Houlsby, G., Augarde, C. & Liu, G. 2000. Modelling tunnelling-induced settlement of masonry buildings. Proceedings of the institution of civil engineers-geotechnical engineering, **143**, 17-29.

Burland, J. 1977. Behaviour of foundations and structures on soft ground. Proc. 9th ICSMFE, 1977, **2**, 495-546.

Burland, J. 1997. Assessment of risk of damage to buildings due to tunnelling and excavation.

Burland, J.B. & Wroth, C. 1975. *Settlement of buildings and associated damage*.

Cobanoglu, B., Aldemir, A., Demirel, İ.O., Binici, B., Canbay, E. & Yakut, A. 2017. Seismic performance assessment of masonry buildings using in situ material properties. Journal of Performance of Constructed Facilities, **31**, 04017033.

Cook, D. 1994. Studies of settlement and crack damage in old and new facades. *Proc., 3rd Int. Masonry Conference., London, England*, 203-211.

Dafalias, Y.F. & Manzari, M.T. 2004. Simple plasticity sand model accounting for fabric change effects. Journal of Engineering mechanics, **130**, 622-634.

De Borst, R. & Vermeer, P. 1984. Possibilites and limitations of finite elements for limit analysis. Géotechnique, **34**, 199-210.

Ellis, E., Cox, C., Yu, H., Ainsworth, A. & Baker, N. 2006. A new geotechnical centrifuge at the University of Nottingham, UK. *6th International Conference of Physical Modelling in Geotechnics: ICPMG*, 129-133.

Fargnoli, V., Gragnano, C., Boldini, D. & Amorosi, A. 2015. 3D numerical modelling of soil–structure interaction during EPB tunnelling. Géotechnique, **65**, 23-37.
Farrell, R., Mair, R., Sciotti, A. & Pigorini, A. 2014. Building response to tunnelling. Soils and foundations, **54**, 269-279.
Farrell, R.P. 2011. *Tunnelling in sands and the response of buildings*, University of Cambridge.
Franza, A. 2017. *Tunnelling and its effects on piles and piled structures*, University of Nottingham.
Franza, A., Deck, O. & DeJong, M.J. 2020. Charts for the mining-induced deflection of buildings. Canadian Geotechnical Journal.
Franza, A. & Marshall, A.M. 2019. Empirical and semi-analytical methods for evaluating tunnelling-induced ground movements in sands. Tunnelling and Underground Space Technology, **88**, 47-62.
Franzius, J.N. 2003. Behaviour of buildings due to tunnel induced subsidence. Imperial College of Science, Technology and Medicine.
Franzius, J.N., Potts, D.M. & Burland, J.B. 2006. The response of surface structures to tunnel construction. Proceedings of the institution of civil engineers-geotechnical engineering, **159**, 3-17.
Giardina, G., Hendriks, M.A. & Rots, J.G. 2010. Numerical analysis of tunnelling effects on masonry buildings: the influence of tunnel location on damage assessment. *Advanced Materials Research*. Trans Tech Publ, 289-294.
Goh, K.H. & Mair, R.J. 2014. Response of framed buildings to excavation-induced movements. Soils and foundations, **54**, 250-268.
Kramer, S.L. 1996. Geotechnical earthquake engineering. Pearson Education India.
Leca, E. & New, B. 2007. Settlements induced by tunneling in soft ground. Tunnelling and Underground Space Technology, **22**, 119-149.
Li, X.-S. & Wang, Y. 1998. Linear representation of steady-state line for sand. Journal of geotechnical and geoenvironmental engineering, **124**, 1215-1217.
Li, X.S. & Dafalias, Y.F. 2000. Dilatancy for cohesionless soils. Géotechnique, **50**, 449-460.
Loganathan, N. & Poulos, H. 1998. Analytical prediction for tunneling-induced ground movements in clays. Journal of geotechnical and geoenvironmental engineering, **124**, 846-856.
Losacco, N., Burghignoli, A. & Callisto, L. 2014. Uncoupled evaluation of the structural damage induced by tunnelling. Géotechnique, **64**, 646-656.
Losacco, N., Callisto, L. & Burghignoli, A. 2016. Soil-structure interaction due to tunnelling in soft ground, an equivalent solid approach. *Structural Analysis of Historical Constructions: Anamnesis, Diagnosis, Therapy, Controls*. CRC Press, 495-502.
Mair, R. 2013. Tunnelling and deep excavations: Ground movements and their effects. *Proceedings of the 15th European conference on soil mechanics and geotechnical engineering–geotechnics of hard soils–weak rocks (part 4)*. IOS Press, Athens, Greece, 39-70.
Mair, R. & Taylor, R. 1997. Theme lecture: Bored tunnelling in the urban environment. *Proceedings of the fourteenth international conference on soil mechanics and foundation engineering*. Rotterdam, 2353-2385.
Mair, R., Taylor, R. & Burland, J. 1996. Prediction of ground movements and assessment of risk of building damage due to bored tunnelling. *Geotechnical aspects of underground construction in soft ground*, 713-718.
Mair, R.J. 1978. *Centrifugal modelling of tunnel construction in soft clay*.
Maleki, M., Sereshteh, H., Mousivand, M. & Bayat, M. 2011. An equivalent beam model for the analysis of tunnel-building interaction. Tunnelling and Underground Space Technology, **26**, 524-533.
Manzari, M.T. & Dafalias, Y.F. 1997. A critical state two-surface plasticity model for sands. Géotechnique, **47**, 255-272.

Marshall, A. 2009. *Tunnelling in sand and its effect on pipelines and piles*, University of Cambridge.
Martinelli, M., Miriano, C. & Tamagnini, C. 2015. *Implementation of SANISAND model as ABAQUS umat and PLAXIS user defined subroutines.* Charles University in Prague Faculty of Science.

O'Rrielly, M.P. & New, B. 1982. *Settlements above tunnels in the United Kingdom-their magnitude and prediction* Report **090048862X**.
Peck, R.B. 1969. Deep excavations and tunneling in soft ground. Proc. 7th ICSMFE, 1969, 225-290.
Pickhaver, J., Burd, H. & Houlsby, G. 2010. An equivalent beam method to model masonry buildings in 3D finite element analysis. Computers & structures, **88**, 1049-1063.
Potts, D. & Addenbrooke, T. 1997. A structure's influence on tunnelling-induced ground movements. Proceedings of the institution of civil engineers-geotechnical engineering, **125**, 109-125.
Rankin, W. 1988. Ground movements resulting from urban tunnelling: predictions and effects. Geological Society, London, Engineering Geology Special Publications, **5**, 79-92.
Richard, F., Woods, R. & Hall Jr, J. 1970. Vibration of soils and foundations.
Ritter, S., Giardina, G., Franza, A. & DeJong, M.J. 2020. Building deformation caused by tunneling: centrifuge modeling. Journal of geotechnical and geoenvironmental engineering, **146**, 04020017.
Roscoe, K., Schofield, A. & Thurairajah, A. 1963. Yielding of clays in states wetter than critical. Géotechnique, **13**, 211-240.
Roscoe, K.H. & Burland, J. 1968. On the generalized stress-strain behaviour of wet clay.
Rowe, R. & Kack, G. 1983. A theoretical examination of the settlements induced by tunnelling: four case histories. Canadian Geotechnical Journal, **20**, 299-314.
Sloan, S. & Randolph, M.F. 1982. Numerical prediction of collapse loads using finite element methods. International Journal for Numerical and Analytical Methods in Geomechanics, **6**, 47-76.
Son, M. & Cording, E.J. 2005. Estimation of building damage due to excavation-induced ground movements. Journal of geotechnical and geoenvironmental engineering, **131**, 162-177.
Springman, S., Nater, P., Chikatamarla, R. & Laue, J. 2002. Use of flexible tactile pressure sensors in geotechnical centrifuges. *Physical modelling in geotechnics: ICPMG'02*, 113-118.
Taylor, R., Grant, R., Robson, S. & Kuwano, J. 1998. An image analysis system for determining plane and 3-D displacements in soil models. *Centrifuge 98*, 73-78.
Timoshenko, S. 1957. Strength of Materials, Part ID Van Nostrand Co. Inc., New York, NY, 19-10.
Visone, C. & Santucci De Magistris, F. 2009. Mechanical behaviour of the Leighton Buzzard Sand 100/170 under monotonic, cyclic and dynamic loading conditions. *XIII ANIDIS-L'ingegneria Sismica in Italia*. StudioStampa SA.
Wan, M., Standing, J., Potts, D. & Burland, J. 2017. Measured short-term subsurface ground displacements from EPBM tunnelling in London Clay. Géotechnique, **67**, 748-779.
Wood, D.M. 2003. Geotechnical modelling. CRC press.
Wood, D.M. & Belkheir, K. 1994. Strain softening and state parameter for sand modelling. Géotechnique, **44**, 335-339.
Xu, J., Franza, A. & Marshall, A.M. 2020. The response of framed buildings on raft foundations to tunneling. Journal of geotechnical and geoenvironmental engineering.
Xu, J., Franza, A., Marshall, A.M., Losacco, N. & Boldini, D. 2020. Tunnel–framed building interaction: comparison between raft and separate footing foundations. Géotechnique, 1-14.

Xu, J., Marshall, M.A., Franza, A., Boldini, D., Amorosi, A. & DeJong, J.M. 2019. The response of framed buildings on raft foundations to tunnelling: a centrifuge and numerical modelling study. *17th European Conference on Soil Mechanics and Geotechnical Engineering*, Vol. 1, 1–8.
Yiu, W., Burd, H. & Martin, C. 2017. Finite-element modelling for the assessment of tunnel-induced damage to a masonry building. Géotechnique, **67**, 780-794.
Zhou, B. 2015. *Tunnelling-induced ground displacements in sand*, University of Nottingham.